DEM SIMULATIONS OF DRAINED AND UNDRAINED BEHAVIOUR

GUOBIN GONG

BEng, MSc

A thesis submitted to The University of Birmingham

for the degree of

DOCTOR OF PHILOSOPHY

Department of Civil Engineering

The University of Birmingham

June 2008

ABSTRACT

This thesis reports the results of DEM (Discrete Element Method) simulations of the behaviour of granular material for axisymmetric compression and plane strain deformation under both drained and undrained conditions. The aim is to study the behaviour of saturated granular material using DEM and the objectives of this thesis are:

- to explore the drained behaviour of granular material using DEM
- to explore the undrained behaviour of loose samples of granular material with and without preshearing history, using DEM
- to compare axisymmetric compression and plane strain behaviour of a granular material under both drained and undrained conditions, using DEM

A servo-control mode with constant mean stress is used to model drained simulations, and a strain-control model with constant volume is used to model undrained simulations. A periodic cell is used for all the simulations. For the drained simulations, the results of both dense and loose systems are presented, and all the systems reach a unique critical state at large strains. For the undrained simulations, mainly the results of loose systems are presented. The influence of preshearing history is also examined for a loose system under undrained axisymmetric compression conditions. The concept of liquefaction is shown to strongly correlate with mechanical coordination number, and liquefaction is shown to be related to structural mechanism.

An attempt has been made to compare the axisymmetric compression and plane strain deformation for the drained and undrained conditions respectively. Shear strength criteria are examined and the Lade criterion is shown to be the most appropriate failure criterion.

KEY WORDS: Discrete Element Method, simulation, critical state, shear strength, liquefaction, coordination number

ACKNOWLEDGEMENTS

I wish to extend my greatest gratitude to my supervisers: Dr Colin Thornton and Prof Andrew Chan for mentoring me throughout the course of my PhD study, and for their help and support.

I wish to extend my gratitude to Dr Ling Zhang and her husband Dr Charley Wu for their guidance and help. I wish to thank Dr David Kafui for his patient help with the TRUBAL code. I wish to thank Prof CDF Rogers and Dr Ian Jefferson for their constructive comments on my thesis. I would also like to thank my former teachers and mentors: Prof Jun Wei, Prof Xiaoxiong Zha and Dr Yu Zhu, for their help and encouragement.

A great thank goes to EPSRC and Civil Engineering Department in the University of Birmingham for providing me a 3-year fully-funded PhD studentship.

The final stage of this thesis is accomplished during my employment with Special Service Division in Mott MacDonald Limited and I would like to thank my manager Dr Paul Norris and my colleague Dr Yuehua Liang for their concern and help.

Finally, thank my parents and my wife Zhuoer Hu for their steadfast love and support.

Contents

List of figures, tables and symbols

List of figures

List of tables

List of symbols

σ_{ij}	stress tensor
ε_{ij}	strain tensor
ϕ_{ij}	fabric tensor
Z_a	apparent coordination number
Z_m	mechanical coordination number

μ	interparticle friction
q	deviator stress
p	mean stress
ε_v	volumetric strain
$\sin\varphi$	mobilised friction angle

CHAPTER 1: INTRODUCTION

1.1 Motivation of Discrete Element Method

Despite a historical effort spanning at least 300 years (with notable contributions from, for instance, Coulomb, Reynolds and Bagnold), a fundamental understanding of the stress response of granular materials remains elusive, as does the ability to relate fundamental concepts to real applications.

In classical continuum mechanics, three completely independent assumptions are made, i.e. continuity, homogeneity and isotropy [Malvern (1969)]. The idealization of the material is called a continuum, or more precisely, the continuum model of the material [Khan and Huang (1995)]. Granular materials consist of grains in contact and surrounding voids. The micromechanical behaviour of granular materials is therefore inherently discontinuous and heterogeneous, and generally anisotropic.

Kishino (1998) pointed out that in continuum mechanical analyses of granular materials, the determination of a constitutive model is the most difficult process. A constitutive model based on continuum approaches usually includes a lot of material constants (or model parameters), which sometimes have no clear physical meaning (Kishino, 1998). However, when one observes the granular materials as packed assemblies of particles, the mechanical interaction between particles is very simple and the material constants have explicit meanings. The ambiguous characters of the material constants based on continuum approaches may have their origin in the implicit expression of the geometry of a packed assembly of particles. Thus, one can expect to analyse granular materials in a more realistic way if one makes use of the discrete element approaches in which the particle arrangement is modelled explicitly.

Feda (1982) distinguished between the two different approaches in determining the mechanics of granular materials, the phenomenological approach (structure-less continuum approach) and the structural (sometimes called micromechanical) approach. The structural approach probes into the physical basis, more or less, and the discrete element approach is closer to this structural approach but it is a numerical approach. As to why the discrete element method (DEM) is an efficient method in studying granular materials in terms of both the macromechanical and micromechanical behaviours, this will be discussed in Chapter 2.

1.2 Motivation of this thesis

Since Cundall in 1971 first introduced the innovative distinct element method (DEM) into granular materials research, DEM has been developed to different levels and applied to a wide range of engineering applications. The content of this thesis is concerned with the quasi-static deformation of granular material such as sand. However, real granular materials like sand are very complex and it is very difficult for the development of theory in this area if there are no simplifying assumptions. As a first approximation, real particle shape is ignored and the particles are modelled as spheres. It is also assumed that the spheres are elastic and, consequently, the interactions between particles are modelled by algorithms based on theoretical contact mechanics rather than (the much simpler) linear springs. Also, since the particles are spherical no rolling resistance is considered. There are some other important issues missing in the published DEM studies of granular materials such as sand, some of which are the main motives of this thesis.

In DEM, very little research has been reported on the behaviour of loose samples. Liquefaction of very loose samples has not been well explained in soil mechanics. Partial liquefaction phenomenon for medium loose samples has not previously been reported by DEM simulations, and there are still arguments as to whether or not partial liquefaction is a real physical behaviour in soil mechanics.

The preloading history influence on undrained shear behaviour has been reported by Finge et al (2003) among others, but the explanation for the influence of the preloading history has not been well explored. There has not yet been published work on the preloading history influence on shear behaviour obtained from DEM simulations.

Although conventional triaxial tests and plane strain tests are fundamental element tests in soil mechanics, there has not been much published work on the comparison of these two types of tests even in the laboratory test literature. Also, there still seems to be argument on the appropriate shear strength failure criteria among soil mechanics researchers. DEM is an ideal tool for such a comparison since the same initial sample can be copied an infinite number of times if required, however, such a comparison has not yet been explored by DEM simulations.

Therefore the aim is to study the behaviour of saturated granular material using DEM and the objectives of this thesis are:

- to explore the drained behaviour of granular material using DEM
- to explore the undrained behaviour of loose samples of granular material with and without preshearing history, using DEM
- to compare axisymmetric compression and plane strain behaviour of a granular material under both drained and undrained conditions, using DEM

1.3 Layout of this thesis

The whole thesis is divided into eight chapters. In Chapter 2 the computational algorithms used in the DEM simulations are briefly introduced and a literature review of the development and applications of DEM, in the context of quasi-static deformation, is provided. This is followed by four chapters (Chapters 3 – 6) which report the results of the DEM simulations that have been performed during the PhD research programme. Each of these chapters (except chapter 6) includes a literature review of corresponding experimental work and/or DEM simulation work. Chapters 3 and 4 provide results of drained axisymmetric compression and drained plane strain simulations respectively. In both cases all the simulations were performed with the mean stress held constant. The results of undrained axisymmetric compression and undrained plane strain simulations are reported in Chapters 5 and 6 respectively. As no fluid is explicitly modelled in this work, undrained test is modelled using constant volume simulation. Emphasis is placed on the behaviour of loose samples. In Chapter 7, the results of the plane strain and axisymmetric compression simulations, both drained and undrained, are compared.

Finally, in Chapter 8, some conclusions on the work presented in this thesis are provided and further developments are suggested.

1.4 Terminology used

The stresses and strains are taken as compressive positive. Drained means constant mean stress and undrained means constant volume when they refer to the DEM simulation reported in this thesis. The stresses mean effective stress except otherwise pointed out.

CHAPTER 2: REVIEW OF DEM SIMULATIONS

2.1 Introduction

In a granular medium composed of discrete particles, forces are transferred only through the interparticle contacts. The discrete nature makes the constitutive relationship very complex. Interpretation of tests on real granular media, such as sand, is difficult because the stresses inside the sample cannot be measured and must be estimated from the boundary conditions. The observed stress-strain behaviour (from the boundary measurements) for a granular medium such as sand, is non-linear and hysteretic, which is dependent on stress level, stress path and stress history. Such complexity has led to the developement of models of granular media, which may be analytical, physical (typically photoelastic) or numerical.

The analytical models can be found in Duffy and Mindlin (1957), Deresiewicz (1958a, 1958b), Duffy (1959), Thornton (1979) and Thornton and Barnes (1982) for uniform packings; and Digby (1981), Walton (1987), and Chang (1988) for random packings. However, the analytical models are limited in that, the particles are spheres or discs, the particles are of uniform size, loading/unloading paths are restricted, and/or only conditions of small deformation can be applied.

The physical (typically photoelastic) models can be found in Dantu (1957), Wakabayashi (1957), Drescher and De Josselin de Jong (1972), Drescher (1976), among others.

However, the physical analyses are time-consuming and lack flexibility to run multiple tests on identical specimens.

Traditionally, theoretical models of material behaviour are validated by physical experiments. However, both traditional theoretical and experimental investigations of granular materials rely on estimates of the macroscopic stress and strain states from the boundary measurements, which themselves depend on assumptions made about the material behaviour. It is not clear whether information obtained at the boundaries of a specimen can reliably represent the ensemble state of stress and strain inside the specimen, which is normally supposed to represent the constitutive behaviour of the material at a point in a continuum.

The most powerful way of modelling granular media is by numerical techniques. Numerical modelling has many advantages over the analytical models and the physical models. In numerical modelling, boundary conditions may be controlled precisely or even there can be no boundary by using a periodic cell, stresses and strains may be measured over any volume within the sample, any parameter may be varied while keeping the other parameters unchanged, any data are accessible at any stage of the test, and the same starting state can be used many times.

The Distinct (Discrete) Element Method (DEM) is a numerical model, which was originally developed by Cundall (1971, 1974), for the analysis of rock mechanics problems. Cundall (1978) and Strack and Cundall (1978) incorporated the methods into the computer program ‘BALL’, and Cundall and Strack (1979a, 1979b) used the method to investigate the constitutive laws for soil. At the same time as the development of DEM, Serrano and Rodriguez-Ortiz (1973) developed a numerical quasi-static model for granular media based on displacement methods of structrual mechanics and finite element method (FEM). However, the method was not able to follow large displacement and rearrangements which are fundamental characteristics of state changing processes of granular media. Cundall and Hart (1992) has shown that DEM is better in modelling a discontinuous material than other numerical tools such as FEM and BEM (boundary element method). Cundall (2001) suggested that the future trend for numerical modelling in soil and rock may consist of the replacement of continuum methods by particle methods, although it is currently difficult to apply such particle methods to large-scale problems. This should be improved in the future due to the continuing development of computer hardware/software.

In this chapter, a brief computational algorithm of DEM will be outlined, previous work on development and application of DEM simulations is reviewed and focused on quasi-static deformation. Micromechanics concepts frequently used in granular materials will be discussed in the final section.

2.2 Brief description of computational algorithms in DEM

A brief description of computational algorithms will be given below. Further detailed information can be found in Cundall and Strack (1979b, 1979c), Strack and Cundall (1978), and Zhang (2003).

In DEM, the interaction of the discrete particles is monitored contact by contact and the motion of the particles modelled particle by particle. The DEM program models the particle interactions as a dynamic process and the time evolution of the system is advanced using a simple explicit time-dependent finite difference technique. At any time *t*, interparticle force increments are calculated at all contacts from the relative velocities of the contacting particles using incremental force-displacement rules. The interparticle forces are then updated and are resolved to obtain the out-of-balance forces and moments on each particle, from which new accelerations (both linear and angular) of each particle are then calculated using Newton's second law of motion. Numerical integration of the accelerations is then performed over a small time step to give new velocities (both linear and angular) which are then numerically integrated to give displacement increments (both linear and angular) from which the new particle positions are obtained. Having obtained new positions and velocities for all the particles, the program repeats the cycle of updating contact forces and particle locations. Checks are incorporated to identify new contacts and contacts that no longer exist.

From the above process, all complete information of each particle can be tracked. Such basic local information for a particle includes forces at contacts and contact positions, from which the ensemble average (macroscopic) stress tensor can be established in a chosen region, as will be explained later in this chapter. The ensemble average strain tensor can also obtained in the same way. Such an averaging process is also called the microstructural approach by Bagi (1996) or homogenization process by Cambou (1993). The constitutive relationship between the macroscopic stress and strain can be established viewing the particle assembly as a point in a continuum under different stress or strain probes, which may be incorporated into the finite element method (FEM) analyses of engineering scale problems.

2.3 Review of development and application of DEM on quasi-static condition

In this section, the development of DEM codes, and the application of DEM (mainly related to geotechnical laboratory testing) will be summarised. A summary of the literature work and the research direction undertaken in this thesis is provided at the end of this section.

2.3.1 Development of DEM programs: BALL and TRUBAL

The early version of the 2D DEM program BALL developed by Cundall (1978) was validated by Cundall and Strack (1979a, 1979b), by comparing the force vector plots with a photoelastic analysis by De Josselin De Jong and Verruijt (1969) and by reproducing stress-strain behaviour reported by Oda and Konishi (1974). In this early version of BALL, a linear spring contact law was used, specimens were made up of discs, and wall or particle boundaries were applied. Both wall and particle boundaries could be strain-controlled, stress-controlled, or servo-controlled, the details of which can be found in Cundall et al (1982).

BALL was extended to an early version of TRUBAL by Cundall and Strack (1979c), who used linear spring contact laws, and the structure of the program resembles that of BALL. This early version of TRUBAL was specifically designed for reproducing the work of

Rowe (1962), in which the results from a triaxial test on an assembly of face-centered-cubic packings of steel spheres were presented. Neither wall nor particle boundaries were available. Only fixed forces could be applied to any set of spheres, which restricts the analysis to being valid only for small displacements and strains. The numerical results with boundary rotations inhibited showed better agreement with Rowe (1962) than those without constraint on rotations.

Cundall (1988) extended the above early version of TRUBAL to random arrays of spheres, and introduced the notion of a periodic cell to DEM. A periodic cell allows a particle that moves out of the cell to be re-mapped back into the cell at a corresponding location on the opposite face. The particle that moves out of the cell carrys all the same information as that moving into the cell, except for particle positions. An infinite lattice can be imagined by replicating one cell throughout space. Thus, the simulation can be performed free from boundaries. In this version, nonlinear contact laws are used with complete Hertz normal contact theory and a simplified tangential contact theory of Mindlin (1949). Thornton and Randall (1988) implemented particle-particle interaction rules that were based on theoretical contact mechanics with Hertz normal contact theory and the complete tangential contact theory of Mindlin and Deresiewcz (1953) in TRUBAL.

2.3.2 Modelling geotechnical laboratory tests using DEM

Although the DEM algorithm is essentially a dynamic process, it can also be used for quasi-static problems as it models quasi-static problems as a slow dynamic process by ensuring that the loading rates are low enough for inertial forces to be much smaller than typical contact forces as pointed out by Cundall and Strack (1979a), where rigid particles and compliant contacts were assumed. Viscous damping may be used to inhibit the build-up of kinetic energy and to bring the system to equilibrium. However, according to Kishino (1988), the movement of particles in quasi-static condition is not coaxial with the acceleration vector as assumed in DEM because of constraints by neighbouring elements (particles and/or boundaries). This led to the so-called Granular Element Method (GEM) developed by Kishino (1988, 1989). Similar to DEM, GEM calculates the displacements of each particle independently of the others, but the particles are displaced by using a successive relaxation technique based on the stiffness of the contacts with neighbouring elements. In the basic iteration step all particles are assumed to be fixed except one particle. The resultant of external contact forces acting on this particle is calculated and the displacement method is applied to determine its displacements. Then the next particle can be taken. Large displacements and rearrangements can be followed this way but its convergence is slow. Some other quasi-static models for granular assemblies can be found in Bagi (1993), Tzaferopoulos (1996), among others.

Ting et al (1989) applied the program DISC (modified version of BALL) to simulate geotechnical laboratory tests and the results showed that 2D DEM can simulate realistic soil behaviour appropriately when individual particle rotation is inhibited. Modelling of large-scale problems is accomplished to some degree by constructing a reduced-scale model, then applying the geotechnical centrifuge scaling relationships in order to reduce the number of particles simulated and to ensure stress-strain-strength similitude between the model and prototype. Full-scale simulations of bearing capacity and lateral earth pressure tests, indicate that DEM can accurately simulate real geotechnical problems, including those possessing large local yield zones. Ting et al (1995) investigated the effect of particle shape on the strength and deformation mechanisms of assemblies of elliptical particles using DEM by varying individual particle aspect ratio. The results indicate that the DEM analysis using elliptical particles produces better quantitative and qualitative mechanical behaviour similar to real granular materials than when assemblies of discs are used, the conclusion of which is the same as that in Rothenburg and Bathurst (1992). The contact detection with 2D particle shapes other than discs requires more time (also true for 3D particle shapes other than spheres).

Dobry and Ng (1992) presented a general overview of applications of DEM to granular media, and incorporated Hertz-Mindlin contact solution to the TRUBAL code developed by Strack and Cundall (1984). They presented some 2D cyclic shear results at small and large strains with the particle rotation prohibited. Ng and Dorby (1994) further reported some 3D simulation results under monotonic drained and cyclic constant volume loadings. Effects of particle rotation and intergranular friction were investigated respectively. When particle rotation was inhibited, higher strength, greater stiffness and stronger dilation were found compared to the case in which rotation was allowed. Higher strength, higher initial stiffness and greater dilation were also found when a larger microscopic friction angle (intergranular friction) was used. They showed macroscopic friction angle increased linearly with the microscopic friction angle. Ng and Petrakis (1996) investigated the small-strain response of random arrays of spheres using the above modified TRUBAL, and they found that the distribution of contact forces and the magnitude of the normal contact forces were of great importance to the macroscopic response of the medium. Lin and Ng (1997) extended the above DEM program to assemblies of ellipsoids. Ng (2001) investigated the influence of particle shapes on fabric evolution under drained triaxial compression using the program of Lin and Ng (1997), and the results indicated that particle shape does not influence shear strength at large strain, but does influence volume change. Ng (2002) further incorporated hydrostatic boundaries (which was used to simulate the chamber fluid but not the rubber membrane.) in their program and named it ELLIPSE3H. Ng (2004a, 2004b) performed a series of drained tests under different sample preparation methods and stress paths using ELLIPSE3H, in which different failure criteria proposed in the literature were compared. It was found that the Lade (1977) and Ogawa et al (1974) failure models showed the best agreement.

Jensen et al (1999) investigated the influence of structure interface (surface roughness and particle shape) by enhanced DEM, in which a particle of general shape is modelled as a combination of several smaller particles of simpler shape, such as a circle, into clusters that act as a single larger particle. The clusters more accurately model the geometry-dependent behaviour of the particles, such as particle interlock and resistance to rolling. The granular medium-structure interface shear tests are performed using both clustered and non-clustered particles, the results of which show that the clustered particles undergo less rolling and provide for increased shear resistence of the medium. Comparison of numerical simulations with typical response of laboratory specimens shows that DEM simulations using simple discs or spheres usually underestimates the shear resistance, because the particles made up of discs or spheres tend to roll or rotate excessively. In order to reduce particle (disc- or sphere- shaped) rotations to more realistic levels, particle rotation may be prohibited (Dobry and Ng, 1992), or rolling resistance may be added at contacts (Iwashita and Oda ,1998), or as an alternative, ellipse-shaped particles may be used in place of disc- shaped particles (Ting et al, 1995), or the discs may be glued together in clusters (Jensen et al, 1999), or fused overlapping spheres may be used (Powrie et al, 2005). Phenomena such as damage and grain crushing may also be investigated by glued particles to form agglomerates, see Cheng et al (2003) and Cheng et al (2004).

Sitharam (1999) reported the effect of confining pressure on the mechanical behaviour of granular materials from micromechanical considerations starting from the grain scale level, based on the results of numerically simulated tests on disc assemblages using DEM. The numerical results indicated a non-linear Mohr-Coulomb failure envelope with increase in confining pressure. The angle of internal friction slightly decreased with increase in confining pressure. Particle breakage was not considered in these simulations, and the decrease in the angle of internal friction was attributed to increased average coordination number and reduced fabric anisotropy. Sitharam et al (2002) reported numerical results of isotropic compression and triaxial shear tests under drained and undrained stress paths on 3D assemblages of polydisperse spheres in a periodic cell using DEM. Both loose and dense assemblies were investigated to study the evolution of the internal variables such as average coordination number and induced anisotropy during deformation along with the macroscopic behaviour. Micromechanical explanations were presented in terms of force and anisotropy coefficients. The results indicated there is a steady state, in which both macroscopic and microscopic descriptors are constant and independent of densities, but the density of the assembly has an obvious influence on the pre-steady-state behaviour.

Rothenburg and Bathurst (1989) investigated the developement of induced anisotropy during shear deformation of plane granular assemblies with disc-shaped particles by introducing statistical characteristics of fabric and contact forces. They introduced microstructural parameters that were explicitly related to the measure of deviatoric load by considering the condition of static equilibrium. Verification of the stress-force-fabric relationship was presented by DEM simulation, which was originally proposed by Rothenburg (1980) based on micromechanics approach and can be described as

$$\sin\varphi = \frac{1}{2}\frac{a + a_n + a_t}{1 + (\frac{aa_n}{2})} \approx \frac{1}{2}(a + a_n + a_t) \tag{2.1}$$

where $\sin\varphi$ is the mobilised angle of friction, and a, a_n, a_t are second-order coefficients of contact normal anisotropy, average normal force anisotropy, and average tangential force anisotropy, respectively. This relationship gives an important link between some macroscopic and microscopic descriptors. The relationship has also been verified using DEM in Bathurst and Rothenburg (1990) for 2D disc assemblies, in Rothenburg and Buthurst (1992) for 2D ellipse assemblies, in Ouadfel (1998) for 3D ellipsoid assemblies, and in Mirghasemi et al (2002) for 2D angular (polygon-shaped) particle assemblies. Rothenburg and Kruyt (2004) developed a theory of critical state and of the evolution of coordination number during quasi-static deformations of granular materials based on the interpretation of several DEM simulations of plane granular assemblies with a range of interparticle friction from nearly frictionless to infinitely rough. They suggested that the critical state is reached when rates of contact breakage and creation become equal. The interparticle friction was shown to be an essential element that affects stability of local configurations. The simulation data suggested that the packing fraction (solid fraction) was affected by both the anisotropy of contact orientations and by the coordination number, and suggested that critical state is characterized by both a critical coordination number and by a critical anisotropy, the combination of which makes the critical state a unique state.

Thornton and Barnes (1986b) reported 2D simulations of quasi-static shear deformation of a compact (dense) polydisperse system of 1000 discs using the BALL code, in which two biaxial tests (constant mean stress and constant volume) were examined in detail. The results showed that the evolution of induced structural anisotropy and angle of internal shearing resistance is unique for the the two tests. Visualisations of the force transmission patterns obtained under isotropic and anisotropic stress states were also provided. Thornton and Sun (1993) reported simulations of 3D axisymmetric compression using two different interparticle friction coefficients, specified for both a dense and a loose system, with no interparticle adhesion. The results showed that an increase in the interparticle friction resulted in an increase in shear modulus and shear strength for both systems and also resulted in a higher degree of induced structural anisotropy and higher rates of dilation. Both tangential and normal contact-force contributions to the deviator stress (called deviatoric stress in general) increased with increasing interparticle friction, but the tangential contribution is still very small compared with the normal contribution. It was also observed that when the interparticle friction was increased both the ratio of sliding contacts and the critical mechanical coordination number decreased. Simulations of a constant deviatoric strain test and a multi-axial plane strain test were reported by Thornton (2000). General 3D stress probes were first examined by DEM and the failure criterion proposed by Lade and Duncan (1975) was first confirmed by DEM simulations, by Thornton and Sun (1993), and later by Thornton (2000) from different radial deviatoric loadings. A higher angle of internal shearing resistance for axisymmetric extension than for axisymmetric compression was observed in the DEM simulations, which showed that neither Mohr-Coulomb failure criterion nor the failure criterion proposed by Matsuoka and Nakai (1974) applies. Further studies of general stress and strain probes have been recently reported by Thornton and Zhang (2006a). Some results of cyclic loading tests were reported by Thornton and Sun (1994), of which qualitative macroscopic behaviour is in agreement with real sand.

Thornton and Antony (2000) reported the results of DEM simulations of quasi-static shear deformation for a hard and a soft system respectively and a comparison was made. Thornton and Antony (1998) examined and demonstrated the existence of strong- and weak- force transmission subnetworks first proposed by Radjai et al (1996) and Thornton

(1997), in which a strong subnetwork of contacts transmitting above-average contact forces and a weak subnetwork of contacts transmitting below-average contact forces existed. By examining the evolution of the separate contributions of the strong and weak subnetworks to the partitioned stress tensor (isotropic and deviatoric parts) and the partitioned fabric tensor, an important finding was made that the weak force network contributes only to the mean stress and the deviatoric stress can be considered to be solely due to the strong force network.

Thornton and Zhang (2001) reported 2D constant volume numerical simulations of different shear testing devices including biaxial compression, simple shear and direct shear, in which a periodic cell was used in biaxial compression while wall boundaries were used in all “devices”. It was suggested that interpretations of material behaviour based on wall boundary information are not reliable. Masson and Martinez (2001) reported 2D direct shear tests using DEM on both dense and loose systems. Thornton and Zhang (2003) further reported 2D direct shear simulations under constant normal stress conditions using DEM. Futher 3D direct shear simulations were reported by Cui and O’ Sullivian (2006). Thornton and Zhang (2006b) examined shear banding during biaxial compression and simple shear non-coaxial flow rules by DEM. The shear banding was observed and visualized under both wall bounded systems and periodic cell systems. It was concluded that localisation and shear band formation are genuine material behaviour rather than artefacts created by boundary imperfections. It was also demonstrated that the initiation of shear bands is an elastic buckling problem. Results of DEM simulations of simple shear deformation were presented to illustrate the evolution of non-coaxialty, and the corresponding non-coaxialty flow rule was shown to be equivalent to that proposed by Tasuoka et al (1988). At fully developed flow when there is no further change in volume, the stress and strain-rate directions are coaxial and the flow rule is that proposed by Hill (1950), which was also shown to apply to direct shear at the critical state, see Zhang (2003).

2.3.3 Application of DEM in wave propagation and other DEM topics

Transient wave propagation (dynamic response) in granular materials was studied using DEM by Sadd et al (2000) with the aim to link wave propagational behaviours with material microstructure or fabric. With regard to wave propagation, granular materials create a structured wave-guide network through which mechanical energy is transferred. Along a given wave path, the dynamic load transfer is determined by the contact interactions between neighbouring particles, and thus propagational characteristics of wave speed, amplitude attenuation and wave form dispersion are related to the local fabric along established wave paths. The simulation results indicated that wave speed is dependent on the stiffness of the interparticle contacts and the distribution of branch vectors along the propagation direction. Wave amplitude attenuation is also dependent on the number of branch vectors in the direction of propagation. Different normal contact law effects on wave progagation in granular medium was studied using DEM by Sadd et al (1993). The specific normal contact laws included linear, non-linear and non-linear hysteretic contact laws along with velocity proportional damping. The simulation results were compared with experimental data from dynamic photoelastic and strain gage experiments. It was found that only the non-linear hysteretic contact law can model the dispersion characteristics reasonably, although all the three contact laws can model the wave speed and amplitude attenuation well.

Other applications of DEM can be found in the literature. DEM has been used in massively parallel computing by Meegoda and Washington (1994), O'Connor (1996); has been applied to unsaturated soils by Jiang et al (2004); has been evaluated by modern X-Ray computer tomography imaging technique by Fu (2005); has been combined with the finite element method (FEM) by Komodromos and Williams (2004), Onate and Rojek (2004); has been combined with the boundary element method (BEM) by Bray (1987); has been coupled with a fluid flow to study undrained behaviour of granular soils by Bonilla (2004).

2.4 Micromechanical descriptors

Some state variables frequently used in micromechanics will be defined below.

2.4.1 Stress tensor (Thornton and Barnes, 1986b)

The statistical average stress tensor (without body forces) for a volume V^p occupied by a single particle is defined as

$$< \sigma_{ij}{}^{p} > = \frac{1}{V^{p}} \int \sigma_{ij} dV^{p} = \frac{1}{V^{p}} \int x_i t_j dS \tag{2.2}$$

If we consider the tractions t_j to consist solely of discrete forces F_j acting at point contacts defined by the coordinates x_i (referenced to the particle centre) then the integral in (2.2) may be replaced by a summation over the n contacts for the particle p. Thus

$$< \sigma_{ij}{}^{p} >= \frac{1}{V^{p}} \sum_{1}^{n} x_i F_j \tag{2.3}$$

The average stress tensor for a volume V of material is defined as

$$< \sigma_{ij} >= \frac{1}{V} \int \sigma_{ij} dV \tag{2.4}$$

But, since the stresses are not continuously distributed within the assembly ($\sigma_{ij} = 0$ in the voids) we may replace (2.4) by

$$< \sigma_{ij} >= \frac{1}{V} \sum_{1}^{m} \sigma_{ij}{}^{p} V^{p} \tag{2.5}$$

where the assembly consists of m particles.

Combining (2.3) and (2.5) we therefore define the macroscopic stress tensor as

$$< \sigma_{ij} >= \frac{1}{V} \sum_{1}^{m} \sum_{1}^{n} x_i F_j \tag{2.6}$$

Noting each contact contributes to (2.6) twice, for systems of equal-sized spheres we may replace (2.6) by

$$< \sigma_{ij} >= \frac{2}{V}\sum_{1}^{C} x_i F_j \tag{2.7}$$

where there are C contacts in the assembly.

For polydisperse systems, (2.6) is written as

$$< \sigma_{ij} >= \frac{1}{V}\sum_{1}^{C} (x_i{}^a F_j{}^{ab} + x_i{}^b F_j{}^{ba}) \tag{2.8}$$

$x_i{}^a, x_i{}^b$ are the coordinates of a contact referenced to two different particle centres respectively on which the contact is acting on, $F_j{}^{ab}$ is the corresponding contact force acting on particle a by particle b, and $F_j{}^{ba}$ is the corresponding contact force acting on particle b by particle a .

For spheres (or discs), $x_i = Rn_i$, $F_j = N_j + T_j$, $N_j = Nn_j$, $T_j = Tt_j$

where R is the radius of the particle, n_i defines the contact normal vector, t_i defines the direction of the tangential displacement vector at the contact, and $n_i t_i$=0. Therefore, (2.8) can be written as

$$< \sigma_{ij} >= \frac{1}{V}\sum_{1}^{C} [(R^a + R^b)Nn_i n_j + (R^a + R^b)Tn_i t_j] \tag{2.9}$$

which is the form used in the calculation of the stress tensor for the simulations reported in this thesis.

The average stress tensor defined by (2.9) is a ‘partitioned’ form, considering the contributions of the contact normal force and tangential force respectively, derived from Thornton and Barnes (1986b). Other ‘partitioned’ forms can be found in detail in Cundall and Strack (1983), and Rothenburg and Bathurst (1989).

Other noteworthy definitions of the average stress tensor can be found in Christoffersen et al (1981), Rothenburg (1980), Rothenburg and Selvadurai (1981), Mehrabadi et al (1982), Bagi (1996), and Kruyt and Rothenburg (1996).

2.4.2 Coordination number

The coordination number is an alternative parameter to the contact density, and is directly related to the structural stability of the assembly concerned. The apparent coordination number is defined as the average number of contacts per particle and expressed as

$$Z_a = \frac{2C}{N} \tag{2.10}$$

where C is the number of contacts and N is the number of particles. Numerical simulations have revealed that, at any time during shear, there are some particles with no contacts and some particles with only one contact. None of these particles contribute to the stable state of stress. Hence, a mechanical coordination number is defined by Thornton and Sun (1993) as

$$Z_m = \frac{2C - N_1}{N - N_1 - N_0}, Z_\mathrm{m} \geq 2 \tag{2.11}$$

where N_1 and N_0 are the number of particles with one or no contacts respectively.

2.4.3 Fabric tensor

In Oda (1972, 1978), fabric (which means the spatial arrangement of solid particles and associated voids) is explained by orientation fabric and packing density. Orientation fabric is quantitatively defined by vector mean direction and vector magnitude to characterize orientation of non-spherical particles. Packing (which means mutual relation of individual particles to other ones) is defined by the probability density function of contact normals, mean coordination number and deviation of coordination number. Therefore fabric in a broad sense includes coordination number. Rothenburg et al (1989) have also pointed out that a physically adequate constitutive model for granular materials must be able to describe a complex set of phenomena related to the evolution of microstructure (fabric) during shear deformations.

Satake (1982) suggested that for disc or sphere assemblies, the distribution of contact normals n_i (also termed as structural anisotropy) could be characterized by a fabric tensor ϕ_{ij} where

$$\phi_{ij} = \frac{1}{2C}\sum_{1}^{2C} n_i n_j = \frac{1}{C}\sum_{1}^{C} n_i n_j \tag{2.12}$$

The fabric tensor ϕ_{ij} defined above was originally used to describe the orientation of the distribution of contact normals or structural anisotropy. However, the general form of (2.12) can be used to define other types of anisotropy associated with non-spherical particles, e.g. distribution of the orientation of the long axes of elliptical particles, see Oda (1999).

Oda et al (1982) combines the structural anisotropy defined by (2.12) and the packing density and defined a fabric tensor

$$F_{ij} = F_{kk}\phi_{ij} \tag{2.13}$$

where $F_{kk} = \frac{2C\overline{R}}{V}$ (2.14)

and $\overline{R}$ is the mean particle radius. F_{ij} appears to be a satisfactory method to characterize the complete microstructure of granular materials.

The fabric tensor defined by (2.12) is a symmetrical second order tensor, which has three principal values as a stress tensor or strain tensor does. Like stress and strain tensors, a principal fabric space and a Mohr fabric circle can also be identified. According to (2.12), the principal fabric values of ϕ_{ij}, termed as ϕ_i, has the following properties

$$\phi_1 + \phi_2 + \phi_3 = \phi_{11} + \phi_{22} + \phi_{33} = 1 \text{ (for 3D)} \tag{2.15}$$

or

$$\phi_1 + \phi_2 = \phi_{11} + \phi_{22} = 1 \text{ (for 2D)} \tag{2.16}$$

(2.15) and (2.16) show that the principal values of fabric are not independent of each other.

For isotropic structure (uniform distribution of n_i) of granular materials,

$$\phi_1 = \phi_2 = \phi_3 = \frac{1}{3} \tag{2.17}$$

or, in 2D,

$$\phi_1 = \phi_2 = \frac{1}{2} \tag{2.18}$$

For an axisymmetric condition,

$$\phi_1 > \phi_2 = \phi_3 \tag{2.19}$$

So for 3D axisymmetric conditions, a deviator fabric defined by $(\phi_1 - \phi_3)$ has been used to describe the degree of structural anisotropy by Thornton and Sun (1993). Bardet (1994) used the fabric ratio defined by $\frac{\phi_1}{\phi_2}$ to describe structural anisotropy for 2D biaxial conditions. Rothenburg and Bathurst (1989) and Sitharam et al (2002) used the second-order coefficient of contact normal anisotropy to describe induced anisotropy.

Other complex forms of fabric tensor can be found in Nemat-Nasser and Mehrabadi (1983). A fourth-order or higher order fabric tensor can also be defined (see Oda 1999, Thornton and Barnes 1986a), where more information can be obtained.

2.5 Summary

The Discrete Element Method, since its inception, has been developed from 2D to 3D, from simple linear contact law to complex Mindlin and Deresiewcz (1953) type laws, and from wall boundaries to periodic cells. In addition it has developed from using purely circular particle shapes to elliptical shapes and to other more complex shapes, including developing interactions between particle to particle to interactions between clusters. Adhesion, viscous liquid bridges and plastic dissipation at the inter-particle contacts have also been implemented into DEM (see Thornton 1999). It has been used to simulate biaxial tests, direct shear, simple shear, triaxial shear tests plus general 3D shear tests. It has been used to study the behaviour of granular materials at low stress levels to particle crushing behaviour at high stress levels. It has also been used for the study of shear bands.

From the literature review, DEM has been used to model geotechnical tests by many researchers. Both macroscopic and microscopic behaviour have been explored. Strain hardening, and softening and critical state behaviour has been well captured for dense samples under drained conditions. The effects of particle shape, particle rotation and friction coefficient have also been modelled and the relationships well documented. However, most simulations are drained tests and not undrained tests, and most systems simulated are dense not loose, except Sitharam et al (2002). In addition, most simulations are of axisymmetric compression or biaxial tests, not plane strain tests. Therefore, the behaviour of granular materials for loose particle systems has not been well captured, especially under undrained conditions. The explanation of liquefaction has also not been well explored. Furthermore, the difference between axisymmetric compression and plane strain behaviour has not been well explored. Therefore, this thesis will focus on the behaviour of loose samples especially liquefaction under undrained conditions.

CHAPTER 3: DRAINED AXISYMMETRIC COMPRESSION SIMULATIONS

3.1 Introduction

The triaxial test is one of the most repeatable and useful laboratory tests for determining the stress-strain-dilation characteristics of soils. It is more reliable than the unconfined compression test and the direct shear test (Bardet 1997). Due to its relative simplicity, its versatility, and the degree of controlled deformation that it allows, the triaxial test has become one of the most widely used apparatuses for the testing of soil specimens, both for research and routine practical purposes. In a standard laboratory drained triaxial experiment, an axisymmetric compression test is usually performed under constant cell pressure conditions, which means that the minor principal stress σ_3 ($\sigma_2 = \sigma_3$) is maintained at a constant value and failure results from the increase in the major principal stress (axial stress) σ_1 under conditions of full drainage. The rate of loading or deformation is so arranged that negligible excess pore pressure is generated in the specimen at any time during the application of the axial load and particularly at failure. The starting point before drained shear can be at an isotropic stress state or an anisotropic stress state, which is usually obtained in laboratories after isotropic consolidation or anisotropic (such as K_0) consolidation respectively. The isotropically consolidated drained triaxial compression test is more frequently performed in laboratories, which is often called CD or CID tests. During drained tests, there is no excess pore pressure generated, and the effective stresses and total stresses can be taken to be equal. Cohensionless materials such as sand are actually often tested dry as it simplifies the laboratory procedure. The behaviour of dry cohensionless soil is virtually identical with the drained behaviour of cohensionless saturated soil (Lambe and Whitman 1979). The details of conventional triaxial tests can be found in Bishop and Henkel (1957) and Head (1986). In the drained DEM simulations with constant mean stress conditions reported in this chapter, dry particles are used corresponding to the dry specimens in the laboratory. The DEM simulation results are comparable to those of CD tests for dry samples or fully saturated samples.

In this chapter, published literature on axisymmetric compression in both laboratory work and DEM work is reviewed briefly in section 3.2. Simulation details of parameters, boundary conditions, control modes used in the DEM simulations and especially on how to prepare samples of different porosities is described in section 3.3. Simulation results and discussions of the DEM drained tests are provided in section 3.4. Finally, a summary is given for the chapter.

3.2 Literature review

3.2.1 Drained behaviour

Bishop (1966) demonstrated the stress-strain-dilation behaviour of Ham River sand in drained triaxial tests. He pointed out that, for loose sand the reduction in volume during shear rose rapidly with increase in σ_3 up to about 6.89 MPa, and then more gradually as σ_3 was increased to 27.58 MPa; dense sand (strongly dilatant at low confining pressures) showed almost zero rate of volume change at failure when σ_3 reached 3.45 MPa, and at higher values of σ_3 dense sand showed an increasingly marked reduction in volume during shear until, at σ_3 =6.89 MPa, its behaviour approximated to that of loose sand. Bishop (1966) studied the Mohr envelopes for loose and dense sand and observed a marked curvature of the envelope for the dense samples and its convergence at high stresses with that for loose samples. The difference between the slope of the Mohr envelope for dense sand and loose sand dropped from nearly 5° at σ_3 =0.69 MPa to only 0.2° at σ_3 =6.89 MPa. It was also observed that even for loose sand placed in a very loose state the slope of the Mohr envelope was not independent of the confining pressures, but drops about 3° as σ_3 rises from 0.69 MPa to 6.89 MPa. This drop was closely associated with the rate of volume change at failure. By plotting grading curves during compression and shear, the degree of particle crush can be compared and it was observed that the combined effect of consolidation and shear led to very marked particle breakdown even in a medium to fine sand, and that at high stresses the particle breakdown occurs to a much greater extent during shear stage than during the consolidation stage.

Lee and Seed (1967) investigated drained strength characteristics of sands under elevated confining pressure up to 14 MPa. The soil used for the investigations was mainly Sacramento River sand, which was a fine uniform sand and the particles were mainly feldspar and quartz minerals with subangular to subrounded shapes. They examined the stress-strain-dilation relationship in a series of drained triaxial tests on dense Sacramento River sands, and observed that an increase in σ_3 increased the strain to failure, decreased the tendency to dilate, and reduced the brittle characteristics of the stress-strain curve.

Similar results were obtained for loose Sacramento River sands, the pattern of which was similar to that of the dense sands except that at low pressures the tendency for dilation was not so strong as for the dense sands and the tendency for compression was greater for the loose sands at high pressures. The same void ratio at failure was observed for each confining pressure respectively, independent of the initial void ratios, which was called a "critical void ratio" (for the corresponding confining pressure). The corresponding confining pressure was extensively defined as the critical confining pressure for the corresponding void ratio, under which the soil sample would shear at essentially constant volume in drained triaxial tests for each initial void ratio respectively. Lee and Seed (1967) also investigated the slopes of the Mohr circle envelopes for the peak deviator stresses for the Sacramento River sands (both dense and loose) in drained triaxial tests, and they found that the slope of the Mohr envelope for dense sand changed from about 41° at low pressures (<0.8 MPa) to 24° at the higher pressures (4 MPa). For loose sand, the slope correspondingly changed from 34° to 24°. However, when the confining pressure was above 4 MPa, a straight line envelope developed for dense sand and a slight increase in the slope developed at higher confining pressures. Lee and Seed (1967) also investigated a comparative study of Ottawa sand, which had well-rounded particles and exhibited a high resistance to crushing, which can be confirmed by plotting the gradation of the sands before shear and after shear at different confining pressures. They observed that the failure Mohr envelope for Ottawa sand exhibited a continuous curvature and continued to flatten over full range of confining pressures up to 14 MPa, which was different from that of the Sacramento River sand. This difference between these two sands was attributed to the relatively high crushing resistance of the Ottawa sand. Lee and Seed (1967) recommended four components for the drained shearing resistance of sand, i.e. sliding friction, dilatancy, particle crushing, and rearranging. Friction may be assumed to be essentially constant though it may vary slightly with changes in confining pressure and crushing of particles. At low pressures dilatancy caused a significant increase in angle of friction and accounted for the steep failure envelopes commonly observed for dense sands. Crushing became progressively more important with increasing confining pressures.

Barden and Khayatt (1966) performed drained triaxial tests on River Welland sand, the particle shape of which was a mixture of angular and sub-angular. Both triaxial compression (increasing mean stress p) and extension (decreasing mean stress p) tests were performed and compared under confining pressures of 275.8 kPa and 68.95 kPa respectively. By plotting the peak effective stress ratio against initial porosities (after consolidation), they found that the triaxial extension exhibited higher shear strength than the triaxial compression tests at the confining pressure of 275.8 kPa, but at the confining pressure of 68.95 kPa the two strength values have little difference for similar mean stress at failure. The difference for the triaxial compression and extension tests under the confining pressure of 275.8 kPa was attributed to the particle crushing of the compression tests. Barden and Khayatt (1966) proposed that the strength in triaxial compression and extension be equal for equal porosity at failure. The peak points in various tests were studied to assess the failure criteria, and Barden and Khayatt (1966) showed that the extended von Mises and Tresca criteria are not applicable to sands for theoretical reasons alone, while the Mohr-Coulomb criterion gives a more reliable prediction.

Yamamuro and Lade (1996) as well as Lade and Bopp (2005) investigated the effects of initial relative density on the drained axisymmetic (both compression and extension) behaviour at high pressures up to 52 MPa and 70 MPa respectively. It was found that as the confining pressure increased, particle crushing increasingly influenced the stress-strain and volume change relationships, producing increasing strains to failure and increasingly contractive volume changes. Beyond certain high values of mean normal stress at failure, increasing with initial relative density, the volumetric contraction and strains to failure began to decrease. The Mohr-Coulomb failure envelopes showed the greatest curvature for the highest density, but the failure envelopes merged at high pressures where, due to particle crushing, the relationships between void ratio and isotropic pressure are described by a single curve. The experimental results showed that the rates of dilation at failure and the friction angles are directly related to each other, as has been proposed by many researchers. The friction angles are higher in extension than in compression for lower confining pressures, but a crossover occurs and the friction angles are higher in compression than in extension for higher confining pressures.

Coop (1990) investigated the mechanical behaviour of a typical biogenic carbonate sand (Dogs Bay sand) using triaxial testing at standard and also at high pressures up to 8 MPa. The test results showed that despite the particle breakage which is characteristic of these soils, their behaviour was still qualitatively similar to that observed for more commonly encountered soils, and was consistent with the principal features of critical state soil mechanics. The higher stresses used in the tests were an order of magnitude greater than were generally used in soil testing, and the values of some individual soil parameters such as the friction angle at critical state and other Cam clay model parameters were found to be outside the range of normal experience. Micrographic and grading analyses were used to examine the influence of the isotropic and shear stresses on particle breakage and particle crushing was found even at relatively low stresses. Coop and Atkinson (1993) investigated the mechanical behaviour of artificially cemented carbonate sand using triaxial testing at confining pressures up to 9 MPa. The results showed that an important effect of cementing was a reduction in specific volume resulting from the increase in fine contents. This influences both the stress-strain behaviour and the peak strength at strains beyond those required to fracture the cement bonding. Comparisons between the behaviour of the cemented and uncemented soils should therefore be carried out on samples with the same grading. For cemented samples it was possible to identify a yield curve outside the state boundary surface of the uncemented soil. A framework for the behaviour was defined which depended on the relative magnitudes of the confining pressure and cement bond strength, which was found to be extensively applicable to a natural calcarenite and may be applicable to other cemented soils. Cuccovillo and Coop (1999) investigated the behaviour of two natural sands by means of triaxial testing over a wide range of pressures. One material had bonding as the principal element of its structure and the other fabric. It was suggested that structure should be considered as an element of the nature of a sand in addition to properties such as mineralogy, particle shape and grading. While bonding results in a cohesive mode of shearing, it was demonstrated that when fabric dominates, the shearing behaviour remained predominantly frictional, although the rates of dilation and peak strengths may be very much higher than for the reconstituted soil at the same stress-volume state. It was suggested that it is not necessarily the position of state of the soil relative to the critical state line that distinguishes strain hardening and softening behaviour, but the proximity to the boundary determined in isotropic compression.

3.2.2 Numerical simulations

Early DEM simulations were restricted to 2D arrays of discs. The first DEM simulations of triaxial compression tests were reported by Cundall (1988), who introduced the concept of periodic boundaries in DEM simulations. Cundall (1988) showed that the stress-strain-dilation behaviour for different sample sizes (number of particles) was quite similar under constant mean stress simulations using a periodic cell. He also showed numerical results for dense systems that were qualitatively comparable with those of physical tests reported by Ishibashi and Chen (1988).

Thornton and Sun (1993) reported 3D axisymmetric compression results for dense and loose systems, and showed that the simulated behaviours were in qualitative agreement with those of real experiments reported for glass ballotini. They showed that the mobilised shear strength was primarily a function of the normal contact force contribution to the stress tensor and the tangential contact force contribution was less than 10%, the conclusion of which was independent of the interparticle friction coefficient used, see also chapter 2. They proposed that the critical void ratio should depend on the interparticle friction used.

Thornton and Antony (1998) showed stress-strain-dilation behaviours in qualitative agreement with real sand for axisymmetric compression simulation tests. They examined and demonstrated the existence of strong- and weak- force transmission subnetworks. By examining the evolution of the separate contributions of the strong and weak subnetworks to the partitioned stress tensor (isotropic and deviatoric parts) and the partitioned fabric tensor, an important finding was made that the weak force network contributes only to the mean stress and the deviatoric stress can be considered to be solely due to the strong force network, see also chapter 2. Thornton and Antony (2000) reported axisymmetric (both compression and extension) simulations on a soft (E = 70 MPa instead of 70 GPa for a hard system) particle system of 8000 spheres with interparticle friction and adhesion and showed that the mechanical behaviour (macroscopic and microscopic) for the soft system is qualitative similar to that of the hard system reported by Thornton and Antony (1998) for axisymmetric compression conditions. It was found that the shear strength was mainly due to strong force network and the weak network's contribution to shear strength was very small for both compression and extension simulation tests for a soft system, the conclusion of which had been confirmed in Thornton and Antony (1998) for hard systems under axisymmetric compression.

Ng and Dobry (1994) presented drained monotonic triaxial compression simulation tests under constant mean stress for a system with 398 spheres of three different particle sizes in a periodic cell. They studied the influence of interparticle friction and particle rotation, and concluded that a larger microscopic friction angle (interparticle friction coefficient), as well as inhibited particle rotation, produced a higher shear strength, a higher initial modulus and stronger dilation. They observed that the macroscopic friction angle had a linear relationship with the microscopic friction angle, which was in agreement with Rowe (1962) but not with Thornton (2000).

Sitharam et al. (2002) performed traditional drained triaxial simulation ($\sigma_2 = \sigma_3 =$ constant) for both a dense and a loose system on 3D assemblages of polydisperse spheres in a periodic cell using DEM to study the evolution of the internal variables such as average coordination number and induced anisotropy during deformation along with the macroscopic behaviour, see also chapter 2.

Instead of spherical particles, ellipsoidal particles were incorporated into the DEM code by Lin and Ng (1997) as well as Ouadfel (1998). Lin and Ng (1997) performed traditional triaxial compression simulations using a periodic cell with systems of spheres as well as ellipsoids (both mono-sized) in order to study the influence of particle shape. They found that the system of ellipsoids achieved lower porosity and larger coordination number under the same consolidation procedure. They also found that higher shear strength, larger initial modulus, more dilation and less particle rotation were exhibited by the system with ellipsoids in the triaxial compression. Ng (2001) performed drained triaxial compression using the program by Lin and Ng (1997) for systems of ellipsoids with different aspect ratios (major/minor axis of the ellipsoidal particle), and the results indicated that particle shape did not influence shear strength at large strain, but influenced volume change.

3.3 Simulation details

In all the simulations mentioned in section 3.2, only Sitharam et al. (2002) observed obvious contractive volume change for a loose system. So it is desirable to generate a very loose sample (or looser samples) in DEM simulations and it is necessary to simulate a variety of samples from very dense to very loose systematically. In the work reported in this thesis different sample preparation procedures were developed to create samples at an isotropic stress of 100 kPa with a range of porosities from 0.362 to 0.425.

All the samples presented in this thesis consist of 3600 elastic spherical particles with no adhesion. The Young's modulus and Poisson's ratio for each particle are E = 70 GPa and $\upsilon = 0.3$, respectively. The interparticle friction coefficient during shear tests is $\mu = 0.5$. Nine different sizes of spheres were used: 0.25 mm (2), 0.26 mm (20), 0.27 mm (220), 0.28 mm (870), 0.29 mm (1376), 0.30 mm (870), 0.31 mm (220), 0.32 mm (20), 0.33 mm (2), with an average particle diameter of 0.29 mm (the actual number of particles is given in brackets). The notional density of each particle is 2650 kg/m^3, which is scaled up by a factor of 5×10^{12} in order to perform quasi-static simulations within a reasonable timescale. Such density scaling will not affect the quasi-static stress-strain behaviour (Thornton 2000). The time step used in the simulations is based on the minimum particle size and the Rayleigh wave speed (Thornton and Randall 1988). Cundall and Strack (1979b) introduced global and contact damping in order to dissipate sufficient kinetic energy. In the DEM simulations presented in this thesis, only contact damping is used; and no gravity field is applied.

The particles were randomly generated as a ‘granular gas’ in a specified periodic cell with an initial cuboidal size of 1.74 mm to provide an assembly with a porosity of 0.676 and no interparticle contacts. During the simulation of isotropic compression starting from the “granular gas”, a servo-control (see Appendix A) was introduced to maintain a desired stress level.

Sample preparation for DEM is a time-consuming process. In order to achieve a system which could be used for subsequent shear simulations, the isotropic compression was carried out in stages, increasing the isotropic pressure from 0 kPa to 0.1 kPa, 1 kPa, 10 kPa, 50 kPa, 90 kPa and finally 100 kPa. It is not easy to obtain a very loose sample with an isotropic stress of 100 kPa, because it takes a large number of steps during the isotropic compression stage to compress the initially generated ‘granular gas’ system with an isotropic stress of only 0.1 kPa so that sufficient contacts can be established in the system, i.e. a sample with a certain value of isotropic stress is formed. Consequently, this sample will be much denser than the initial ‘granular gas’ in terms of porosity.

A computational trick was used to overcome this difficulty, i.e. the particle rotations were prevented during the very early isotropic compression stage. Without particle rotation the assembly is stiffer and more resistant to the isotropic compression, and therefore a very loose sample may be formed. For other medium loose samples, the interparticle friction can also be adjusted in order to obtain a sample with required values of porosity. The details are provided as follows:

In order to create a dense system for subsequent shear simulations, the interparticle friction was set to zero during the isotropic compression stage until the isotropic stress was 90 kPa. The interparticle friction was then set to μ=0.5, which is the value used in the subsequent shear simulations. In this way, the densest sample was created with a porosity of 0.362 at an isotropic stress of 100 kPa. Like the process for obtaining the densest sample, if an interparticle friction of 0.2 was used first, and then changed back to 0.5 when the isotropic stress was 90 kPa, a dense sample (but looser than the previous sample) with a porosity of 0.389 was obtained at an isotropic stress of 100 kPa. If the interparticle friction was set to other values (see Table 3.1) during the early isotropic compression stage and then set to 0.5 when the isotropic stress approached 90 kPa, a series of samples (sample 3 to sample 7) were similarly created, see Table 3.1. In order to create an even looser sample (porosity > 0.419), particle rotations were prevented during the very early isotropic compression stage until the isotropic stress was 1kPa. During all the later isotropic compression stages, the particles were permitted to rotate. In this way the loosest sample was obtained. In table 3.1, μ_i means the interparticle friction value used in the early isotropic compression stages (for sample 6 and sample 8, the interparticle friction values at all isotropic compression stages are the same as those used for the subsequent shear). For sample 8, 'no rotation' in the column of μ_i means there was such a process at the very early isotropic compression stage in which the particle rotations of the assembly were prevented. In Table 3.1, the values of porosity, Z_m, stresses and fabrics are those at the end of isotropic compression (p= 100kPa), and therefore correspond to the initial values for the subsequent shear stage.

In order to perform drained axisymmetric compression simulations at a constant mean stress of 100 kPa for each sample listed in Table 3.1, a servo-control was used (see Appendix A) to keep the mean stress constant, and the initial specified strain-rates in the three principal directions were set to be $\dot{\varepsilon}_1 = 1\times 10^{-5} s^{-1}$, $\dot{\varepsilon}_2 = \dot{\varepsilon}_3 = -5\times 10^{-6} s^{-1}$, respectively, where positive means compressive strain.

During shear, strain increments are computed directly from the lengths of the sides of the periodic cell. As the principal strain directions do not rotate (a result of the imposed conditions), the change of the three principal strains in a time step Δt can be obtained as follows:

Table 3.1 Information for the initial systems

sample	μ_i	porosity	Z_m	stress (kPa)			fabric		
				σ_{11}	σ_{22}	σ_{33}	ϕ_{11}	ϕ_{22}	ϕ_{33}
1	0	0.362	5.75	100.6	100.1	99.6	0.334	0.335	0.331
2	0.2	0.389	5.62	100.0	98.4	102.0	0.331	0.330	0.339
3	0.3	0.405	5.39	101.7	98.3	99.2	0.335	0.328	0.337
4	0.35	0.407	5.20	99.9	100.0	100.4	0.334	0.331	0.335
5	0.4	0.409	5.12	100.3	100.3	99.0	0.333	0.330	0.337
6	0.5	0.414	5.10	101.6	100.7	97.7	0.337	0.331	0.332
7	0.6	0.419	5.03	101.8	98.7	98.3	0.336	0.332	0.332
8	0.5 (no rotation)	0.425	4.76	103.0	99.6	97.8	0.334	0.331	0.335

$$\Delta\varepsilon_i = \frac{l_i^t - l_i^{t+\Delta t}}{l_i^{t+\Delta t}} \qquad (i = 1, 2, 3) \tag{3.1}$$

where, l_i is the dimension of the periodic cell n the $i\,(i = 1,2,3)$ direction at times t and $t + \Delta t$. The strains are then calculated from the initial isotropic stress state when the strains are taken to be zero, by using

$$\varepsilon_i = \sum \Delta\varepsilon_i \qquad (i = 1, 2, 3) \tag{3.2}$$

which corresponds to natural strains.

3.4 Simulation results

The simulation results and discussions include both the macroscopic and microscopic behaviour. ‘Macroscopic’ behaviour here means an averaged response dealing with the system as a continuum, as is measured directly or indirectly in conventional triaxial tests. The macroscopic behaviour considered includes the evolution of the deviator stress, volumetric strain, porosity and sinφ. ‘Microscopic’ behaviour here means a response that cannot be measured in conventional triaxial tests, and can only be obtained when treating granular media as a discontinuum. The microscopic behaviour includes the evolution of the structural anisotropy, mechanical coordination number, and percentage of sliding contacts.

3.4.1 The macroscopic behaviour

Figure 3.1a shows the deviator stress ($q = \sigma_1 - \sigma_3$) plotted against deviator strain for all samples. In the case of the densest sample (n = 0.362, n refers to porosity here) there is a pronounced peak deviator stress of about 103 kPa attained at a deviator strain of 7%. Fig. 3.1b is a refined plot of Fig. 3.1a at smaller strains. Before the peak, the deviator stress

increases as the deviator strain increases, corresponding to strain hardening. After the peak, the deviator stress decreases as the deviator strain increases, corresponding to strain softening. At large strains the deviator stress remains constant at a value of 74 kPa. For the medium dense sample (n = 0.389), a maximum deviator stress of 81 kPa is attained at a deviator strain of 5%. This is followed by a small gradual reduction until a constant value of 74 kPa is reached at large strains. For all the loose samples (n = 0.405 to n = 0.425), allowing for the fluctuations, the maximum deviator stress occurs at large strains and there is no significant occurrence of a peak deviator stress prior to this. At small deviator strains (smaller than 5%) during the strain hardening process, a denser sample exhibits stiffer behaviour than a looser one, or it can be said that the shear modulus during strain hardening is dependent on the initial porosity of the sample, see Fig. 3.1b. All the samples reach a unique value (74 kPa) of deviator stress at large strains, which is independent of the initial porosity. Fig. 3.1a shows there are fluctuations on the stress-strain curve, which is mainly because of the limited number of particles used for the system. Cundall (1988) showed that as the number of particles increased the stress-strain curve would become smoother.

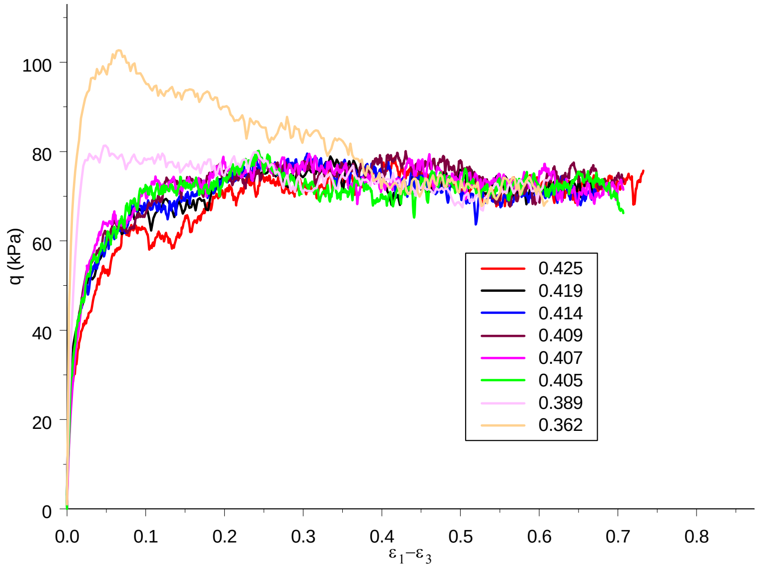

Fig. 3.1a Evolution of deviator stress (whole range)

[key refers to porosity]

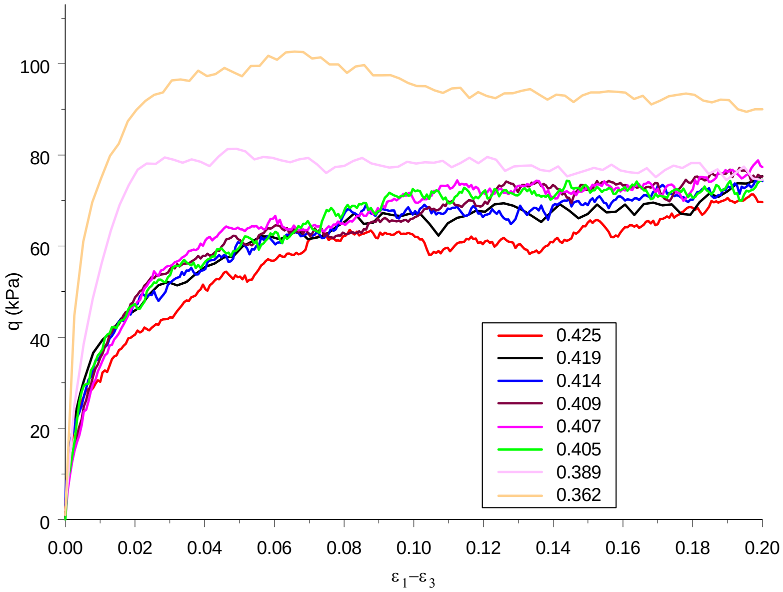

Fig. 3.1b Evolution of deviator stress (small strain range)

[key refers to porosity]

Figure 3.2 shows volumetric strain plotted against deviator strain, where it can be seen that volumetric strain decreases with increasing deviator strain until it remains constant at large strains for the two dense samples, and that volumetric strain increases with increasing deviator strain until it remains constant at large strains for the three very loose samples. For the three medium loose samples, the volumetric strain first increases a little with deviator strain before decreasing a little to a steady value at large strains (with a deviator strain of over 60%). From Fig. 3.1a and Fig. 3.2, at large strains, both q and ε_v remain constant for each sample and in soil mechanics the sample is said to have reached critical state, see Schofield and Wroth (1968) and Muir Wood (1990). It can be said that at critical state, volumetric strain remains constant at different values for the different samples because of different initial porosities. It can also be seen that the decreasing rate of volumetric strain for the dense sample is larger than that for the medium dense sample from the beginning till the critical state, and that the increasing rate is the largest for the loosest sample. At critical state, the rate of change of volumetric strain remains zero for all the samples.

The evolution of volumetric strain and evolution of porosity is completely related by

$$\varepsilon_v^t = \ln \frac{1-n_t}{1-n_0} \tag{3.3}$$

where n_0 is the initial porosity at isotropic state, n_t is the porosity at current strain and ε_v^t is the volumetric strain corresponding to n_t.

Figure 3.3 shows porosity plotted against deviator strain, where it can be seen that porosity increases with increasing deviator strain until it reaches constant at critical state for the two dense samples, and that porosity decreases with increasing deviator strain until it remains constant at critical state for the three very loose samples. For the three medium loose samples, the porosity first decreases a little and then increases a little until it remains constant at critical state.

It can also be seen that the increasing rate of change of porosity for the densest sample is larger than that for the medium dense sample from the beginning, and that the decreasing rate of change is largest for the loosest sample. When porosity increases expansion occurs, and when porosity decreases contraction occurs. It can be said that expansion occurs for the dense samples during shear, and contraction occurs first then expansion occurs for the medium loose samples during shear, and contraction occurs for the very loose samples during shear. The initial expansion rate is dependent on the initial porosity which increases with decreasing porosity. For the dense samples, a decreasing rate of expansion occurs during shear until zero expansion occurs at critical state. For the very loose samples, a decreasing rate of contraction occurs during shear until zero contraction occurs at critical state.

Figure 3.3 shows there exists a unique value (0.406) of porosity at critical state, which is called critical porosity. It should be mentioned that the critical state concept requires a unique stress-porosity (or stress against void ratio) relationship (called CSL by Roscoe et

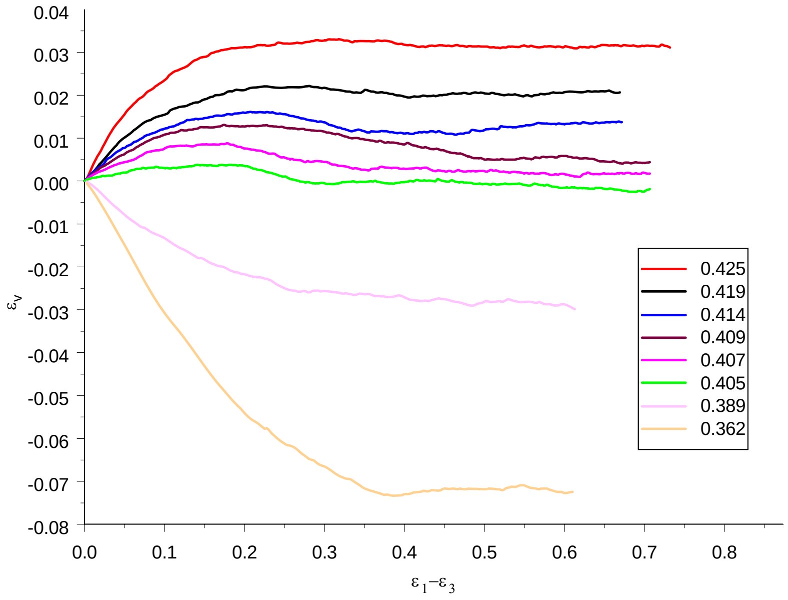

Fig. 3.2 Evolution of volumetric strain
[key refers to porosity]

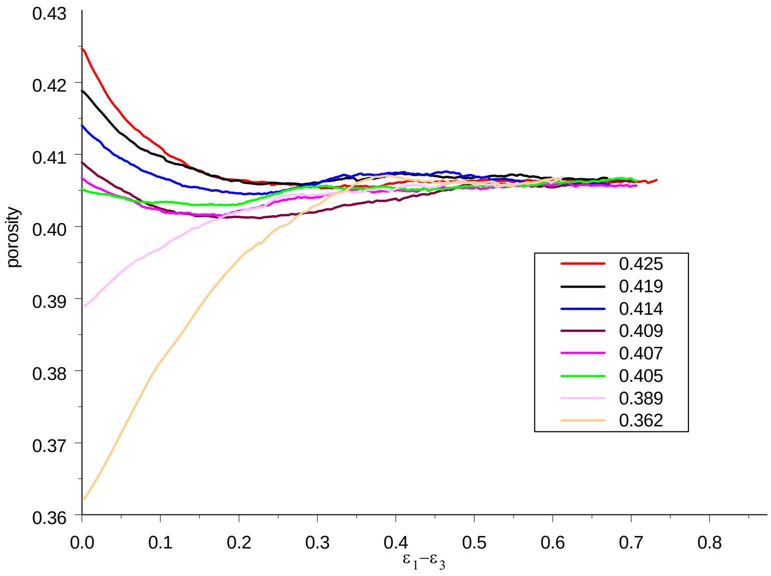

Fig. 3.3 Evolution of porosity
[key refers to porosity]

al. 1958) at critical state in q-p-e space (in drained conditions the effective and total stresses can be taken to be equal), which indicates the existence of a ‘critical void ratio’, independent of initial state, i.e. associated with deformation at constant volume and constant deviator stress for a given mean stress.

From the macroscopic behaviour exhibited by the axisymmetric compression simulations at a constant mean stress of 100 kPa, it has been shown that, at large strains, the deviator stress for all samples is constant with a value of 74 kPa, all samples are deforming at constant volume, and the porosity is 0.406 independent of initial porosity. These facts demonstrate that if the simulations are continued to sufficiently large strains (deviator strain of 70%), the critical state as defined by Schofield and Wroth (1968) can be observed.

Figure 3.4 shows $\sin\varphi$ (φ is sometimes called the mobilised friction angle or the angle of internal shearing resistance) plotted against deviator strain, where it can be seen that the trend of $\sin\varphi$ is similar to that of q. It can be easily shown by using $q = \sigma_1 - \sigma_3$ and $p = (\sigma_1 + 2\sigma_3)/3$ that $\sin\varphi$ is a monotonic increasing function of q, which can be expressed by $\sin\varphi = 3q/(6p+q)$. The peak value of $\sin\varphi$ (or φ) or the value at critical state is often used to describe the shear strength, see Cornforth (1964) and Bolton (1986) among others).

The peak values of $\sin\varphi$ for the densest and medium dense samples are 0.44 and 0.36

respectively. The unique value of sinφ for all samples at large strains is 0.33.

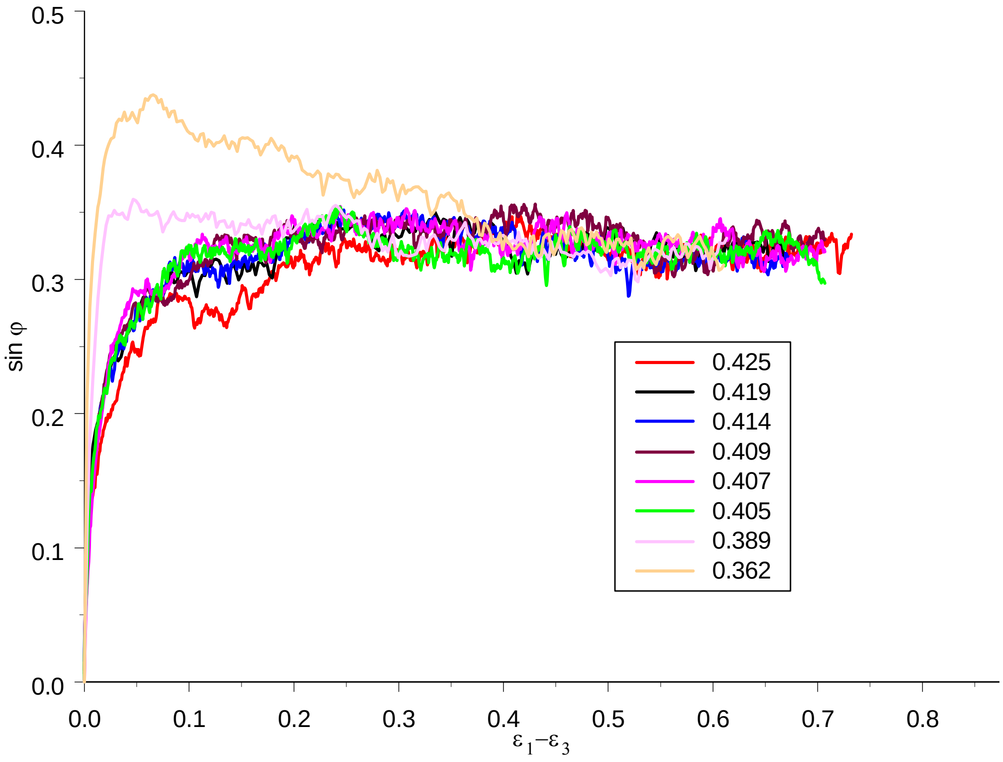

Fig. 3.4 Evolution of sinφ

[key refers to porosity]

3.4.2 The microscopic behaviour

Figure 3.5 shows the deviator fabric plotted against deviator strain. It was found in these simulations of axisymmetric compression tests, ϕ_2 is approximately equal to ϕ_3. So the deviator fabric (ϕ_1 - ϕ_3) can be used to define the structural anisotropy. It can be seen that, for the two dense samples the deviator fabric (structural anisotropy) increases with increasing deviator strain until the deviator fabric reaches a peak, which is dependent on

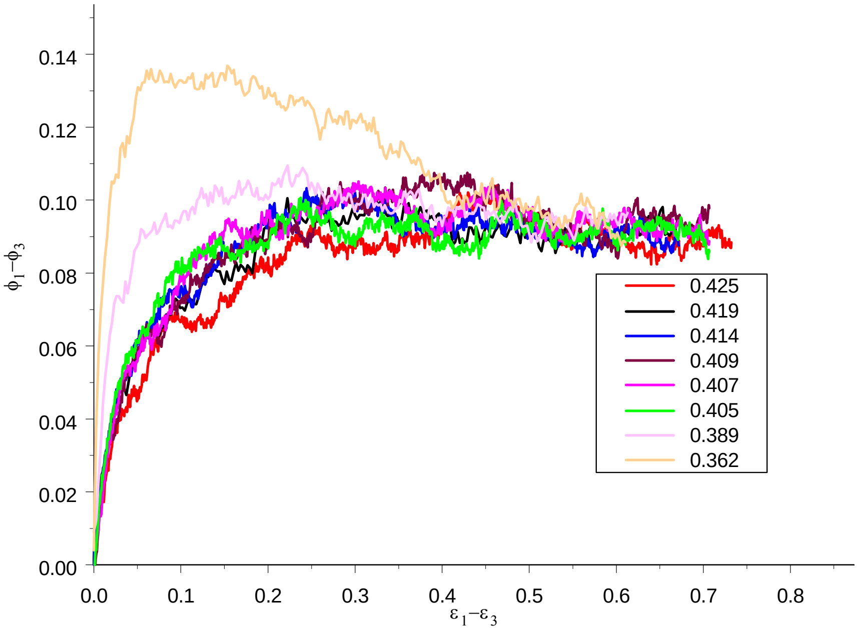

Fig. 3.5 Evolution of deviator fabric

[key refers to porosity]

the initial porosity, then it reduces until an almost steady value is reached at large strains. There is no obvious peak deviator fabric for any of the loose samples. At the critical state both the dense and loose samples have almost the same value of deviator fabric, which can be called the critical deviator fabric. At the beginning of the tests (whether for the dense or loose samples), the deviator fabric is almost zero, see Table 3.1. The structure is isotropic since the initial randomly generated system of particles was subjected to isotropic loading history. As the deviator stress increases (before the peak), the deviator fabric increases. The trend of evolution of deviator fabric is similar to that of deviator stress.

Figure 3.6a shows the mechanical coordination number Z_m (as defined by equation 2.11) plotted against deviator strain. For all the tests, the mechanical coordination numbers always exhibit an initial drop at small strains and remain constant at large strains. Fig. 3.6b is a refined plot of Fig. 3.6a at smaller strains. The initial drop corresponds to an initial loss of number of contacts, which was also observed by Zhang (2003) and Sitharam et al. (2002). For the two dense samples, after the initial drop the mechanical coordination number remains constant at around 4.7, and the evolution of Z_m for the two dense samples is almost identical. For the two loosest samples, after the initial drop the mechanical coordination number increases until it remains constant at around a value of 4.85. In all cases, after a deviator strain of 8%, the mechanical coordination number remains more or less constant. The critical state was observed after a deviator strain of at least 30% from Fig. 3.1. So the state with a constant mechanical coordination number does not imply critical state, but the constant values can be called critical mechanical coordination numbers. It is seen that the critical mechanical coordination number for the two dense samples is approximately 4.7, while for all the loose samples it is approximately 4.85. This observation does not agree with a unique critical coordination number for a given mean stress as suggested by Thornton (2000). Such a deviation is not expected, but at the moment no explanation has been found.

It was suggested by Thornton (1994) that a 'limiting' mechanical coordination number reflects an underlying stability requirement and corresponds, in statistical physics terminology, to a percolation threshold. It was suggested that if the mechanical coordination number drops below the 'limiting' value then local instability occurs which,

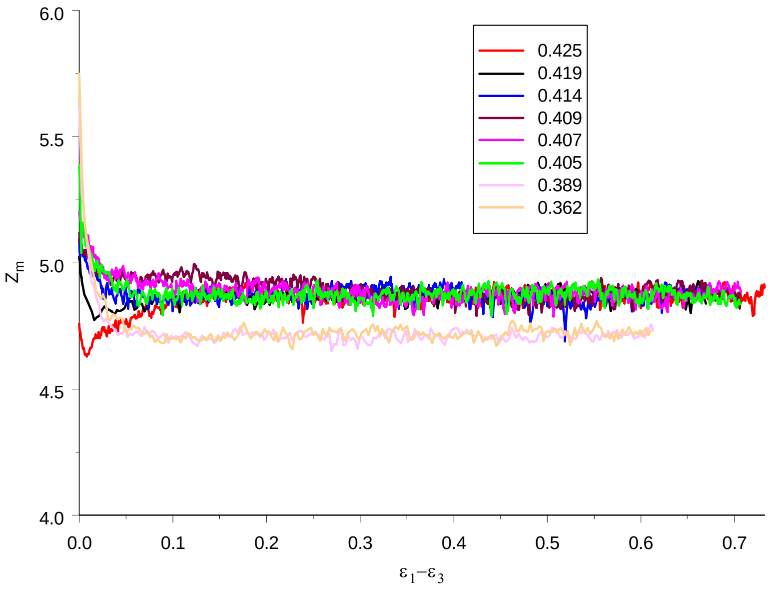

Fig. 3.6a Evolution of mechanical coordination number (whole range)

[key refers to porosity]

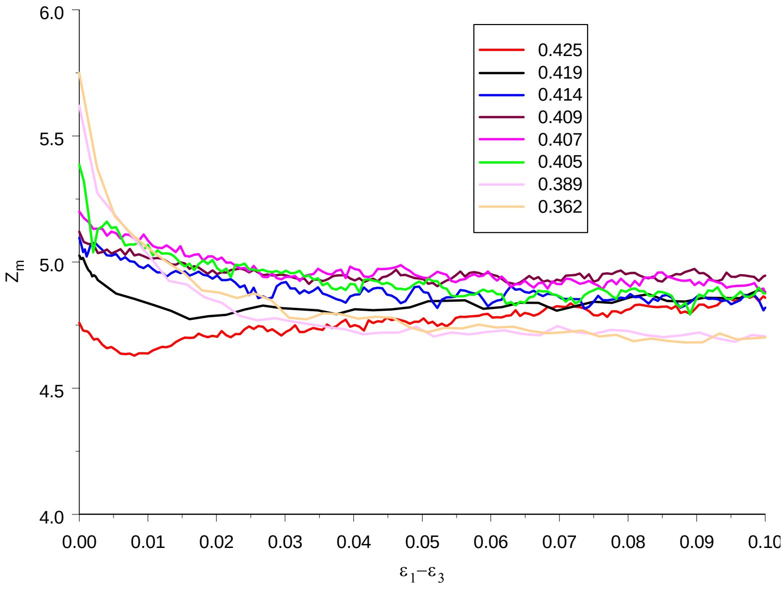

Fig. 3.6b Evolution of mechanical coordination number (small strain range)

[key refers to porosity]

in the presence of boundaries, may result in strain localisation and/or the formation of shear bands.

It can be seen from Fig. 3.6a that, for the two dense systems, the coordination number remained constant during strain softening without any significant drop occurring. This indicates uniform deformation without occurrence of temporary local instabilities and demonstrates that softening is a genuine material behaviour. Vardoulakis (1998) suggested that strain softening was due to the reduction in the number of contacts, but as shown by the results of the two dense samples, this is not the case since the mechanical coordination number remains constant throughout post-peak deformation.

Figure 3.7 shows the percentage of sliding contacts plotted against deviator strain. Only the evolutions for small ranges of deviator strains ($\leq$ 20%) are shown for four samples in order that the differences among the evolutions can be visualized. For the larger ranges of strains ($\geq$ 20%), the evolutions are not much different from those at small ranges (the results are not shown). It can be seen that the dense samples have a relatively smoother evolution, while the loose samples exhibit a fluctuation of percentage of sliding contacts between 0.8% - 6.5%, with an average value of about 4%. Zhang (2003) showed that as porosity increases the amplitude of fluctuation increases, which is consistent with the data presented in Fig. 3.7.

3.5 Summary

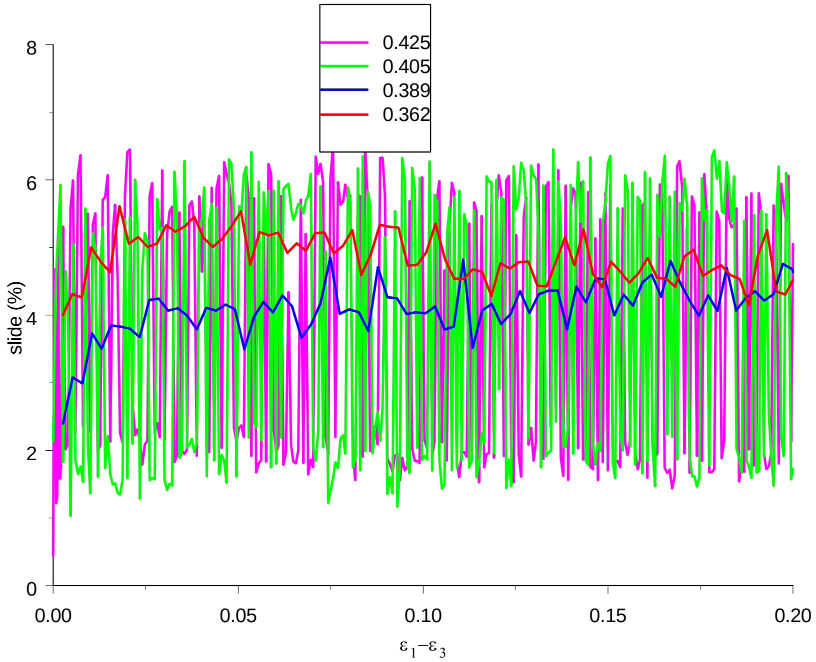

Fig. 3.7 Evolution of percentage of sliding contacts
[key refers to porosity]

This chapter has presented the results of the simulations on a series of samples from very dense to very loose under axisymmetric compression and constant mean stress conditions.

It was observed that both strain hardening and softening occurred for the dense samples, and only hardening (no softening) occurred for the loose samples. It was demonstrated that strain softening is a genuine material behaviour since a uniform specified strain field was applied to the system in a periodic cell, i.e. its existence has nothing to do with the real boundaries although finite boundaries may affect the softening. The peak value of deviator stress was found to be dependent on the initial porosity. A denser sample exhibited a higher peak value of deviator stress. The loose samples do not have an obvious peak deviator stress, so it can be said that a denser sample is both stiffer and stronger.

It was also observed that the dense samples expanded, the very loose samples contracted, and the loose samples initially contracted and then expanded during shear until critical state was reached with a deviator strain of over 60%. At the critical state, all the macroscopic and microscopic parameters remained constant. A critical deviator stress and a critical porosity were found at critical state, both of which were independent of the initial state. Such unique deviator stress and unique porosity are in agreement with the frame work of critical state soil mechanics. The simulation results showed a lower peak and critical state value of sinφ than those for real sand, which can be explained by particle shape, see chapter 2.

CHAPTER 4: DRAINED PLANE STRAIN SIMULATIONS

4.1 Introduction

Plane strain problems occur more frequently than axisymmetric problems in geotechnical engineering. Long structures like embankments, retaining walls and strip footings, with loading in the plane of the cross-section, are frequently approximated to be in plane strain conditions. For such structures, the displacement and strain along the length of the structure are assumed to be zero. The three principal stresses acting in plane strain have different values ($\sigma_1 > \sigma_2 > \sigma_3$), with the intermediate principal stress usually assumed to act along the axis of zero deformation ($\varepsilon_2 = 0$). This is also a general plane strain condition that can be studied using a true triaxial apparatus. Cornforth (1964) stated that a knowledge of plane strain conditions has useful application in basic research, in applied research, and in practice.

The layout of this chapter is as follows. In section 4.2, a literature review of drained plane strain is given for both physical tests and numerical DEM tests. In section 4.3, the simulation details of the initial isotropic samples and simulation parameters used for drained plane strain tests are provided. In section 4.4, the simulation results of drained plane strain are presented and discussed. Finally, in section 4.5, a summary of this chapter is given.

4.2 Literature review

In the conventional plane strain compression apparatus, a specimen enclosed in a membrane is restrained in the direction of the intermediate principal stress σ_2 by using a pair of lubricated rigid platens, bolted together in order to ensure zero lateral strain in one of the principal stress directions and “lubricated” minimises the shear stresses on planes normal to the direction of zero strain. The original form of plane strain apparatus was developed at Imperial College, London, and used by Bishop and Wood. The constructional details were presented by Wood (1958). This apparatus was later used to investigate the plane strain behaviour of sand by Cornforth (1961), and clay by Wade (1963). A similar type of plane strain apparatus was developed by Wightman (1967). Dyson (1970) and Thornton (1974) used plane strain apparatuses, but with flexible side platens. Another type of plane strain apparatus called a true biaxial tester was developed by Harder and Schwedes (1985), in which stresses or strains in the x- and y- directions can be applied independently of each other to investigate the influence of the stress history on the yield limit.

Cornforth (1964) presented a series of results for drained plane strain compression (σ_3 = constant for some cases and σ_1 = constant for others) and drained triaxial tests (triaxial compression and triaxial extension) on Brasted sand. The triaxial compression and triaxial extension agree approximately to a common strength-density curve, and the plane strain compression with σ_3 = constant or with σ_1 = constant also agree approximately to a common strength-density curve. The drained strengths of Brasted sand in plane strain compression tests were compared with strengths measured in triaxial tests at the same initial density. The strength-density curves had the same general shape but the plane strain shear strengths were always higher, the differences in the peak angle of internal shearing resistance (φ_{max}) increasing progressively from about 0.5° for loose sand to more than 4° for the densest specimens tested. The angle of internal shearing resistance at large strains (φ_{cv}) measured in plane strain compression tests was constant (32.3°), irrespective of initial density, and had approximately the same value as those measured in triaxial compression tests (33°). It was concluded that the strain condition is a major factor contributing to the shear strength of sands. All the initial samples tested by Cornforth (1964) were anisotropically consolidated (K_0 consolidation) in order to maintain consistency in the plane strain and triaxial tests conditions (all specimens were consolidated with zero lateral strain). Cornforth (1964) indicated that K_0 consolidation and isotropic consolidation led to the same drained shear strength parameters in sands by quoting other research work, such as Bishop and Eldin (1953). Lee (1970) also used initial anisotropically consolidated samples and implied that this condition is more near to true field condition than isotropical consolidation condition. The results were similar to those reported by Cornforth (1964).

Bishop (1966) proposed the extended Tresca, as well as the extended von Mises failure criteria and examined different failure criteria (including the Mohr-Coulomb criterion) for a series of tests including plane strain, axisymmetric compression and axisymmetric extension tests. Bishop (1966) found that the Mohr-Coulomb criterion gave the best over-all data fit though for a comparison of the compression test and the plane strain test only the extended Tresca was in better agreement for dense sand. Bishop (1966) also proposed that for plane strain tests, $\sigma_2/(\sigma_1+\sigma_3) = 0.5\cos^2\varphi$, which will be examined in section 4.4.

Barden et al (1969) tested cuboidal samples of sand in plane strain at low and high pressures and showed that the critical state value of the mobilised friction angle φ_{cv} does not change significantly with pressure over the range σ_3 =137.9-5860.5 kPa for a sand with an initial porosity of 0.42. Barden et al (1969) implied that φ_{cv} was related to particle shape. Bishop (1966) pointed out that in triaxial tests high pressure caused the stress-strain behaviour of a dense sample to approach that of a loose one due to particle crushing, which was also shown to be true in plane strain by Barden et al (1969).

Thornton (1974) performed plane strain and axisymmetric compression tests on sand over a range of initial porosities. He concluded that all the previous experimental evidence showed that the stress-strain and volume change curves obtained from plane strain tests exhibited the same characteristic shape as those obtained from axisymmetric compression tests. There were, however, significant differences in the behaviour of granular materials when tested under plane strain and axisymmetric compression conditions. There was general agreement, from tests using a variety of apparatuses, that the effect of preventing any movement in one orthogonal direction was to increase the strength of the soil and to decrease both the volumetric and axial strains to failure. As a result, the use of a strength parameter determined from axisymmetric compression tests results will in most cases lead to a conservative design. On the other hand, it has been found that soils loaded in plane strain are highly susceptible to imperfections, leading to material instability or bifurcation, where sudden failure can occur much sooner than what is typically observed in the triaxial case (see e.g. Alshibli et al. 2003).

Han and Vardoulakis (1991) presented some results from an experimental study of the pre-failure and post-failure behaviour of water-saturated fine-grained sand in biaxial compression. The experiments were performed under undrained and drained conditions in a plane strain apparatus which allowed a detailed study of bifurcation and post-bifurcation phenomena. Emphasis was given to limiting states, deformation instabilities and failure phenomena (liquefaction and localization). Failure modes were illustrated by X-ray radiographs.

Finno et al (1997) presented experimental results which characterised the behaviour of a loose, fine-grained, water-saturated sand tested under globally undrained and drained conditions in a plane strain apparatus. The objective of the investigation was to provide insight into the phenomenon of shear banding in loose sand. Together with local measurements of boundary forces and deformations, stereophotogrammetry was used to investigate the progression of strain localization in plane strain compression. Typical results and findings concerning the evolution of non-homogeneous deformation were presented in detail. Shear banding occurred in both undrained and drained experiments on loose masonry sand. In general, temporary modes of strain localization, observed during macroscopically ‘uniform’ deformations of a specimen, gave way to a single, persistent shear band. A clear pattern of the onset of the formation of the persistent shear band, mobilization of the maximum effective friction and complete formation of the band was observed in all tests. The stress state when the localisation began was very close to, but preceded that corresponding to the maximum mobilized friction. The persistent shear bands evolved with changing width and orientation.

Matsushima et al (2002) presented a Laser-Aided Tomograph / Plane Strain Compression (LAT/PSC) testing method, which allowed for a discussion of granular micromechanics with visualised granular fabrics. The LAT technique was used to visualise in real time, any arbitrary cross-section of a granular specimen. An image processing algorithm was successfully developed to extract irregular perimeters of 3D grains, their fabric, and their motions (displacements and rotations) caused by loading.

Powrie et al (2005) performed a series of numerical plane strain simulations using the Itasca PFC-3D code. In these simulations, dense samples were comprised of about 10000 non-spherical particles, each formed by strongly bonding two spheres together. The simulations demonstrated the ability of DEM to capture the essential macro-features of soil behaviour as observed in laboratory tests, including the dependence of peak strengths on the initial void ratio relative to the critical void ratio. The development of strain localisation or shear bands associated with the use of rough loading platens, and the sensitivity of DEM to the initial sample porosity, particle shape factor and interparticle friction angle, were also investigated. It was found that the peak friction angle, maximum rate of dilation and the overall sample dilation during shear all increase as the shape factor [defined by (R+r)/R, where R and r are radii of the bonded spheres] increases. Particle rotations were shown to be a useful indicator of deformation mechanisms in that they indicated the extent of structural disturbance in the samples. In the literature, plane strain DEM simulations of dense systems can also be found in the work of Thornton (2000) and Ng (2004a, 2004b). However, plane strain DEM simulations of 3D very loose systems have never been reported before.

4.3 Simulation details

All the samples prepared by isotropic compression for axisymmetric compression test simulations reported in the previous chapter were used to investigate plane strain behaviour. Consequently, for a given porosity, the initial state is identical for both plane strain and axisymmetric compression simulations, see Table 3.1.

In order to perform plane strain simulations, the strain rate tensor was initially specified as follows: $\dot{\varepsilon}_{11} = 1.0 \times 10^{-5} s^{-1}$ (compressive), $\dot{\varepsilon}_{22} = 0$, $\dot{\varepsilon}_{33} = -1.0 \times 10^{-5} s^{-1}$ (tensile) and $\dot{\varepsilon}_{ij} = 0$ when $i \neq j$. A servo-control was used to keep the mean stress constant, see Appendix A. All the other simulation parameters used were the same as in Chapter 3.

4.4 Simulation results

The simulation results and discussions include the macroscopic and microscopic behaviour. The macroscopic behaviour includes the evolution of $(\sigma_1 - \sigma_3)$, $(\sigma_2 - \sigma_3)$, volumetric strain, porosity, $\sin\varphi$, $\sigma_2/(\sigma_1+\sigma_3)$, $0.5\cos^2\varphi$ and $(\sigma_2 - \sigma_3)/(\sigma_1 - \sigma_3)$; the microscopic behaviour includes the evolution of the deviator fabric and the mechanical coordination number.

4.4.1 Macroscopic behaviour

Figure 4.1 shows the evolution of the deviator stress ($q = \sigma_1 - \sigma_3$) plotted against deviator strain for all samples. Comparing Fig. 3.1a and Fig. 4.1, the general trends of the deviator stress evolution are very similar, and therefore, some general trends are only described briefly. A more detailed comparison (also for other parameters discussed) between axisymmetric compression and plane strain will be provided in chapter 7.

It can be seen from Fig. 4.1 that, as in axisymmetric compression, strain hardening followed by strain softening occurs for the two dense samples and no softening occurs for the loose samples. All the samples have approximately the same value of deviator stress at large strains. The peak value of deviator stress (for the dense samples only) and the critical state value (for all the samples) do not appear to depend on strain conditions (axisymmetric compression or plane strain) for the simulations reported. This implies that the appropriate shear strength criterion may be the extended Tresca criterion and it is interesting to note that Bishop (1966) stated, for a comparison of the axisymmetric compression and plane strain tests, only the extended Tresca criterion was better than the Mohr-Coulomb criterion for dense sand. The appropriate shear strength criterion will be further discussed in chapter 7.

Fig. 4.2 shows the evolution of ($\sigma_2 - \sigma_3$), which is qualitatively similar to the evolution of ($\sigma_1 - \sigma_3$) shown in Fig. 4.1.

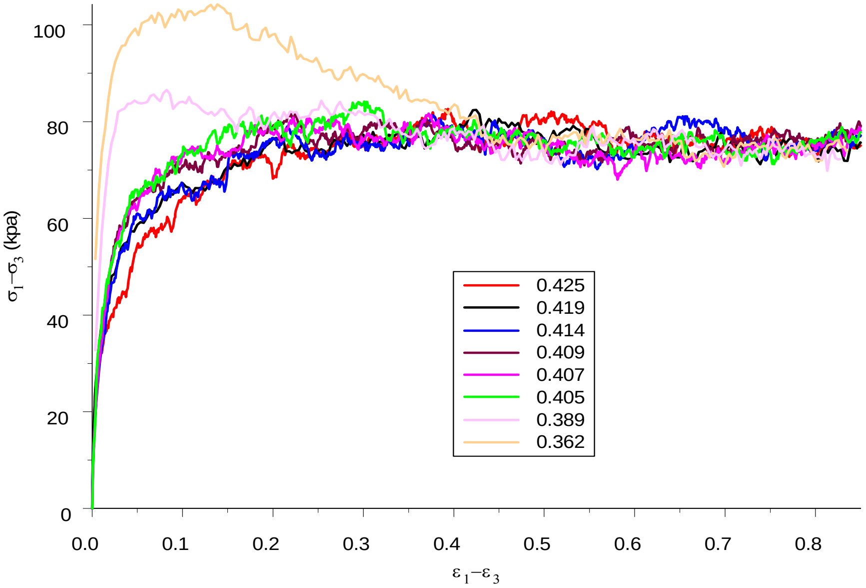

Fig. 4.1 Evolution of deviator stress (σ_1 - σ_3)

[key refers to porosity]

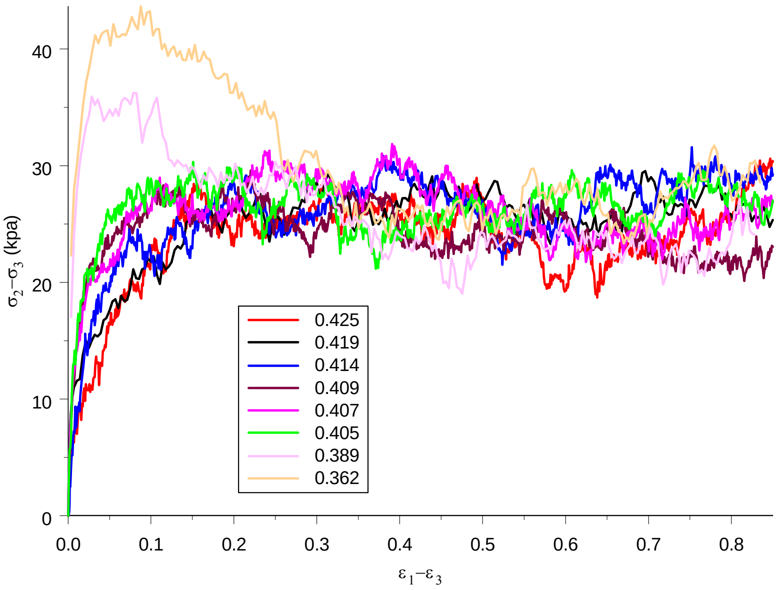

Fig. 4.2 Evolution of (σ_2 - σ_3)
[key refers to porosity]

Figure 4.3 shows the evolution of volumetric strain against deviator strain. Comparing Fig. 4.3 and Fig. 3.2, the evolutions of volumetric strain for axisymmetric compression and for plane strain simulations are similar. At large strains (critical state), volumetric strain remains approximately constant at different values for the different samples because of the different initial porosities.

Figure 4.4 shows the evolution of porosity plotted against deviator strain, in which it can be seen that the evolution for each sample is similar to that in drained axisymmetric compression simulations, and also the dilation and dilation rate discussed for each sample are qualitatively similar to those in drained axisymmetric compression. The porosities converge to a value of about 0.408 at large strains, which is slightly higher than the critical porosity (with a unique value of 0.407) obtained in drained axisymmetric compression simulations, see Fig. 3.3.

Figure 4.5 shows the evolution of sinφ plotted against deviator strain. Qualitatively the trend is similar to that obtained in axisymmetric compression. However, the magnitudes of $\sin\varphi_{max}$ for the two dense samples and the value of $\sin\varphi_{cv}$ for all samples are greater than the corresponding values obtained in the axisymmetric compression simulations. It can be seen from Fig. 4.5 that the peak value of sinφ for the densest sample is 0.5 ($\varphi_{max} = 30^\circ$) compared to the value of 0.44 ($\varphi_{max} = 26^\circ$) in axisymmetric compression. The peak value of sinφ for the medium dense sample is 0.42 ($\varphi_{max} = 24.8^\circ$) compared to 0.36

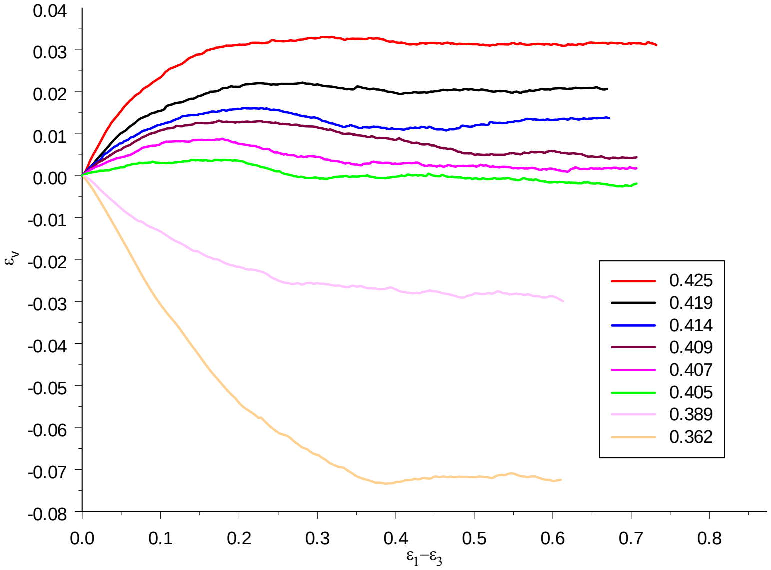

Fig. 4.3 Evolution of volumetric strain

[key refers to porosity]

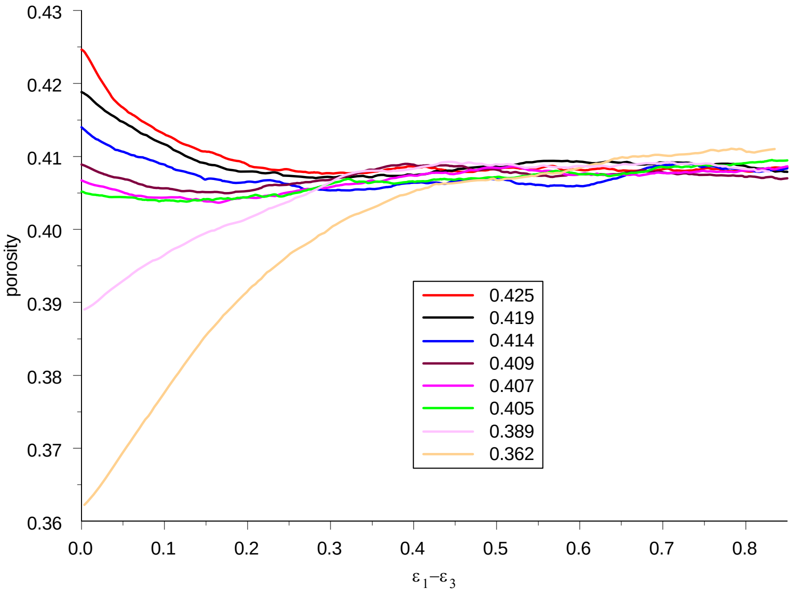

Fig. 4.4 Evolution of porosity
[key refers to porosity]

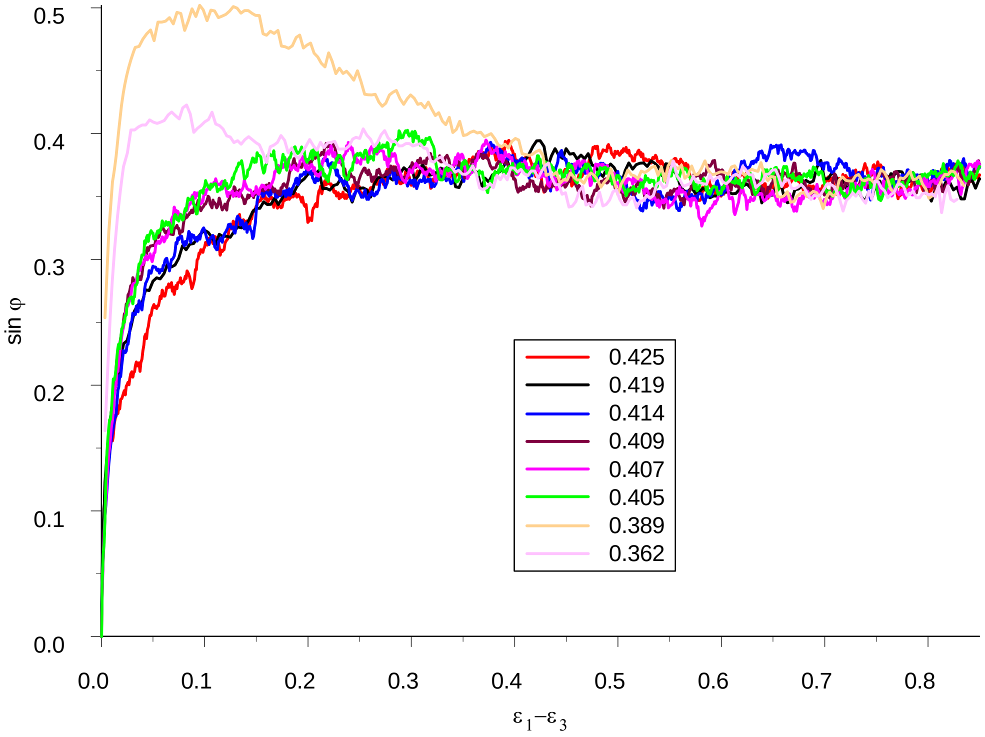

Fig. 4.5 Evolution of sinφ

[key refers to porosity]

(φ_{max} = 21°) in axisymmetric compression. The difference of the peak values of φ between the densest sample and the medium dense sample is 5.2° (the corresponding difference in axisymmetric compression is 5°, which does not seem to be dependent on the strain conditions. All the samples reach a unique sinφ at critical state with the value of 0.36 (φ_{cv} = 21°). The corresponding sinφ at critical state in axisymmetric compression was 0.33 (φ_{cv} = 19.3°). The critical state value (φ_{cv}) is independent of porosity under a given strain condition, but is dependent on the strain condition imposed.

If the peak values of φ for the loose samples is taken to be the critical state values under axisymmetric compression and plane strain respectively, it can be said that φ_{max} in plane strain is higher by 4° for the densest sample and by 1.7° for the loose samples. Cornforth (1964)'s results indicated this range was from 4° to 0.5°. With increasing initial porosity, the peak strength ($\sin\varphi_{max}$ or φ_{max}) for the dense samples will decrease but for all loose samples the strength is essentially the same.

Cornforth (1964) showed that the peak value of φ under plane strain was greater than that in axisymmetric compression, but the critical state values were not much different. The latter is not in agreement with the simulations reported in this thesis.

Figure 4.6a shows the evolution of $\sigma_2/(\sigma_1+\sigma_3)$ against deviator strain. For an isotropic elastic material tested under plane strain conditions, $\sigma_2/(\sigma_1+\sigma_3)$ defines the Poisson's ratio. However, as the particle systems are neither elastic nor isotropic, the ratio is not a measure of Poisson's ratio for granular media. At the start of the tests, the stress state is nearly isotropic and therefore $\sigma_2/(\sigma_1+\sigma_3)$ is almost equal to 0.5. Cornforth (1964) reported that the value of the intermediate principal stress in plane strain was less than one-half the sum of the other two principal stresses. Cornforth (1961, 1964) showed that $\sigma_2/(\sigma_1+\sigma_3)$ varied from 0.27 for the denser samples to 0.36 for the looser samples (at peak failure) and for each porosity the evolution of $\sigma_2/(\sigma_1+\sigma_3)$ could be taken as a constant. Fig. 4.6a indicates that all the values of $\sigma_2/(\sigma_1+\sigma_3)$ start from 0.5 and drop to 0.44 gradually. Comparing Fig. 4.6a and Cornforth's results, the DEM results give a higher

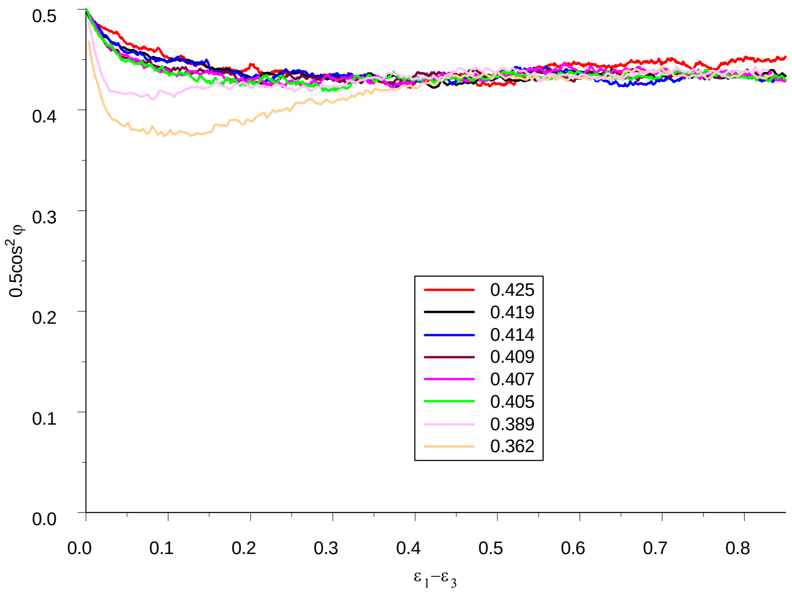

Fig. 4.6a Evolution of $\sigma_2/(\sigma_1+\sigma_3)$
[key refers to porosity]

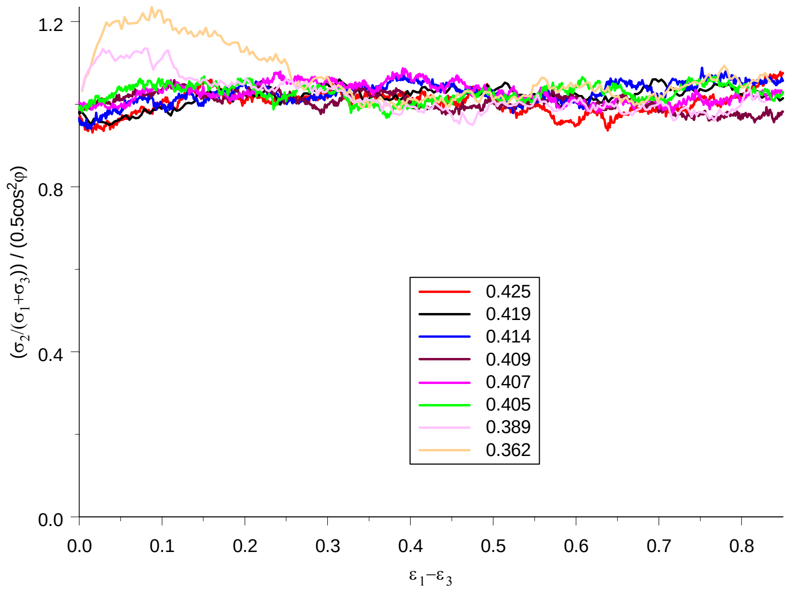

Fig. 4.6b Evolution of $[\sigma_2/(\sigma_1+\sigma_3)] / 0.5\cos^2\varphi$
[key refers to porosity]

value of $\sigma_2/(\sigma_1+\sigma_3)$ than that of the physical experiments. However, they cannot be directly compared since Cornforth used K_0 consolidation instead of isotropic consolidation, and, moreover, Green (1969) suggested that the intermediate principal stress as measured by Cornforth (1961) was low due to friction between the axial platens and the specimen. Fig. 4.6a indicates that after the initial drop, $\sigma_2/(\sigma_1+\sigma_3)$ can be taken as a constant value of 0.44, irrespective of the initial porosity. It seems that $\sigma_2/(\sigma_1+\sigma_3)$ is essentially independent of the initial porosity, which is in agreement with Reades (1972) and not with Cornforth (1964). Thornton (1974) found that the values of $\sigma_2/(\sigma_1+\sigma_3)$ at failure range between 0.3 and 0.4 and the value was independent of porosity and stress path. It should be mentioned that except for Thornton (1974) all the other above physical test data involved were for samples that were K_0 consolidated.

Bishop (1966) proposed that, for drained plane strain tests, $\sigma_2/(\sigma_1+\sigma_3) = 0.5\cos^2\varphi$, which indicates a higher value of $\sigma_2/(\sigma_1+\sigma_3)$ results for a lower value of $\sin\varphi$. Since the DEM simulations presented in this thesis employed spherical particles which give lower values of $\sin\varphi$ compared with those of real sand), the DEM simulations are expected to give higher values of $\sigma_2/(\sigma_1+\sigma_3)$ from Bishop's formula given above, which has been confirmed in the previous paragraph. The plot of $[\sigma_2/(\sigma_1+\sigma_3)]/(0.5\cos^2\varphi)$ is shown in Fig.4.6b, in which it is indicated that Bishop's formula $[\sigma_2/(\sigma_1+\sigma_3) = 0.5\cos^2\varphi]$ gives a reasonable approximation of $\sigma_2/(\sigma_1+\sigma_3)$ for all the loose samples at all strains and gives a good approximation for the dense samples only at large strains.

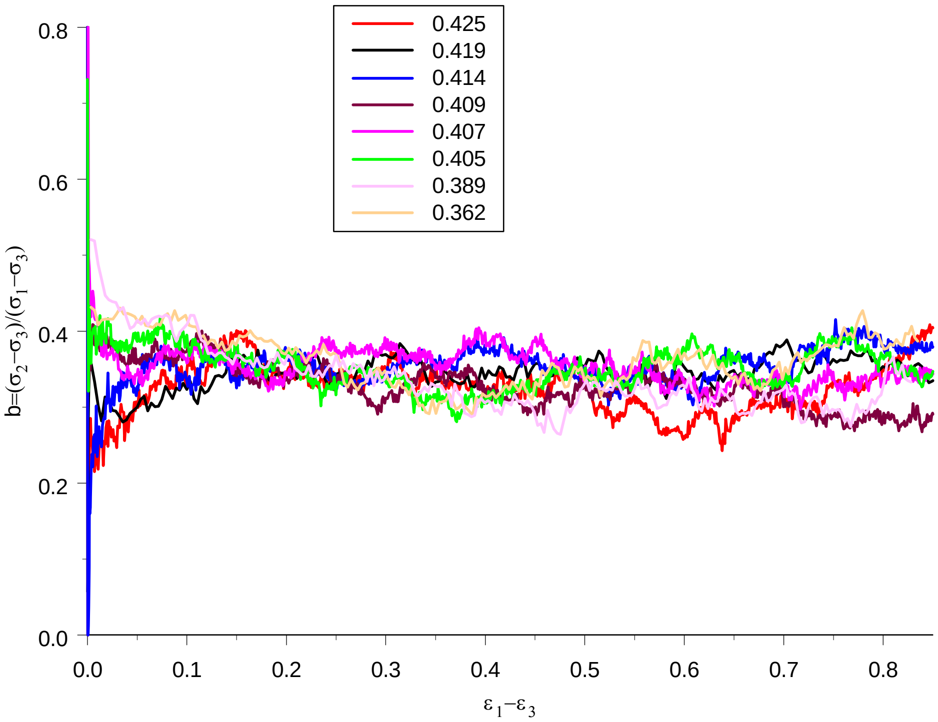

Fig. 4.7 Evolution of $(\sigma_2-\sigma_3)/(\sigma_1-\sigma_3)$
[key refers to porosity]

Bishop (1966) suggested that the influence of σ_2 can be more readily appreciated in terms of the nondimensional parameter

$$b = (\sigma_2-\sigma_3)/(\sigma_1-\sigma_3) \qquad (4.1)$$

Figure 4.7 shows the evolution of Bishop's b parameter stress b parameter plotted against deviator strain. At the start of shear, b is indeterminate (0/0) as the initial stress state is isotropic, resulting in big fluctuation at very small strains. Therefore the analysis of this parameter is not so significant at very small strains. From its definition, Bishop's b parameter is related to the Lode parameters by the following equations:

$$b = (1+\mu_\sigma)/2 \tag{4.2}$$

where μ_σ is the Lode parameter for stress (see Fung and Tong, 2001) and

$$\mu_\sigma = (2\sigma_2 - \sigma_1 - \sigma_3)/(\sigma_1 - \sigma_3) \tag{4.3}$$

and

$$\tan\theta_\sigma = \frac{1}{\sqrt{3}}\mu_\sigma = \frac{1}{\sqrt{3}}(2b-1) \tag{4.4}$$

where θ_σ is the stress Lode angle.

Figure 4.7 shows that b at critical state is about 0.34. Fig.4.1, Fig.4.2, Fig.4.3 and Fig.4.4 have confirmed that there is an approximate unique stress state at critical state.

4.4.2 Microscopic behaviour

Figure 4.8 shows deviator fabric plotted against deviator strain. Higher peak values and higher critical state values of the deviator fabric are observed in drained plane strain than in drained axisymmetric compression.

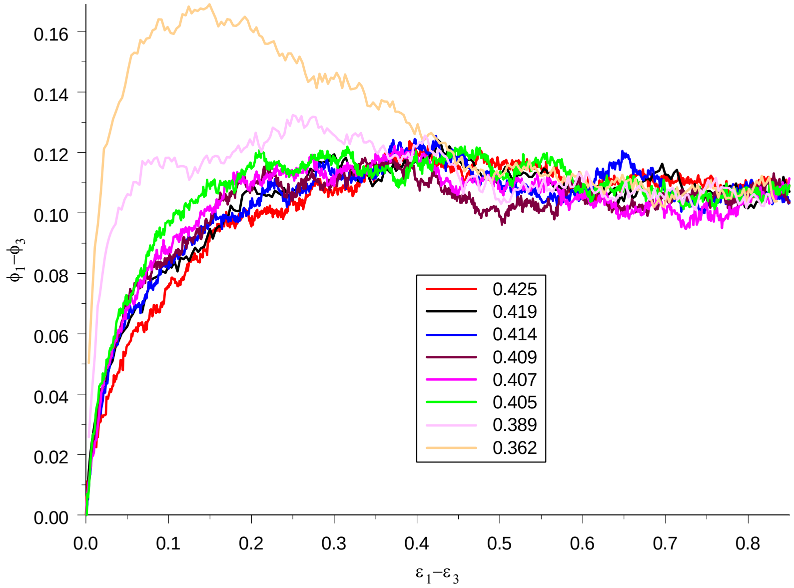

Fig. 4.8 Evolution of induced structural anisotropy
[key refers to porosity]

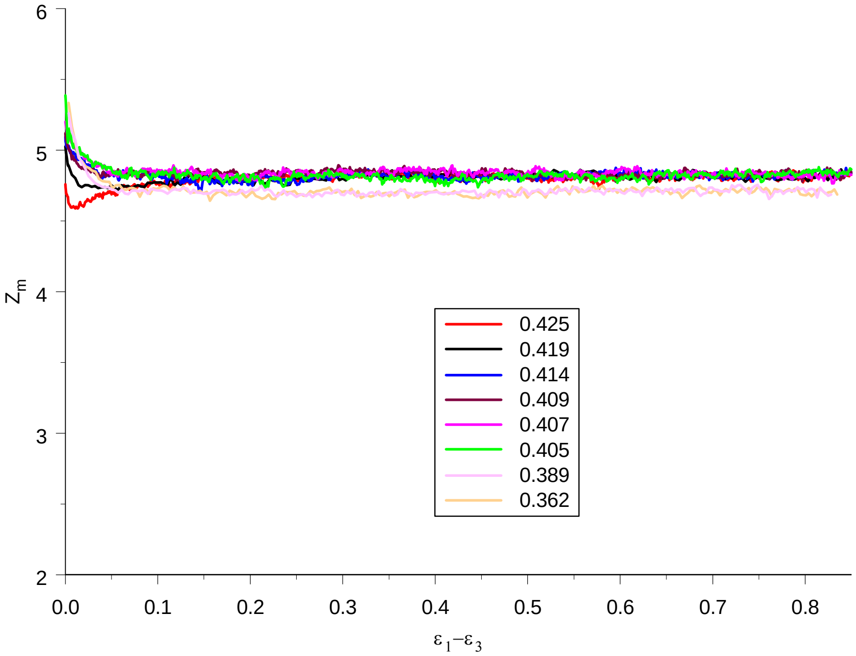

Fig.4.9 Evolution of mechanical coordination number
[key refers to porosity]

Figure 4.9 shows the mechanical coordination number plotted against deviator strain. The whole trend of the evolution for all the samples is very similar to that shown in Fig. 3.6a for axisymmetric compression simulations. Accordingly it can be concluded that there is a critical Z_m for the dense samples (4.7) and the loose samples (4.85) respectively and the evolution of Z_m is independent of strain conditions.

4.5 Summary

An approximate critical porosity (0.408) was observed in these DEM simulations for constant mean stress drained plane strain conditions and is a little higher that (0.407) for axisymmetric compression drained conditions. The critical porosity can be approximately taken as a constant for a given mean stress, which is independent of the initial porosities and strain conditions. It is observed that there is an approximate unique critical state in drained plane strain conditions in $(\sigma_1,\sigma_2,\sigma_3,e)$ space, which is independent of the initial porosities. Oda et al (1997) questioned the existence of critical density for dense sands from the results of drained plane strain tests because of shear banding (see also Mooney et al 1998). Their result is based on the void ratio measured in the shear band, not the same as the void ratio for the whole sample.

The DEM simulations presented showed a lower peak and critical value of $\sin\varphi$ than real sand, which can be explained by the effect of particle shape. This leads to a higher values of $\sigma_2/(\sigma_1+\sigma_3)$ for the DEM simulations in this chapter compared with those in Bishop (1966).

It is also observed that there is a unique value of mechanical coordination number at critical state for the dense and loose samples respectively and the values are independent of strain conditions. The trend of the evolution of deviator fabric is similar to that of deviator stress, which is also true in axisymmetric compression, as reported in chapter 3.

CHAPTER 5: ‘UNDRAINED’ AXISYMMETRIC COMPRESSION SIMULATIONS

5.1 Introduction

In cases where rapid loading occurs, even cohensionless soils may not have time to drain during the loading process and the undrained shear strength must be determined. Conventional strength determinations are only made for monotonic loading, not cyclic loading although the stress-strain application under loading especially during earthquakes will be cyclic in nature (Seed and Lee 1967). In a standard laboratory undrained experiment, an axisymmetric compression test is performed under constant cell pressure conditions, which means that the minor total principal stress σ_3 ($\sigma_2 = \sigma_3$) is maintained at a constant value and failure results from the increase in the major principal stress σ_1. The starting point before the undrained shearing can be at an isotropic or anisotropic stress state, which is usually obtained in laboratories after an isotropic consolidation or anisotropic consolidation respectively. The isotropically consolidated undrained triaxial test is more frequently performed in laboratories, which is often called CU or CIU tests. If there is no consolidation process, the corresponding unconsolidated undrained test is often called a UU test. For saturated soil samples, undrained also means constant volume (more strictly constant mass, see Muir Wood 1990), while for unsaturated soil samples this is not true. The different types of soil laboratory tests and the procedures are well documented in Bishop and Henkel (1957) and Head (1986). Interest in undrained conditions especially for loose sand has become widespread since the work of Bishop (1966, 1971) and Castro (1969).

In section 5.2, a literature review of undrained tests is presented covering both physical experiments and DEM. In section 5.3, simulation details for undrained shearing are provided. In section 5.4, undrained simulation results of loose systems at the same initial isotropic stress state are presented and fundamental features in undrained tests at low confining pressure on sand are effectively captured. The initiation of instability is also examined. In section 5.5, undrained simulation results for a very loose system (porosity = 0.419) with preshearing history are presented in order to mimic the experimental work reported by Finge et al (2003) and to explore more information on preshear effects. A low strain rate undrained test is presented in section 5.6. A summary is provided in section 5.7.

5.2 Literature review

Bishop and Eldin (1950, 1953) presented results of a series of undrained triaxial compression tests on saturated sand, and concluded that:

1) In undrained tests, the pore water pressure may decrease but it will not drop below a value of about -1 atm; on reaching this pressure the pore water will cavitate and small bubbles of water vapour and air will form in the soil voids. When cavitation occurs in the pore water, the failure envelope in terms of total stresses will have a slope equal to the angle of friction of the sand. (Seed and Lee 1967).
2) For undrained tests in which cavitation does not occur, the failure envelope in terms of total stresses should be horizontal, and will have the shear characteristics of a

purely cohesive material with reference to total stresses, although the sand tested has no true cohesion in terms of effective stresses.

Bishop and Eldin (1950) gave an explanation for this behaviour based on three examined basic principles:

1) The mechanical properties, and hence the strength of a soil, are controlled solely by the intergranular forces, i.e. effective stresses.
2) The effective area of contact between the soil grains is negligible. The pore water pressure therefore acts equally all round the soil grains, and changes in it do not affect the intergranular forces.
3) Since water is incompressible compared with the soil structure, a change in applied pressure is carried wholly by the pore water, and the stresses in the soil structure are not changed unless drainage conditions permit a volume change.

After Bishop and Eldin (1950), Newland and Allely (1959) performed a set of undrained tests in order to study the factors influencing the magnitude of the “cohesion”. Newland and Allely (1959) reached a conclusion for dilatant soils that in an “ideal” undrained test where no skeleton volume expansion occurs, the value of the “cohesion” is determined by the initial porosity with other things being equal. Newland and Allely (1959) also showed that significant volume expansion of a dilatant sample may occur during an undrained test in which cavitation does not occur, and this expansion is balanced by penetration of the rubber membrane into the sample due to the increasing cell pressure. They developed a method of analysis to relate the results to those obtained in drained tests on the same materials. Attempts to predict the undrained behaviour from drained tests were later made by Seed and Lee (1967), De Groot and Stoutjesdijk (1997), Norris et al (1997) and Ashour and Norris (1999).

Poulos (1981) defined and explained the concept of steady state deformation for any mass of particles, which is that state in which the mass is continuously deforming at constant volume, constant normal effective stress, constant shear stress, and constant velocity. The steady state of deformation is achieved only after all particle orientation has reached a statistically steady-state condition and after all particle breakage, if any, is complete, so that the shear stress needed to continue deformation and the velocity of deformation remain constant. It has been pointed out that the critical state and steady state differ in that the steady state has an ‘associated flow structure’ and a requirement for a constant velocity, neither of which are incorporated in critical state concepts defined by Roscoe et al. (1958). Been et al. (1991) pointed out that constant velocities actually occur in load-controlled liquefaction tests and showed the steady state and critical state were the same. The steady state and critical state were considered to be equivalent also by Yang (2002).

Been and Jefferies (1985) defined a state parameter ψ, which is the difference between the void ratio in an initial state (e_i)and the void ratio of the steady state (e_{ss}) for the same initial effective mean stress. It was implied that similar behaviour should be expected for similar ψ values, independent of the initial effective confining stress. Been et al. (1991) examined a fine to medium, uniformly graded quartzitic sand. The critical and steady states were shown to be equal and independent of stress path, sample preparation method, initial density and drainage conditions. The critical/steady state line was shown to be nonlinear (curved), and to have a marked increase in slope at stress levels greater than 1 MPa. The critical state friction angle in sands was found to decrease with increasing void ratio, while the critical/steady line was assumed to be straight by Been and Jefferies (1985). A unique steady state line (in e-p-q space) was proposed by Been et al (1991), which is independent of initial confining pressure, the stress paths, the loading modes, the consolidation history, the strain rate and the initial fabric. Such a unique steady state line was also shown by Ishihara (1993).

Vaid et al. (1990) investigated the effect of stress path on the steady state (SS) line of very loose sand. Quasi-steady state (which will be explained in section 5.4), which corresponds to phase transformation (PT) state defined by Ishihara et al. (1975), is also incorporated in the SS frame work. It was found that, for a given void ratio, steady state deviator stress (q) is smaller in undrained extension than in compression, and the difference increased as the sand becomes looser. However, the friction angles mobilized at steady state in undrained extension and in compression are essentially the same.

Yamamuro and Lade (1997) presented undrained triaxial tests on very loose Nevada sands with fines and complete static liquefaction (zero effective principal stresses) at low confining pressures was observed. As confining pressure was increased, the effective stress path indicated increasing resistance to liquefaction by showing increasing dilatant tendencies. It was observed that increasing confining pressures also increases stability for the same density. The locus of the top points of different effective stress paths from a series of undrained triaxial compression tests of varying initial confining pressures with the same initial density fall onto a unique line, called the instability line based on Lade (1992). The unique instability line was also observed in Lee (1965) and Konrad (1993). Yamamuro and Lade (1997)’s results are opposite to that of normal soil, where increasing confining pressure results in decreasing dilatant tendencies (see Lee 1965 and Seed and Lee 1967). The presence of fines in the Nevada sand was thought to cause this reverse behaviour. It was hypothesized that the fines and larger particles create a particulate with unusually high compressibility at low confining pressures.

Doanh et al (1997) presented a series of undrained tests in both triaxial compression and extension for very loose Hostun sands consolidated isotropically and consolidated anisotropically along constant effective stress ratio paths. Static liquefaction and instability concepts were considered in these tests. It was pointed out that the instability concept of Lade is strongly influenced by the monotonic consolidation history and, a larger positive anisotropic consolidation always produces a steeper slope of instability on a q – p plot in compression but a reverse trend may occur in extension. Doanh and Ibraim (2000) showed that the minimum undrained strength of Hostun RF sand at steady state under triaxial compression and extension is strongly influenced by the normalized mean effective stress at peak, and by the void ratio at the end of the initial monotonic consolidation stage.

Bopp and Lade (2005) investigated the undrained behaviour of sand at high pressures and studied the effects of initial relative density on the stress-strain, pore pressure and strength behaviour on loose and medium Cambia sand. Undrained behaviour of dense Cambia sand at high pressures was investigated by Lade and Yamamuro (1996). The stress-strain, pore pressure and strength behaviour were found to be very similar and almost independent of initial relative density at high pressures, because the isotropic compression curves tend to merge once particle breakage becomes important at high pressures. Rutledge (1947) hypothesised that isotropic compression and strength lines are parallel on a semi-log plot of void ratio and stress magnitude, which was considered applicable only to normally consolidated clays. Interpretation of all results from high pressure testing on Cambia sand (all densities) studied in terms of total stresses showed that the sand behaved as a normally consolidated clay in agreement with Rutledge (1947). However, at low pressures, this is not true as isotropic compression and strength lines cross each other for sands, as also implied by Been et al. (1991).

Instead of undrained tests, Chu et al. (1992) and Chu and Leong (2001) performed constant strain increment ratio ($d\varepsilon_v/d\varepsilon_1$ = constant) test for isotropically consolidated sand. It was proposed that strain softening occurs when the following condition meets:

$$(\frac{d\varepsilon_v}{d\varepsilon_1})_i - (\frac{d\varepsilon_v}{d\varepsilon_1})_s \leq 0 \tag{5.1}$$

where $(d\varepsilon_v/d\varepsilon_1)_i$ is the imposed strain increment ratio and $(d\varepsilon_v/d\varepsilon_1)_s$ is the maximum strain increment ratio obtained in a drained test conducted under the same initial effective confining stress. The undrained test is thus a special case in which $(d\varepsilon_v/d\varepsilon_1)_i$ is equal to zero, which can explain why strain softening occurs only for loose sand not for dense sand in an undrained test. It can also be deduced from (5.1) that for dense sand with negative values of $(d\varepsilon_v/d\varepsilon_1)_s$, strain softening will still occur so long as $(d\varepsilon_v/d\varepsilon_1)_i$ is more negative, as observed in their experiments. Consequently, liquefaction (even static liquefaction) and instability can be observed even for very dense sand, see also Lancelot et al. (2004).

In DEM simulations, constant volume tests are often performed to simulate undrained behaviour without dealing with pore pressure. However, constant volume only exists for undrained saturated samples (not for unsaturated), and this means the constant volume DEM simulation results should be relevant only to saturated undrained tests in laboratories. Such a method has been used by Thornton and Barnes (1986), Kishino (1990), Ng and Dobry (1994), and Sitharam et al (2002). Hakuno and Tarumi (1988) was the first to propose a technique to numerically couple fluid flow with the DEM considering individual pores. The volume change of each pore was used to calculate pore pressure generation by assigning elastic properties to the fluid (So no flow is assumed). Hakuno and Tarumi (1988)’s method was improved by Nakase (1999). Bonilla (2004) pointed out that the validity of using constant volume simulations as representative of undrained tests could be questioned. However, Bonilla (2004) made a comparison between DEM constant volume simulation without pore pressure and a DEM undrained simulation with fluid coupling, both for 2D assemblies of elliptical particles. The stress-strain behaviours were found to be very similar.

5.3 Simulation details

There are very few published results of DEM simulations of ‘undrained’ tests (see Chapter 2). Almost all DEM simulations are performed ‘in a vacuum’ without fluid. However, in principle, it is necessary to model the fluid phase and how the fluid/particle phases interact with each other, e.g. as in DEM simulations of fluidised beds (Tsuji et al 1993 and Kafui et al 2002) in order to obtain complete information. In the DEM simulations reported in this thesis the fluid phase is ignored and all stresses are calculated from the orientational distributions of forces at the contacts between particles. Consequently, the effective stresses are calculated directly. This is in contrast to laboratory experiments in which the total stresses and the pore water pressure are measured and the effective stresses are obtained indirectly from Terzaghi’s effective stress equation. According to Terzaghi’s effective stress concept different total stress paths lead to the same unique effective stress path, for the same initial specimen conditions. Therefore, in DEM simulations the pore water pressure can be obtained, for any desired total stress path, from the horizontal distance between the total stress path and the effective stress path on a q – p’ plot. Such a method for calculating pore water pressure was used in DEM simulations by Dobry and Ng (1992).

All ‘undrained’ simulations in this chapter were carried out in a periodic cell, thereby eliminating any boundary effects. In order to mimic undrained tests, constant volume tests were simulated in which the initial strain-rates in the three principal stress directions were set to $1.0 \times 10^{-4} s^{-1}$, $-5.0 \times 10^{-5} s^{-1}$ and $-5.0 \times 10^{-5} s^{-1}$ respectively, an order of magnitude ten times of those in the corresponding drained tests, see chapter 3. Under this strain-controlled condition (instead of servo-control of stress), $\sigma_2 = \sigma_3$ is approximately satisfied throughout the simulations. All the simulations start from an initial almost isotropic state with $\sigma_1 = \sigma_2 = \sigma_3 =$ 100 kPa. All the other simulation parameters (the initial strain rates and control mode excluded) are the same as before. One constant volume simulation result at low strain rates is also provided and discussed at the end of this chapter.

5.4 Simulation results (for loose samples) without preloading

In Chapter 3, the results of ‘drained’ axisymmetric compression simulations were reported for constant mean stress conditions. Constant volume tests were simulated on the same six loose systems. It was shown under ‘drained’ axisymmetric compression simulations volumetric contraction occurred (Fig. 3.2) for the six loose systems. In the loose systems, samples with porosities of 0.405, 0.407 and 0.409 exhibited very low contraction compared with samples with porosities of 0.414, 0.419 and 0.425. Thus the first set is called medium loose and the latter set is called very loose.

The macroscopic behaviour includes the undrained stress path and the evolutions of deviator stress, mean stress and sinφ. The ‘microscopic’ behaviour includes the evolutions of mechanical coordination number and deviator fabric.

5.4.1 Macroscopic behaviour

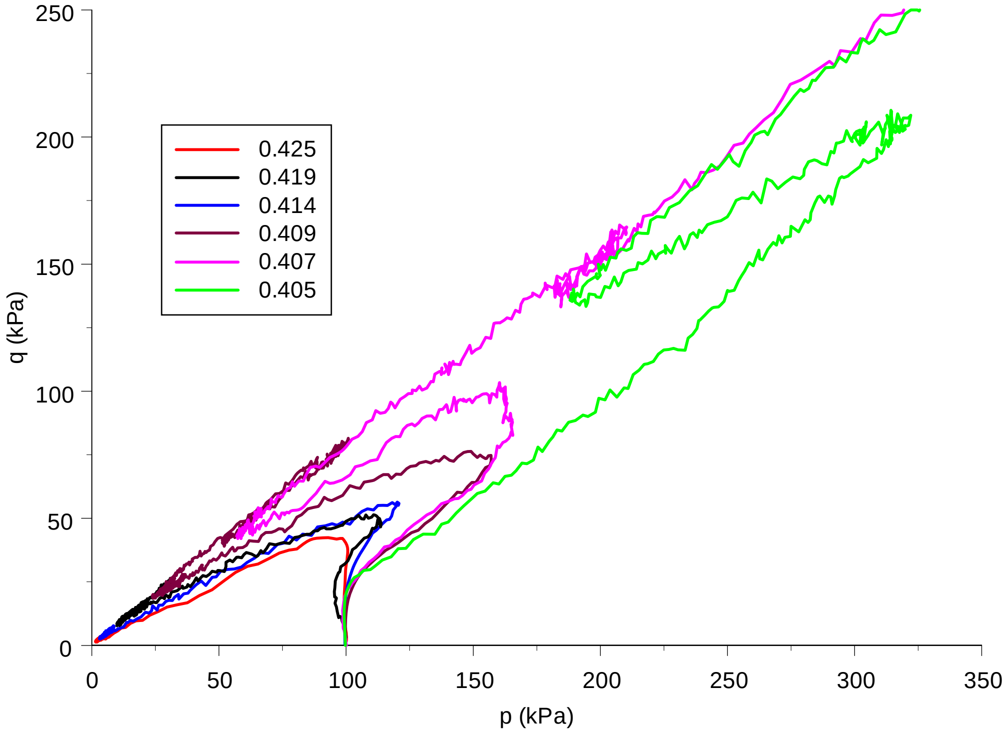

Fig. 5.1 Constant volume stress paths

[key refers to porosity]

Figure 5.1 shows the constant volume stress path (CVSP) for all six loose samples. The initial state on CVSP is the isotropic point (p = 100 kPa, q = 0). It can be seen that for all the loose samples, the deviator stress increases to a peak, followed by a decrease to a minimum value, maybe followed by an increase again. For all the loose samples except the loosest sample with porosity 0.425, p increases before the initial peak of q or p is obtained. According to Been et al. (1991), see also discussion on evolution of p, the loose samples can be said to exhibit a tendency to dilate before the initial peak of q (except the loosest sample with a porosity of 0.425), followed by a tendency to contract until a minimum value of q is obtained, followed by a tendency to dilate again. For the loosest sample (0.425), the stress state after the minimum value of q is obtained is constant with further strain (this will be more clearly seen in Fig. 5.2). Such a state is called steady state (SS) by Poulos (1981). The very loose samples (0.414, 0.419, 0.425) all exhibit steady state (the change of stress for samples 0.414 and 0.419 after the minimum value of q is obtained can be ignored from a practical viewpoint, see Fig. 5.2). The medium loose samples also exhibit a 'steady' state (with no change of stress with further strain, see Fig. 5.2, but after this state q increases. Such a 'steady' state is called quasi-steady state (QSS) by Alarcon-Guzman et al. (1988), or phase transformation (PT) state by Ishihara et al. (1975) because it defines a transient state from contractive to dilative behaviour. Corresponding to steady state, liquefaction is said to occur for the three very loose samples. Corresponding to quasi-steady state, limited (partial, temporary) liquefaction is said to occur for the three medium loose samples. There has been some argument about whether quasi-steady state is a real material behaviour. Been et al. (1991) suggested that quasi-steady state is the result of non-uniformities and other testing effects. Zhang and Garga (1997) indicated quasi-steady state is a test-induced behaviour, not because of non-uniformities but mainly due to end restraint and possibly due to the variation of membrane penetration and the compression of pore fluid. Chu (1992) suggested quasi-steady state can be a real material property.

Been et al. (1991) showed a unique ultimate state line in q-p space in undrained tests and also called it the critical state line. Chu (1992) stated that for loose sand, the critical state is the failure state measured in a drained state and the steady (or quasi-steady) state is the ultimate state in an undrained test; the equivalence of the critical state and steady state reflects the fact that the failure stress ratio measured from a drained test is the same as the ultimate stress ratio measured from an undrained test for loose sand. Obviously, for quasi-steady state, q is not constant for a given sample at the ultimate state. However, Been et al. (1991) considered the ultimate state line to be the same as the critical state line and considered QSS as non-real material behaviour. It appears that in Fig. 5.1, the ultimate states form a straight line passing through the origin, which means the slope $M = q/p$ of the ultimate state line is constant. The relationship between M and $\sin \varphi_{us}$ (the mobilized friction angle at the ultimate state) for undrained axisymmetric compression is: $M = 6\sin\varphi_{us}/(3-\sin\varphi_{us})$. Fig. 5.1 seems to imply that M is independent of porosity. In these undrained axisymmetric tests for the loose samples M is about 0.79, which is a little higher than the value of 0.74 obtained in drained constant mean stress axisymmetric simulations at critical state. The typical value of φ_{us} has been given by many researchers, 30^o by Castro (1969) as well as by Sladen and Oswell (1985), 34^o by Bishop (1971), 31^o by Ishihara (1993) and 27^o by Bonilla (2004). The value of M is accordingly around 1.2. The DEM simulations in Fig. 5.1 show a smaller M ($M = 0.79$, corresponding φ_{us} is 21^o) than real sand because of the influence of particle shape as discussed in Chapter 2. The value of M is taken to be independent of void ratio and cell pressure by the above researchers mentioned.

Figure 5.2 shows the deviator stress plotted against deviator strain for all the systems. In the simulations, σ_2 is approximately equal to σ_3 and $\varepsilon_2 = \varepsilon_3$, and the definition of deviator stress/strain is the same as in drained axisymmetric compression. It can be seen that for the very loose samples, the initial peak in q occurs at very small strains. At very small deviator strains (smaller than 0.004), the stress-strain behaviours for all loose samples are almost identical and can be said to be independent of porosity. After the strain corresponding to the initial peak in q for the loosest sample, the stress-strain behaviours are different and dependent on porosity. From the six loose samples, it can be concluded that the initial peak value of q is dependent on the porosity and, the looser a sample is the smaller the strain required to reach peak q and the smaller the peak value of q (the deviation between porosities 0.419 and 0.414 is ignored here). After the peak, q drops quickly to a minimum value, which corresponds to the SS or QSS state. The concept of liquefaction was defined by Castro (1969) as a sudden loss of effective stress in undrained conditions due to the large increase of pore pressure, which is similar to the behaviour of these constant volume simulations of loose samples. It can be seen that the minimum values of q at SS for the very loose samples are not zero (it is about 2kPa for porosity 0.425). Yamamuro and Lade (1997) defined static liquefaction as a special case in steady state in which zero effective confining pressure and zero deviator stress. Such static liquefaction is not observed for the very loose samples in the DEM simulations. Thus static liquefaction as defined by Yamamuro and Lade (1997) does not occur in the simulations.

It can be said that the three very loose samples exhibit liquefaction and the three medium loose samples exhibit limited liquefaction, which corresponds to SS and QSS respectively.

Also it can be seen from the three medium loose samples which exhibit QSS behaviour, that as porosity decreases, the corresponding strain range (the difference between strain when QSS starts and when QSS ends) for the whole QSS process becomes smaller. As the specified strain rates are the same for all the undrained axisymmetric compression tests, it can be said that as porosity decreases, the time required for the whole QSS process is smaller. It can be seen that as porosity decreases, a larger strain for SS (QSS) to begin is observed or it can be said that decreasing porosity increases the resistance to

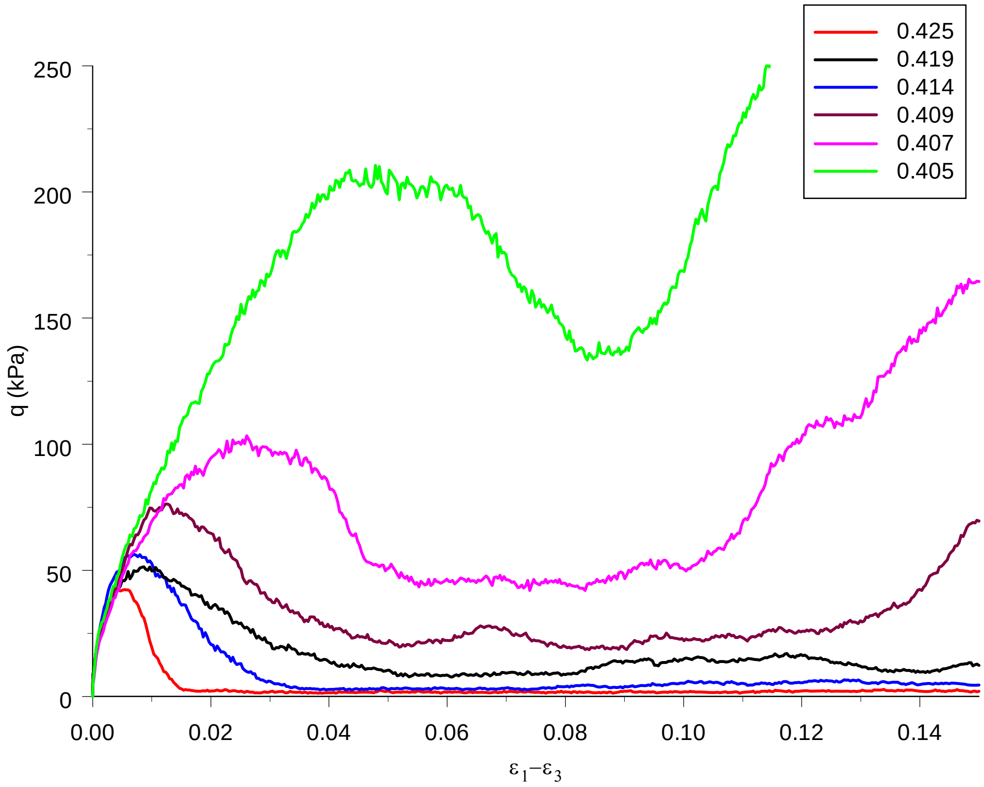

Fig. 5.2 Evolution of deviator stress

[key refers to porosity]

liquefaction. If the SS and QSS are considered in the same framework, it can be concluded that the shear strength (q) at SS and QSS is dependent on porosity, decreasing with increasing porosity.

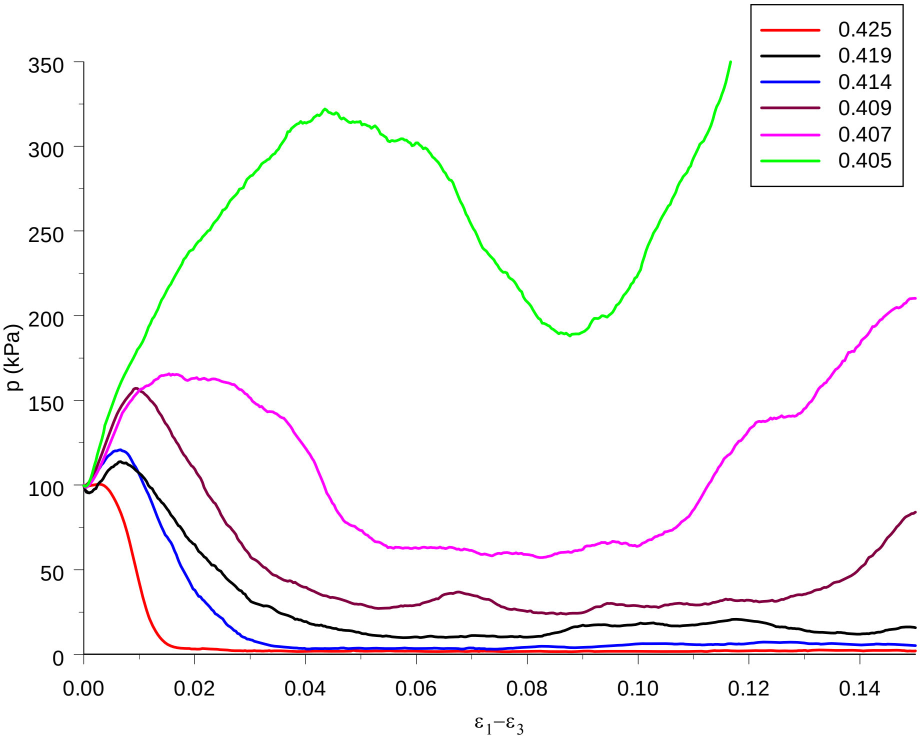

Fig. 5.3 Evolution of mean stress

[key refers to porosity]

Figure 5.3 shows the mean stress plotted against deviator strain for all the systems. The simulations show that both q and p become constant at SS (QSS) simultaneously (see Figs. 5.2 and 5.3). The change of p is indirectly related to change of pore pressure (see section 5.3) if a constant σ_3 total stress path is assumed, which is what occurs in conventional undrained triaxial tests. On a q-p plot (effective stress), the total stress path of constant σ_3 (TSP) has a slope of 3, the effective stress path (ESP) is as shown in Fig. 5.1. When p (all the stresses are effective ones except when stated otherwise) decreases in the undrained axisymmetric compression simulation tests, pore pressure will increase. When p increases, pore pressure will generally decrease. According to Been et al. (1991), dilation and contraction are used in a loose manner to describe negative and positive rates of pore pressure change. Therefore, p increasing means tendency for dilation occurs, p decreasing means tendency for contraction occurs. Except for the loosest sample, all the loose samples exhibit initial tendency of dilation until a peak of p (or q) is obtained. All the loose samples exhibit a tendency for contraction (the tendency for contraction rates are very high) after the peak value of q until SS (for very loose samples) or QSS (for medium loose samples) are reached. The very loose samples (especially porosities 0.414 and 0.419) exhibit small changes of p at large strains, but such change of p is very small and can be so ignored compared with the medium loose samples. It can be seen that the rate of the tendency for dilation after QSS for the medium loose samples increases as porosity decreases.

Figure 5.4 shows sin φ plotted against deviator strain for all the loose systems. From the definition of sinφ, $\sin\varphi = (\sigma_1-\sigma_3)/(\sigma_1+\sigma_3)$, for axisymmetric compression, we have $q/p = 6\sin\varphi/(3-\sin\varphi)$, which shows the evolution of sin φ is not an independent set of plot with Figs. 5.1, 5.2 and 5.3. It can be seen that the evolution of sinφ is almost identical at the very small strains. For the loosest sample (0.425), strong fluctuation occurs at a deviator strain of 0.015 which approximately corresponds to the deviator strain when minimum q occurs (near SS). For the other very loose samples (0.419, 0.414), fluctuations occur at a greater deviator strain and the amplitude is smaller compared with that of the loosest sample. Relatively stable fluctuations for the three very loose samples are observed after a deviator strain of 0.06. For the medium loose samples (0.409, 0.407, 0.405), the fluctuations can be ignored compared with those exhibited by the very loose systems. The fluctuations at SS for the very loose samples indicate that the stresses (q and p) are not constant at SS. Since at steady state, the values of q and p are all small, the difference between q/p and (q+δq)/(p+δp) may be large, where δ means a change of stress caused by a small loading strain. This is why the fluctuations occur. For the medium loose samples, the values of q and p are relatively large and the difference between q/p and (q+δq)/(p+δp) is small. This is why a smoother (almost no fluctuations) curve is observed for each of the medium loose samples. It can be seen that at SS there is not a unique value of $\sin\varphi_{ss}$, and the average value of $\sin\varphi_{ss}$ increases as porosity increases. Been et al (1991) pointed out that the data points near the origin on q-p space appear to be close to the critical state (as they called it), but in fact they were not. Their observation is that $\sin\varphi_{ss}$ decreases with increasing porosity. However, their observation of this was mainly based on high confining pressure. While for medium loose samples, a unique value (about 0.35) of $\sin\varphi_{us}$ at ultimate state is observed from Fig. 5.4, which corresponds to the ultimate state described previously with M = 0.79. From the three medium loose samples (compare Fig. 5.2 and Fig. 5.4), it can be seen that $\sin\varphi_{QSS}$ at QSS is smaller than $\sin\varphi_{us}$. This implies that QSS on p-q space is not on the ultimate state line, which cannot be seen very clearly in Fig. 5.1. However, from a practical viewpoint, $\sin\varphi_{QSS}$ and $\sin\varphi_{us}$ for the medium loose samples can be taken as identical as the difference is small. In q-p space, a unique straight line at ultimate state can be assumed. To be conservative, this straight line should be based on the data points obtained from the medium loose samples with higher ultimate values of stress and not based on the data points at very low ultimate values of stress.

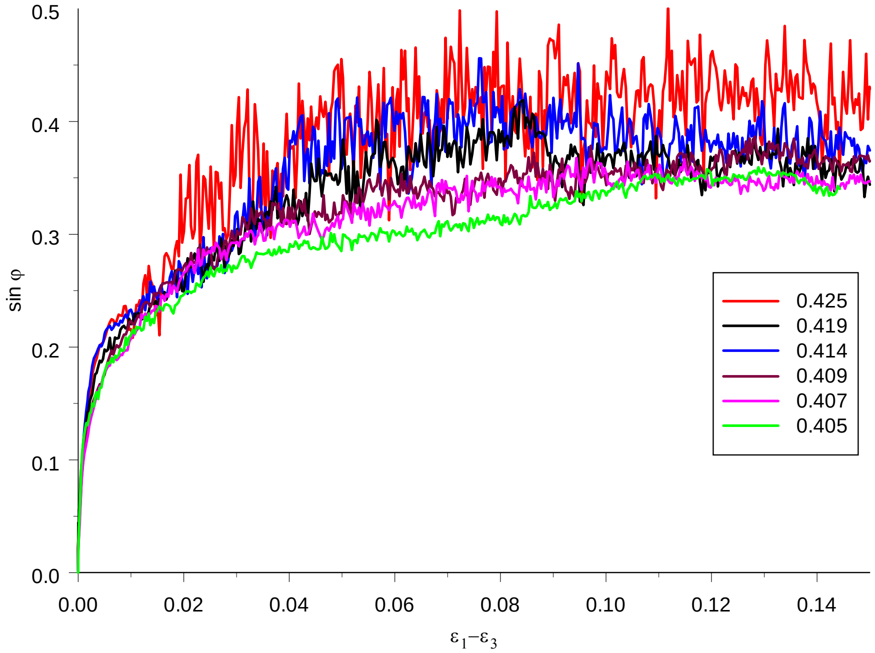

Fig. 5.4 Evolution of sinφ

[key refers to porosity]

5.4.2 Microscopic behaviour

Figure 5.5 shows the mechanical coordination number (Z_m) plotted against deviator strain for all the loose systems. It is found that the mechanical coordination number decreases initially for all the loose systems until a minimum value is reached. The initial drop in the mechanical coordination number is due to loss of contacts in the extensional principal strain directions, Cundall et al (1982). The minimum value of Z_m occurs at a strain coincident with the SS or QSS for each loose system see Fig. 5.5 and Fig. 5.2. Similar to the discussion related to Fig. 5.2, a steady state mechanical coordination number can be defined for the very loose systems, which remains almost constant; a quasi-steady state mechanical coordination number can be defined for the other loose systems. It is observed that the steady (or quasi-steady) state mechanical coordination number depends on the porosity, decreasing with increasing porosity (the deviation between porosity 0.414 and porosity 0.419 is ignored considering the trend for all ranges of porosities), the result of which is the same as the shear strength (q) at SS (or QSS).

The mechanical coordination number is related to the structural stability of the system. This can be considered as follows:

Consider a 3D assembly with $\mu \to \infty$, i.e. no sliding anywhere. The number of degrees of freedom of a single particle is 6 (three rotations and three translations), so the total number of degrees of freedom in the system is 6N, where N is the number of particles. The number of constraints (unknown forces) at a contact is 3 (no couple is considered at a contact in this thesis), so the total number of constraints in the system is 3C, where C is the number of contacts. If 3C = 6N ($Z_a = 2C/N = 4$) the system is statically determinate. If $Z_a > 4$, the system is redundant in that it has more contacts than necessary to satisfy equilibrium. If $Z_a < 4$, the system is unstable and the system becomes a mechanism, which can lead to further loss of contacts.

Consider a 3D assembly for $\mu = 0$, i.e. frictionless contacts so that there is only a contact normal force on any contact and the number of the independent unknown forces (constraints) at a contact is reduced to 1. Therefore, the number of constraints is C (no

tangential forces), and the number of degrees of freedom is 3N (no rotation). Consequently, when $Z_a = 6$, the system is statically determinate; when $Z_a > 6$, the system is redundant; and when $Z_a < 6$, the system is a mechanism or unstable.
Because of the absence of a gravity field in the simulations, there may exist particles with no contacts or only one contact and, therefore, as explained in section 2.4.3, in order to examine stability/instability the appropriate definition of coordination number above is mechanical coordination number Z_m as defined by (2.11).

In the simulations the interparticle friction is finite, u = 0.5, and therefore the limiting value of Z_m is expected to occur between 4 and 6. It would be expected that for a system with a friction efficient of 0.5, a limiting coordination number (for keeping the system statically determinate) is a value between 4 and 6, which depends on the percentage of sliding contacts. However, the sliding contact is always found to be less than 10% for all the samples (the evolutions are not shown in this thesis). This means that more than 90% of the contacts are ‘non-sliding’ and thus it would be expected that the limiting mechanical coordination number to be only slightly greater than 4. It is difficult to ascertain exactly what the value should be and, therefore, $Z_m = 4$ will be assumed to be a good approximation. The physical meaning of this limiting mechanical coordination number can be associated as follows. When $Z_m > 4$, the sample can be said to be solid-like (stable); when $Z_m < 4$, the sample can be said to be liquid-like (not stable and a mechanism occurs); and when $Z_m = 4$, the sample can be said to be in a phase transition state from solid-like to liquid-like.

From Fig. 5.5, it can be concluded that in undrained axisymmetric compression, a phase transition occurs clearly for the very loose systems and occurs before the SS is reached and the samples cannot be recovered to solid-like states; a phase transition occurs for the medium loose systems (with porosities of 0.409 and 407) before the QSS is reached. However, for the medium loose system with a porosity of 0.405 a phase transition does not occur. In chapter 3, for drained constant mean stress simulations, the unique porosity at the critical state was found to be 0.407 for all samples. The results of the undrained simulations suggest that a phase transition from solid-like to liquid-like behaviour only occurs for samples with porosities greater than the critical state porosity, for a given initial stress level.

It was mentioned in section 5.2 that the locus of the initial peak values of q on the different effective stress paths fall onto a unique line, called the instability line by Lade (1992). It is interesting to observe that for all the loose systems, the initial peak states of q (Lade instability) occur when the corresponding Z_m is about 4.5 irrespective of the initial porosity, see Fig. 5.6.

Figure 5.7 shows the evolution of deviator fabric plotted against deviator strain. Following Chapter 2, a deviator fabric (ϕ_1 - ϕ_3) can be used to describe structural anisotropy. At the initial state before undrained shearing, both the stress and fabric are approximately isotropic, so the initial deviator fabric is almost zero. During the subsequent undrained shearing, the change in deviator fabric is induced by the applied

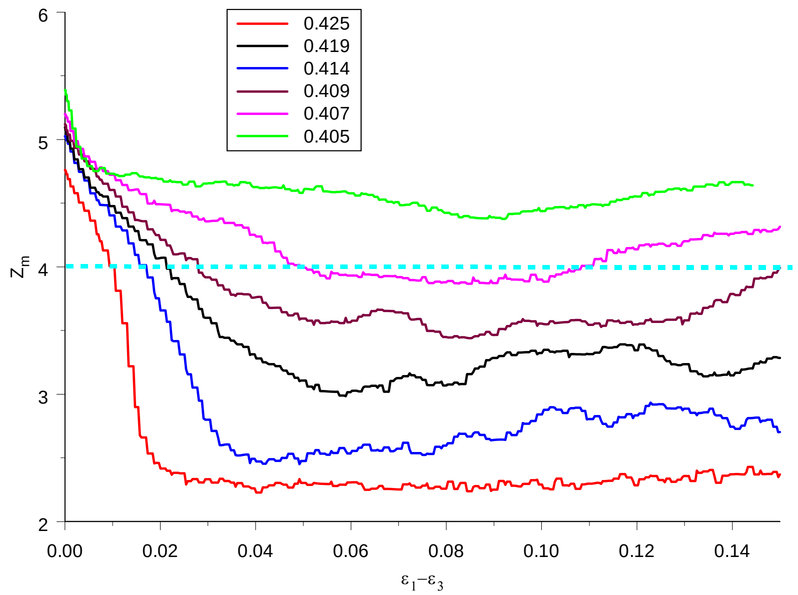

Fig. 5.5 Evolution of mechanical coordination number

[key refers to porosity]

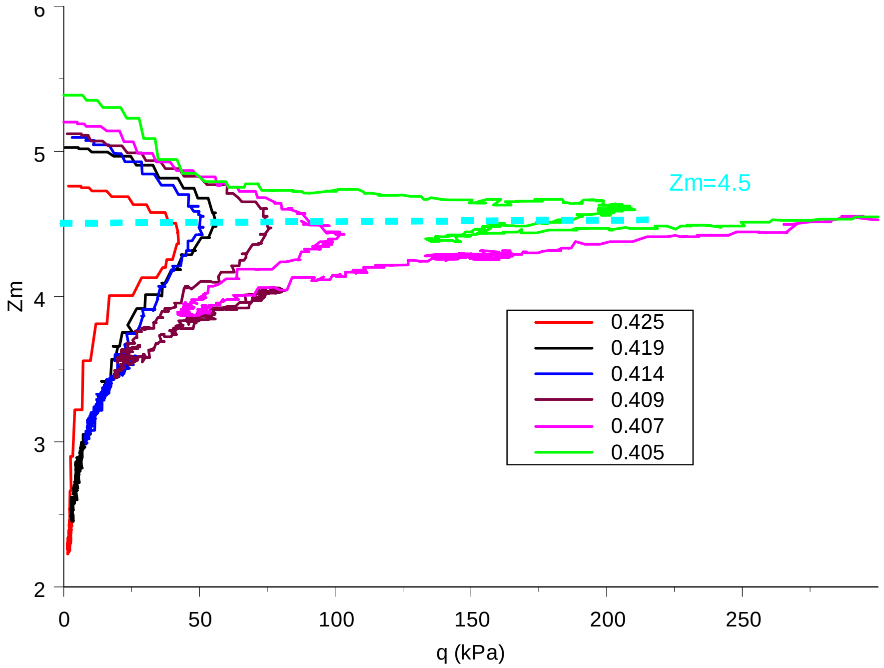

Fig. 5.6 Z_m against q

[key refers to porosity]

strain, so the term “induced structural anisotropy” can be used in place of the deviator fabric. However, in the discussion of the evolution coordination number, when $Z_m < 4$, the system is a mechanism and no longer a stable structure, the induced structural anisotropy loses its meaning in these undrained simulations once the phase transition has occurred. The fabric tensor defined by (2.12) was originally used to define the structural anisotropy in terms of the distribution of the orientation of contact normals. In fluid-like (collisional) systems, the fabric tensor defines the distribution of the orientations of particle collisions. A deviator fabric (>0) indicates an anisotropic distribution of collisional orientations.

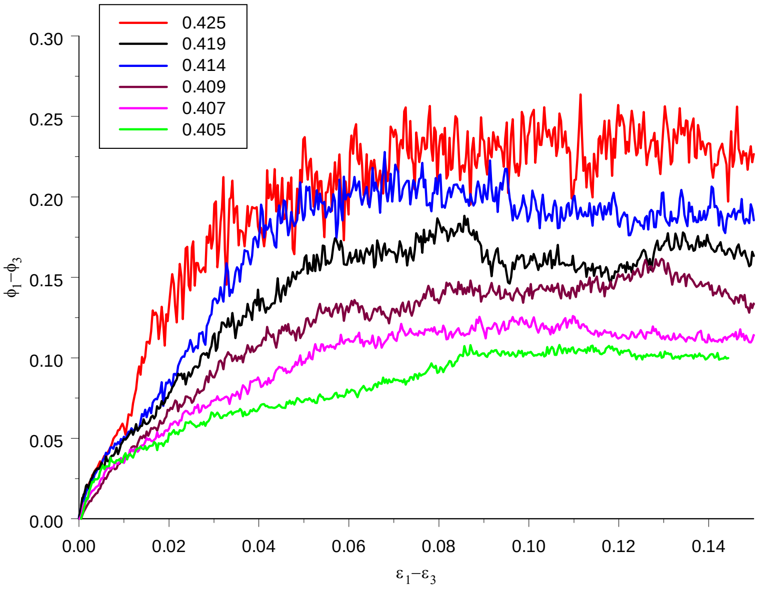

Fig. 5.7 Evolution of deviator fabric

[key refers to porosity]

It can be seen that the deviator fabric at relatively large strain (especially in the fluid-like state) is dependent on porosity. The higher the porosity, the higher deviator fabric, which is similar to the evolution of sinφ. By comparing Figs. 5.2 and 5.7, the reverse behaviour of deviator stress and deviator fabric are observed, which means the deviator fabric does not relate to q when a mechanism occurs. When the deviator strain is greater than 0.08, the deviator fabric remains more or less constant at different values dependent on porosity. It is also noted that the amplitude of the fluctuations in the deviator fabric increases with increasing porosity.

5.5 Simulation results and discussion for the loose sample (porosity = 0.419) with preshearing

Finge et al. (2003) investigated the effects of preloading history on the undrained behaviour of saturated loose Hostun RF sand. They presented a detailed analysis of the effects induced by isotropic overconsolidation and by drained cycle preshear on the subsequent undrained behaviour of Hostun sand, both in compression and extension. The analysis of results focused on the evolution of the behaviour according to the deviator stress achieved during a drained cycle preshear or as function of the overconsolidation ratio. Some plots of the results of the effect of the drained cycle preshear on the subsequent undrained shear are shown in Fig. 5.8. An interesting phenomenon in Fig. 5.8 pointed out by Finge et al. (2003), is that all the presheared samples have the same initial positive slope in q-p space and the initial stress path for the undrained shear lies on a unique curved line independent of the q_{max} during the preshear process, which forms a limiting stress boundary in the stress space not crossed by all presheared samples. A similar phenomenon in physical experiments was observed Gajo and Piffer (1999). As with the increase of q_{max} in the drained cycle (the preshear loading process), Finge et al. (2003) observed that the samples exhibit static liquefaction, temporary liquefaction and complete stability respectively in subsequent undrained compression tests depending on the q_{max} obtained in preloading. Finge et al. (2003) attributed the results to the induced anisotropy caused by the preshearing process.

The loose sample with a porosity of 0.419 was chosen to examine the effect of preshearing. From an initial isotropic stress state (p = 100kPa) the sample was presheared by applying ‘drained’ axisymmetric compression at constant $\sigma_2 = \sigma_3 = 100$ kPa until the deviator stress reached the desired value. The sample was then unloaded back to the initial isotropic state of stress. In this manner the loose sample was prestressed to q = 20 kPa, 40kPa, and 60kPa to provide three samples for subsequent simulations of constant volume (undrained) tests. Since the initial sample is very loose preshearing resulted in volumetric contraction during loading and volumetric expansion during unloading. Due to irrecoverable volume change caused by the preshearing process the pressheared samples are denser compared to the original one, see table 5.1.

Table 5.1 Sample data at the end of preshearing

Preshear q_{max} (kPa)	porosity	Z_m	$\phi_1-\phi_3$	Z_m at the end of preshear loading
0	0.4190	5.03	0.004	5.03
20	0.4185	4.95	0.004	4.92
40	0.4177	4.91	0.002	4.84
60	0.4143	4.83	0.006	4.79

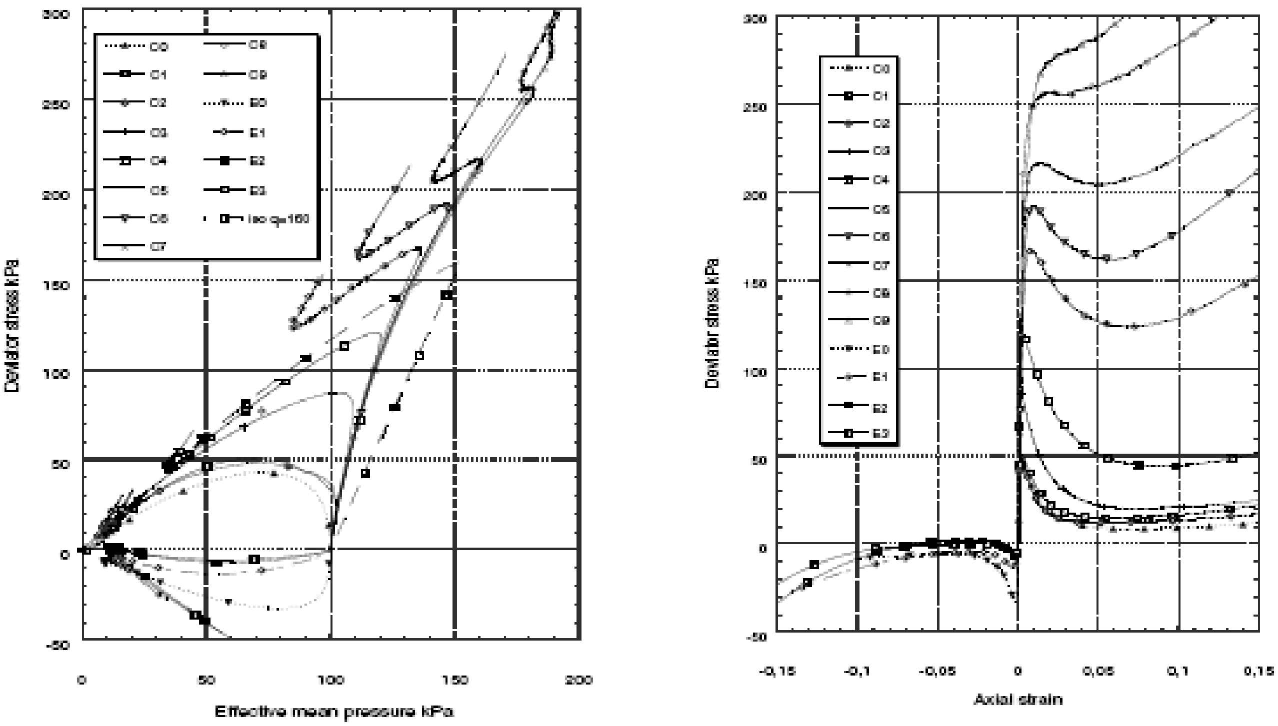

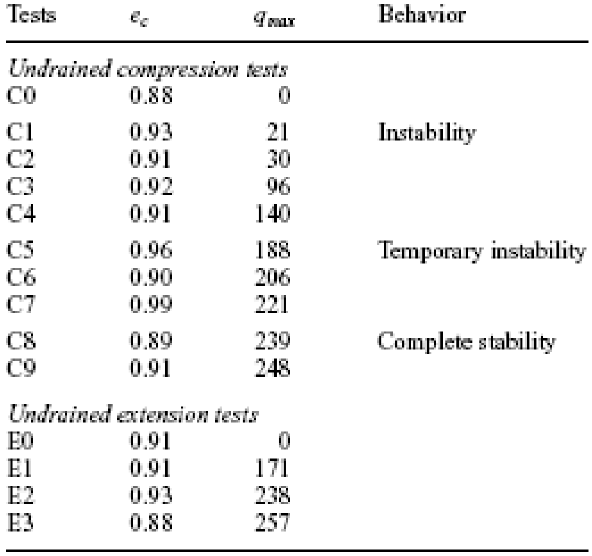

Tests	e_c	q_{max}	Behavior
Undrained compression tests			
C0	0.88	0	
C1	0.93	21	Instability
C2	0.91	30	
C3	0.92	96	
C4	0.91	140	
C5	0.96	188	Temporary instability
C6	0.90	206	
C7	0.99	221	
C8	0.89	239	Complete stability
C9	0.91	248	
Undrained extension tests			
E0	0.91	0	
E1	0.91	171	
E2	0.93	238	
E3	0.88	257	

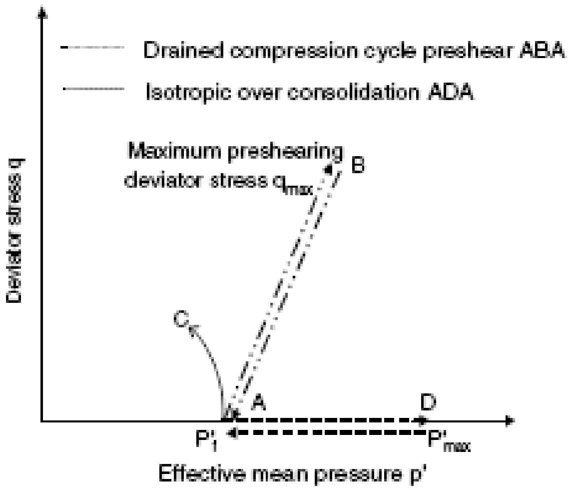

Fig. 5.8 Experimental data from Finge et al (2003)

5.5.1 Macroscopic and microscopic behaviour

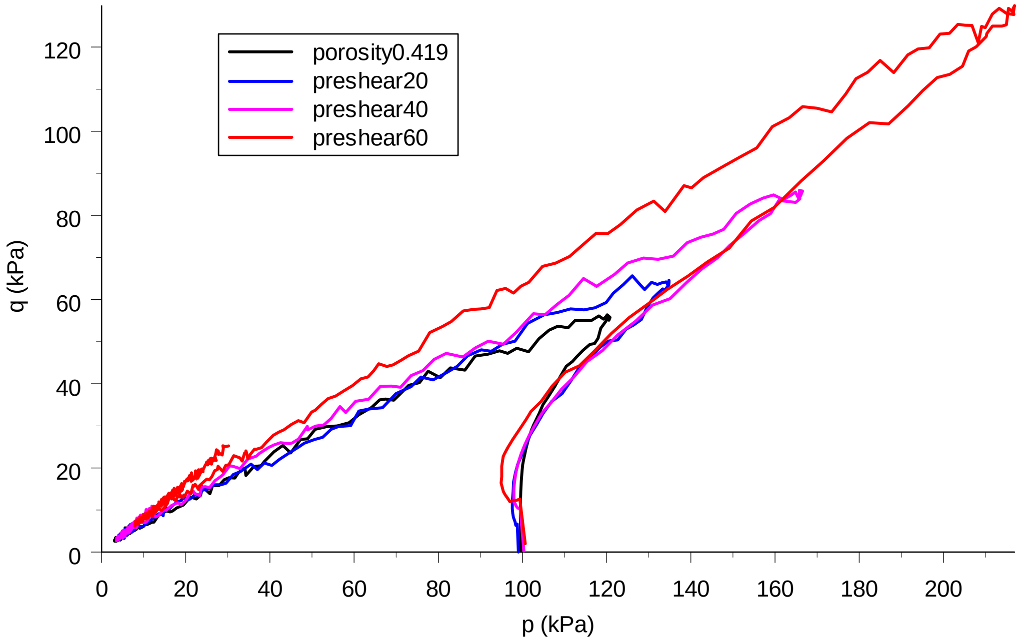

Fig. 5.9 Constant volume stress paths

Figure 5.9 shows the stress paths for the undrained behaviour of the loose sample with and without preshearing history. It can be seen that the undrained behaviour with preshearing history is different from that without preshearing history. It is interesting to note that the samples follow the same initial stress path prior to reaching the maximum deviator stress. The same phenomenon was observed by Finge et al. (2003), see Fig. 5.8, who suggested that this was a limiting stress boundary in stress space. As shown in Fig. 5.8, Finge et al. (2003) observed that presheared samples can exhibit static liquefaction, temporary liquefaction or complete stability depending on the amount of preshear applied. Fig. 5.9 shows that, in the DEM simulations, only the sample prestressed to a deviator stress of 60 kPa exhibited, to some extent, temporary liquefaction.

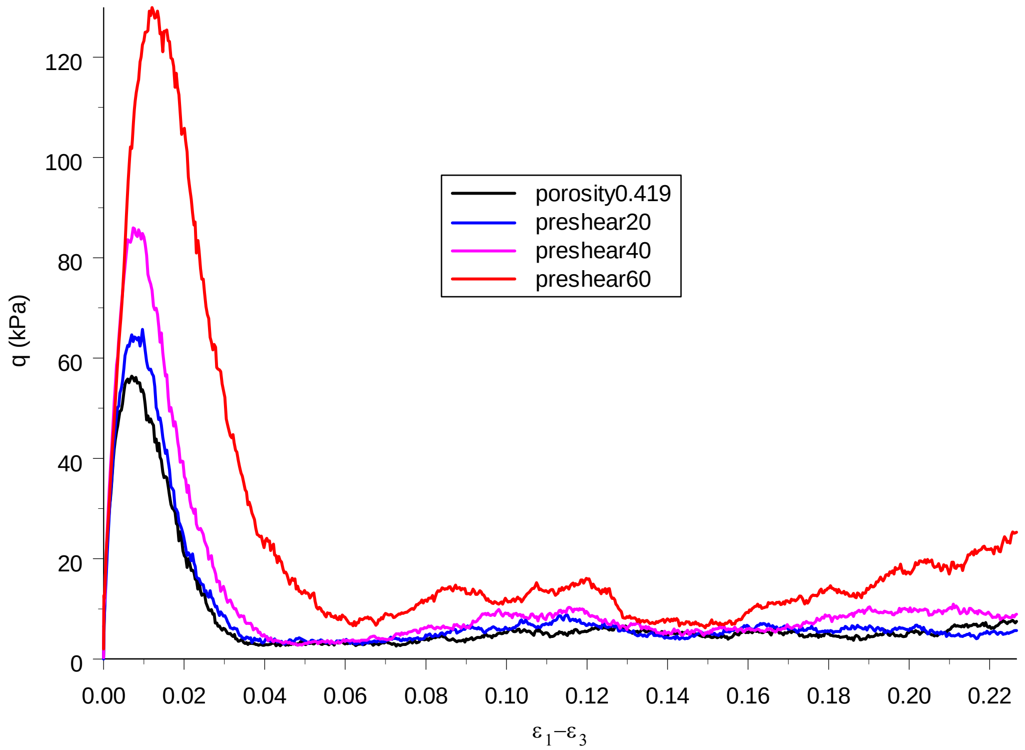

Fig. 5.10 Evolution of deviator stress

Figure 5.10 shows the deviator stress plotted against deviator strain for the presheared and unpresheared samples. It can be seen that the initial slope is identical for the presheared and unpresheared samples. The maximum deviator stress increases if the amount of preshear is increased. The two samples presheared to deviator stresses of 20 kPa and 40 kPa exhibit steady state at large strains but a higher deviator stress at steady state compared with that of the unpresheared sample. The sample presheared to a deviator stress of 60 kPa exhibits quasi-steady state since it can be seen that the deviator stress is increasing slightly at large strains.

Figure 5.11 shows the mean stress plotted against deviator strain for the presheared and unpresheared samples. It can be seen that the initial slope is identical for the presheared and unpresheared samples and p increases initially, which is similar to the evolutions of q. The evolution of p is related to the tendency of dilation for constant volume conditions, i.e. pore pressure, as discussed in section 5.4.

Figure 5.12 shows sinφ plotted against deviator strain for all the presheared and unpresheared samples. Although Fig. 5.10 and Fig. 5.11 show differences for the presheared and unpresheared samples in terms of the evolution of q and p respectively. Fig. 5.12 shows that a more or less unique evolution of sinφ is obtained, which means that q/p is unique. Fig. 5.12 also indicates that the preshear process does not affect the ultimate state line in q-p space for undrained axisymmetric compression conditions.

Figure 5.13 shows the evolution of the mechanical coordination number against deviator strain for the presheared and unpresheared samples. It is observed that the SS (QSS) is associated with the minimum Z_m for both presheared and unpresheared samples (porosity 0.419); and that preshear60 exhibits a little increase in Z_m after the QSS. The value of Z_m is well below 4 (the limiting mechanical coordination number) after some early straining, so there is a mechanism occurring. By comparing Fig.5.13 and Fig.5.10, it can be found that the initial peak states of q are all associated with the unique Z_m of 4.5. So it can be concluded that the preshear process does not influence this value of Z_m at the initial peak deviator stress.

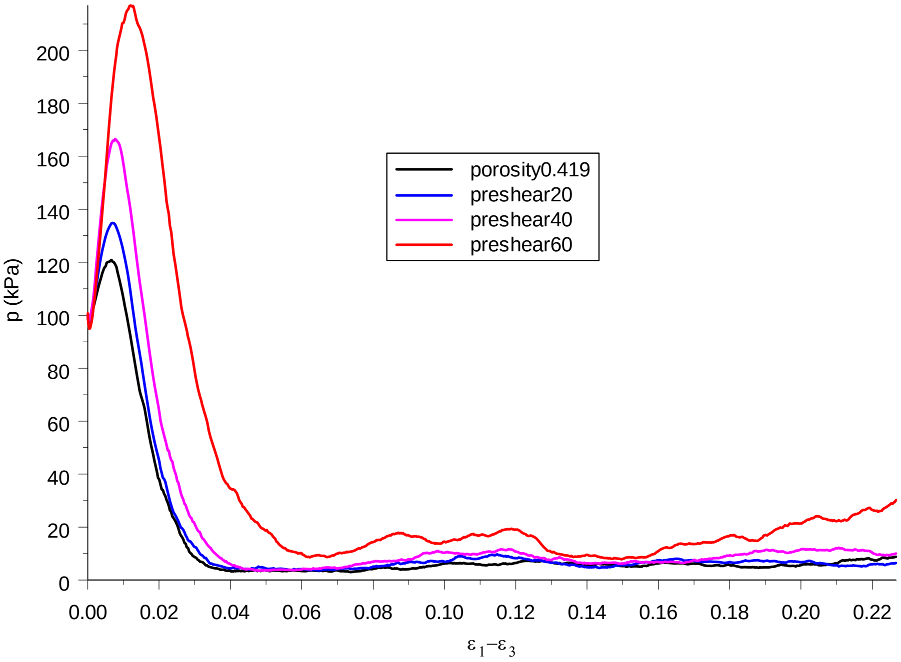

Fig. 5.11 Evolution of mean stress

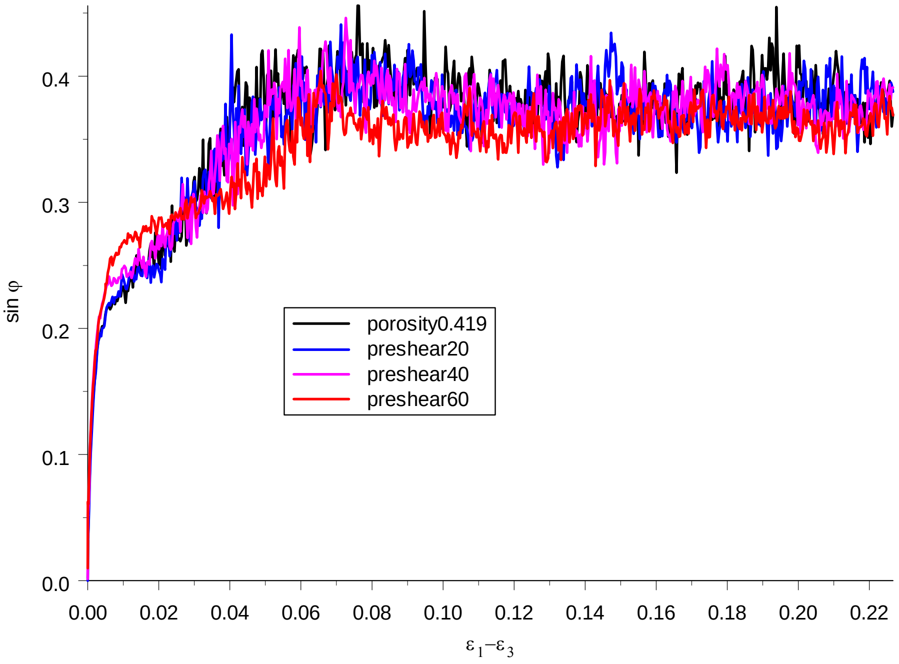

Fig. 5.12 Evolution of sinφ

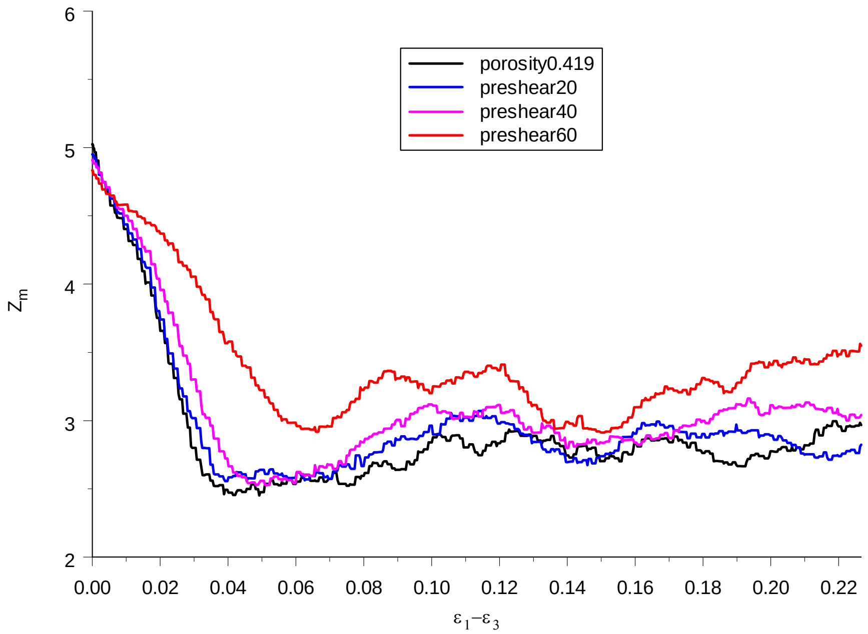

Fig. 5.13 Evolution of the mechanical coordination number

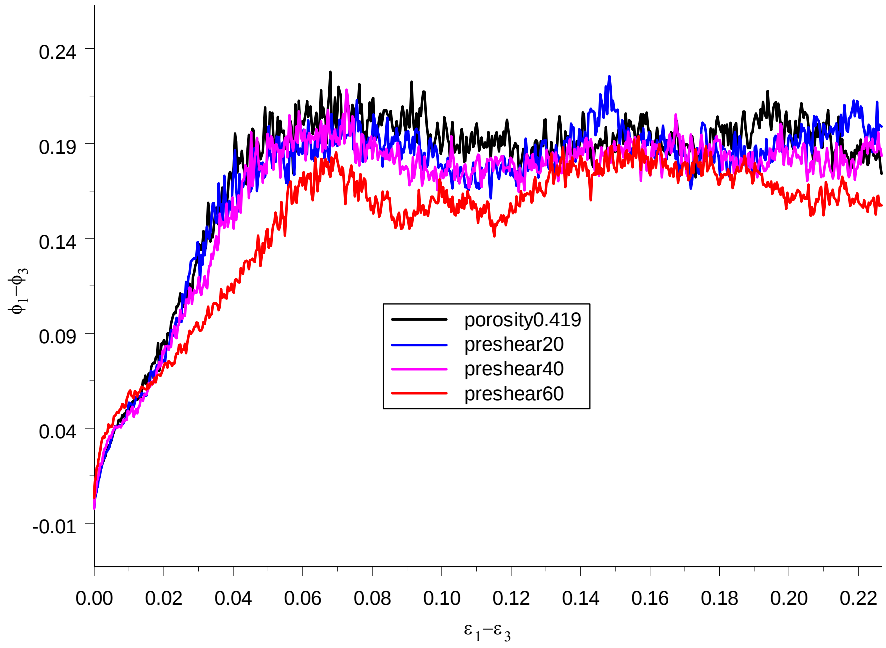

Fig. 5.14 Evolution of deviator fabric

Figure 5.14 shows the evolution of deviator fabric for the presheared and unpresheared samples. Deviator fabric increases for all the presheared and unpresheared samples until it becomes more or less constant at large strains. Preshear20 and preshear40 have almost identical evolution of deviator fabric as that of porosity0.419, while preshear60 shows a lower value after a deviator strain of 0.02 (a little after the initial peak q). Finge et al. (2003) suggested that the reason for the difference between the undrained tests of the presheared and original unpresheared ones is that the preshear processes modifies the macrostructure of the material and creates an induced anisotropy expressed, in stress space, via a slope of the effective stress path toward the positive p-axis. However, the previous discussion showed that the DEM simulations indicate that the preshear process does not change the induced anisotropy, in agreement with Gajo and Piffer (1999). This can be seen more clearly in Fig. 5.14 and is described as follows. Firstly, after the preshear process, all the samples come back to isotropic stress state, which is also associated with isotropic fabric state. Secondly, the initial slopes for the presheared and unpresheared on q-p space are very similar, which is associated with the same initial evolution of the deviator fabric (before a deviator strain of 0.02 which corresponds to the initial peak of q in Fig. 5.10).

5.5.2 Comparison of preshear60 and porosity0.414

Figure 5.15 shows the comparison of preshear60 and porosity0.414 under undrained conditions. The two samples have essentially the same porosity. The evolutions of deviator fabric are essentially the same. The evolutions of q (or p) are very different and the preshear60 exhibits a much greater value of q (or p) than porosity0.414, although the initial mechanical coordination number for the preshear60 is smaller. This implies the sample’s undrained behaviour is stress history dependent.

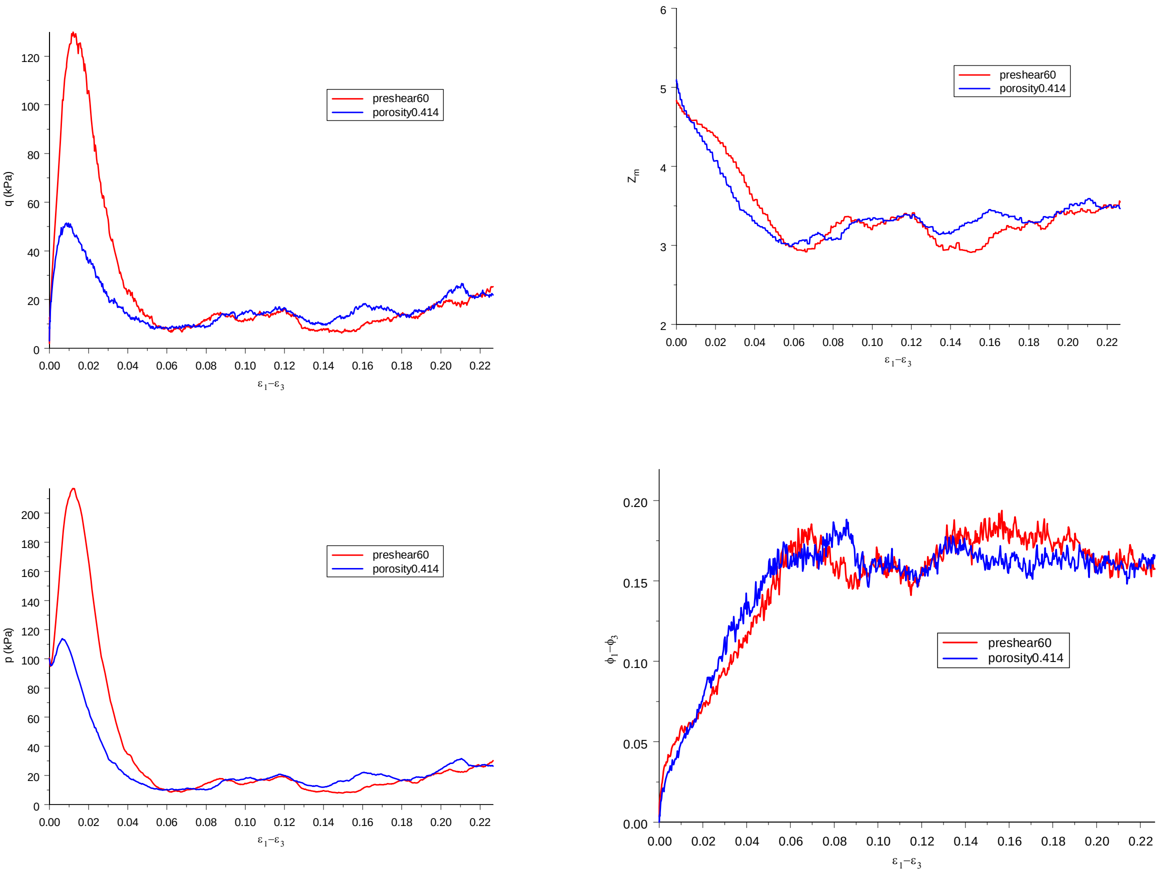

Fig. 5.15 Plots for preshear60 and porosity0.414

5.6 Undrained simulations at low strain rates

Figure 5.16 shows the results of a loose sample (porosity = 0.409) at low strain rates ($1.0\times10^{-5}s^{-1}$, $-5.0\times10^{-6}s^{-1}$ and $-5.0\times10^{-6}s^{-1}$) under undrained conditions. The medium loose sample (0.409), which exhibited temporary liquefaction at higher strain rates, exhibits liquefaction (nearly static liquefaction) at low strain rates. This could imply that the undrained behaviour is strain rate dependent but further investigation would be needed in the future.

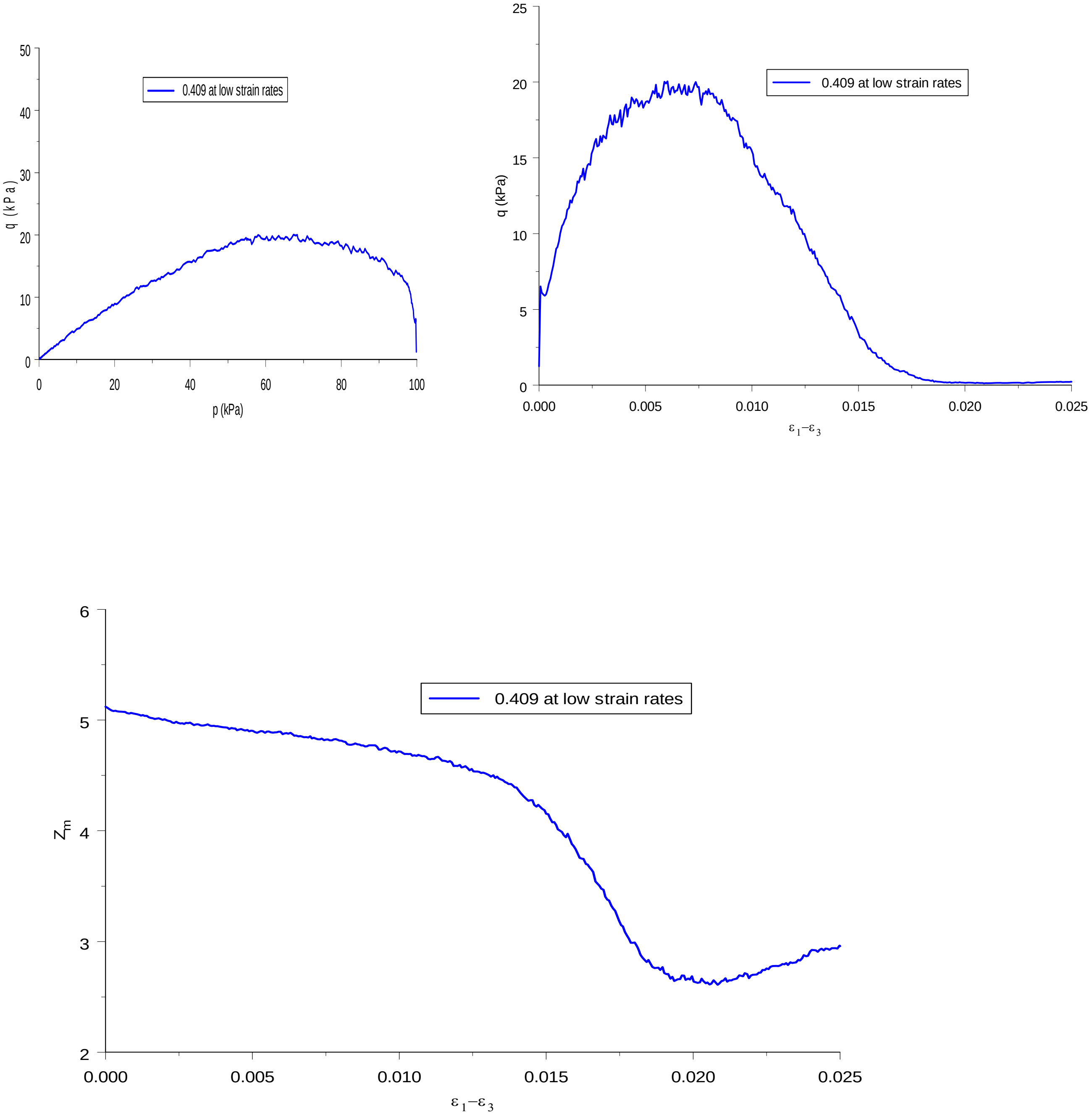

Fig. 5.16 Undrained results at low strain rates
[key refers to porosity]

5.7 Summary

This chapter has mainly presented the results of simulations under undrained axisymmetric compression with and without preshearing at higher strain rates. The undrained condition is modelled in ‘dry’ constant volume tests without considering the interstitial fluid.

The steady and quasi-steady state behaviour is well captured in the DEM simulations for higher strain rates. For the systems without preshearing, it is found that the undrained behaviour is mainly governed by the porosity. As porosity decreases, the system exhibits higher resistance to liquefaction. The very loose systems exhibit steady state behaviour (liquefaction), while the medium loose systems exhibit quasi-steady state behaviour (temporary liquefaction).

Liquefaction (or temporary liquefaction) for very loose samples (or medium loose samples) has not been well explained by any existing theory. The simulation results in this chapter show that liquefaction (or temporary liquefaction) can be explained by structural mechanism with the introduction of the limiting mechanical coordination number. The value of the limiting mechanical coordination number is found to be 4. A phase transition is defined to be associated with the state in which the limiting mechanical coordination number occurs. The results of the undrained simulations suggest that a phase transition from solid-like to liquid-like behaviour only occurs for samples with porosities greater than the critical state porosity, for a given initial stress level.

The presheared simulation results show that the presheared samples are denser compared with the original unpresheared sample, and exhibit higher resistance to liquefaction. The DEM simulation also captures the limiting boundary in q-p space as observed by Finge et al. (2003) as well as Gajo and Piffer (1999), which cannot be crossed by any of the presheared samples.

The undrained behaviour is found to be strain rate dependent and stress history dependent for loose samples.

CHAPTER 6: ‘UNDRAINED’ PLANE STRAIN SIMULATIONS

6.1 Introduction

In routine undrained laboratory testing and design, only undrained axisymmetric compression tests are performed and the data from undrained axisymmetric compression tests are used in undrained analysis. In DEM, undrained plane strain simulations can be performed in strain control mode while keeping zero strain in one of the principal strain directions.

All undrained plane strain simulations in this chapter were carried out in a periodic cell with strain control mode, and the specified strain-rates in the three principal strain directions were set to $1\times10^{-4}\,s^{-1}$, 0 and $-1\times10^{-4}\,s^{-1}$ respectively. All the other simulation details can be found in Chapters 3 and 6.

6.2 Simulations results

Figure 6.1 shows the constant volume stress path (CVSP) behaviour with deviator stress plotted against mean stress for all the loose systems under undrained plane strain conditions. It can be seen from Fig. 6.1 that the overall trends are not much different from those observed in Fig. 5.1. However, the medium loose sample (with a porosity of 0.405) exhibits ‘dense’ undrained behaviour. The three loosest samples exhibit steady state (SS) behaviour and one medium loose sample (with a porosity of 0.409) exhibit quasi-steady state (QSS) behaviour.

Figure 6.2 shows the evolution of the deviator stress plotted against deviator strain for all the loose systems. It can be seen that for the three very loose samples, the initial peak of deviator stress occurs at small strains. Comparing with Fig. 5.2, the corresponding peak values are greater than those in undrained axisymmetric compression for each sample. From the results obtained for the loose samples, it can be concluded that the initial peak value of q is dependent on the porosity and, the looser a sample is the faster the peak is reached and the smaller the peak value of q (the little deviation between porosity 0.419 and 0.414 is ignored here). Only the very loose systems appear to exhibit SS. If the minimum deviator stress at SS and QSS is taken as the ultimate shear strength, then it can be said that this ultimate shear strength is dependent on porosity, decreasing with increasing porosity. Also, if the initial peak of deviator stress is taken as the peak shear strength, then it can also be said that this peak shear strength is dependent on porosity, decreasing with increasing porosity.

Figure 6.3 shows the evolution of the mean stress plotted against deviator strain for all the loose systems. It can be seen that, for all systems, the evolution of mean stress is qualitatively the same as the evolution of deviator stress, as shown in Fig. 6.2.

Figure 6.4 shows the evolution of sinφ plotted against deviator strain for all the loose systems. In axisymmetric compression $q/p = 6\sin\varphi/(3-\sin\varphi)$, which is not true in plane strain. This is why the slope of q/p in Fig. 6.1 is not associated with sinφ. It can be seen that the evolution of sinφ is identical at the very early stage of loading for all loose samples. For the loosest sample, fluctuations occur at a deviator strain of 0.02 which corresponds to the deviator strain just before minimum q occurs (near SS). For the other two very loose samples, fluctuations occur at a greater deviator strain and the amplitude is smaller compared with that of the loosest sample. For the three very loose samples, relatively stable fluctuations occur after a deviator strain of 0.06. For the three medium loose samples, the fluctuations can be ignored compared with those of the very loose ones. The fluctuations at SS for the very loose samples indicates that, the stresses (q and p) are not constant at SS. It can be seen that at SS there is not a unique value (independent of porosity) of $\sin\varphi_{ss}$, and the average value of $\sin\varphi_{ss}$ increases as porosity increases. The only literature reporting experimental results for undrained plane strain tests appears to be Lee (1970), who showed the friction angle at failure in undrained plane strain was 4° to 5° greater than that in undrained axisymmetric compression, which is similar to the difference found by Conforth (1964) for drained tests and the results of the DEM simulations reported in chapters 3 and 4.

Figure 6.5 shows evolution of $\sigma_2/(\sigma_1+\sigma_3)$ against deviator strain for all the loose systems. In undrained plane strain, it can be seen that $\sigma_2/(\sigma_1+\sigma_3)$ reduces from an initial value of 0.5 to values between 0.38 to 0.45.

Figure 6.6 shows the evolution of Bishop's b_σ parameter $[b = (\sigma_2-\sigma_3)/(\sigma_1-\sigma_3)]$ against deviator strain for all the loose systems. In constant mean stress tests, the evolution of b describes the stress path on the deviatoric plane. In constant volume tests, evolution of b

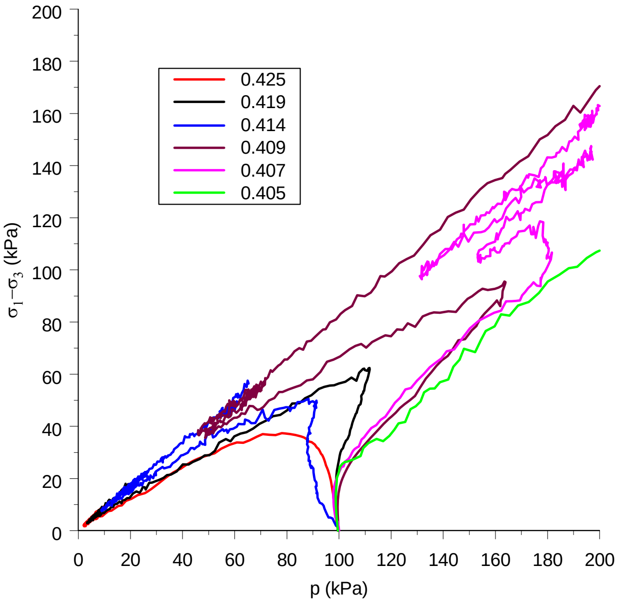

Fig. 6.1 Constant volume stress paths
[key refers to porosity]

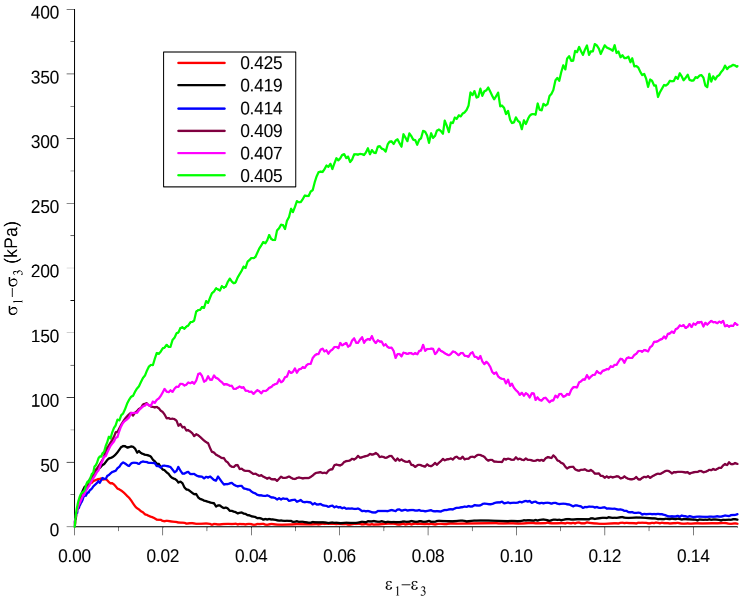

Fig. 6.2 Evolution of deviator stress
[key refers to porosity]

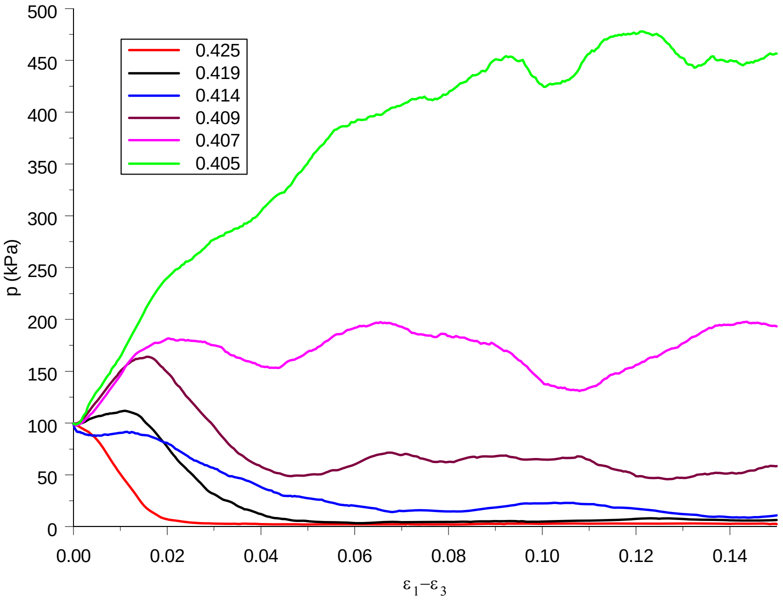

Fig. 6.3 Evolution of mean stress

[key refers to porosity]

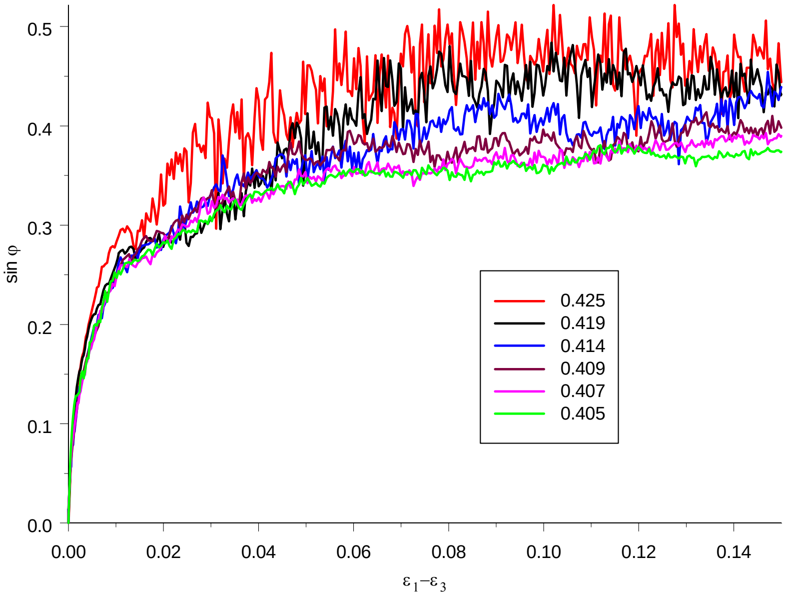

Fig. 6.4 Evolution of sinφ

[key refers to porosity]

describes the stress path ‘projected’ in a deviatoric plane as the mean stress is changing. Initially, b is indeterminate (0/0). With further straining, b reduces to values in the range of 0.26 to 0.38.

Figure 6.7 shows the evolution of mechanical coordination number (Z_m) plotted against deviator strain for all the loose systems, where it is found that the mechanical coordination number decreases initially for all the systems until a minimum value is reached. The initial drop of the mechanical coordination number may be mainly because of sudden change in the loading conditions. The minimum values of Z_m occur at strains coincident with the SS or QSS. This can be found by comparing Figs 6.7 and 6.2. The values of The minimum values of Z_m associated with SS or QSS decrease with increasing porosity.

The limiting mechanical coordination number is related to phase transition of the system as discussed in chapter 5 and a limiting Z_m with a value of 4 was suggested in undrained axisymmetric compression simulations. Based on this limiting Z_m, it can be said that the three very loose samples exhibit fluid-like behaviour. All the other samples can be said to be always in a solid-like state.

Fig. 6.8 and Fig. 5.6 suggest that the initial peak q is associated with a unique value of mechanical coordination number (Z_m = 4.5), irrespective of porosity as well as strain conditions.

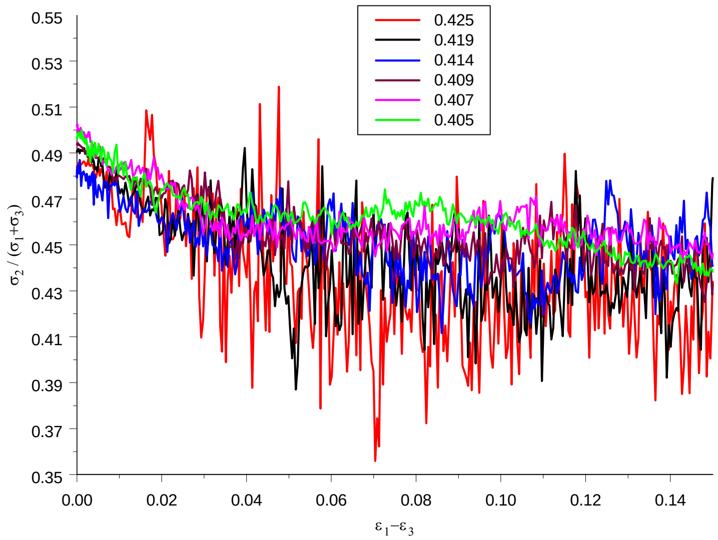

Fig. 6.5 Evolution of $\sigma_2 / (\sigma_1+\sigma_3)$

[key refers to porosity]

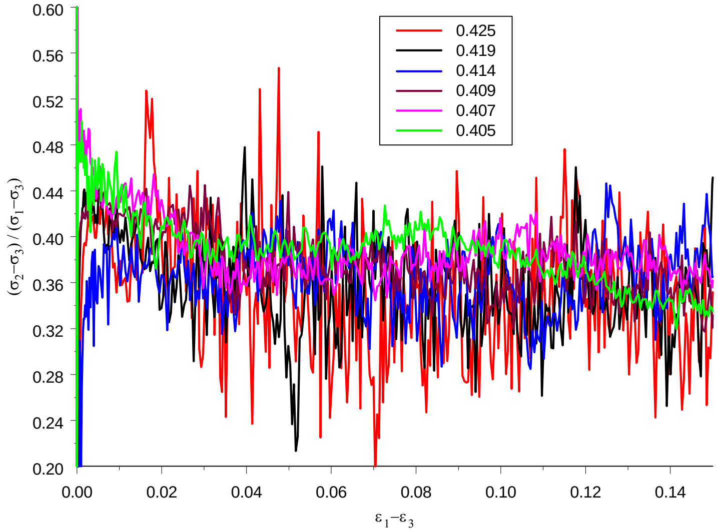

Fig. 6.6 Evolution of $(\sigma_2-\sigma_3)/(\sigma_1-\sigma_3)$

[key refers to porosity]

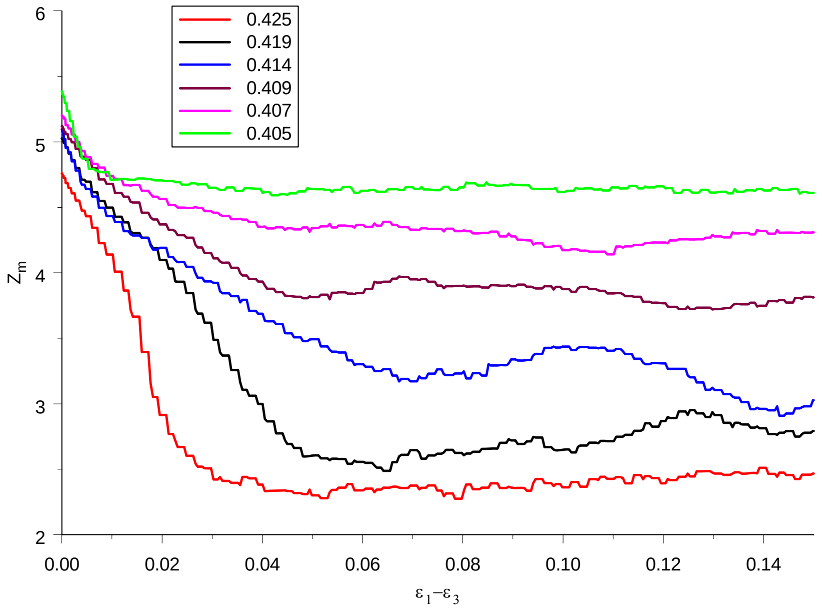

Fig. 6.7 Evolution of mechanical coordination number

[key refers to porosity]

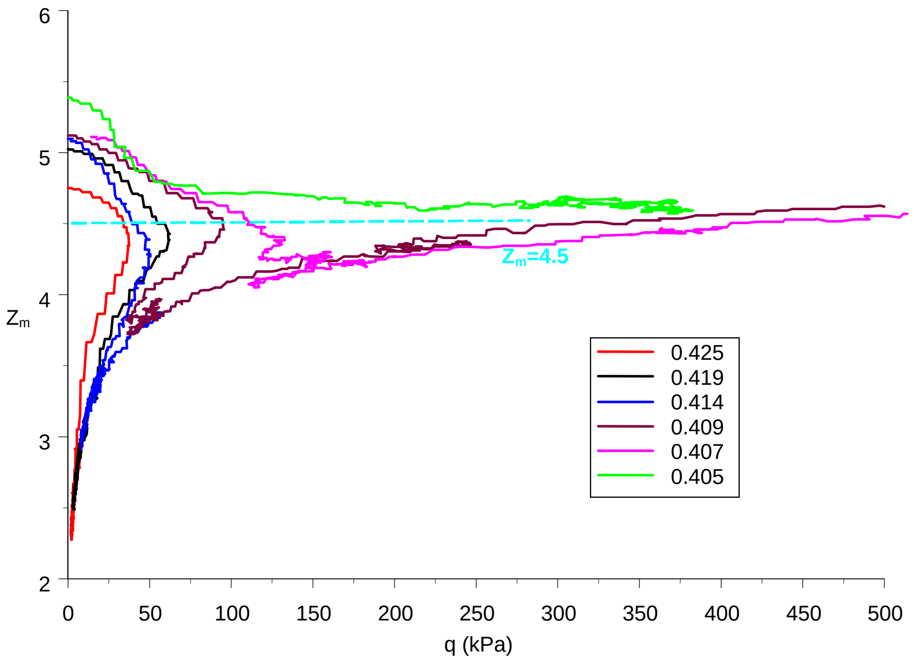

Fig. 6.8 Mechanical coordination number against deviator stress

[key refers to porosity]

Figure 6.9 shows the evolution of deviator fabric plotted against deviator strain for all the loose systems. It can be seen that the trends of the evolutions of deviator stress (Fig. 6.2) and deviator fabric are very different. As discussed in Chapter 5, the fabric tensor defines the distribution of the orientation of particle collisions in fluid-like (collisional) systems when mechanical coordination number is less than 4 and a deviator fabric (>0) indicates an anisotropic distribution of collisional orientation. It can be seen that the deviator fabric at relatively large strain (especially in the fluid-like state) is dependent on porosity. For fluid-like systems, the higher the porosity, the higher the deviator fabric.

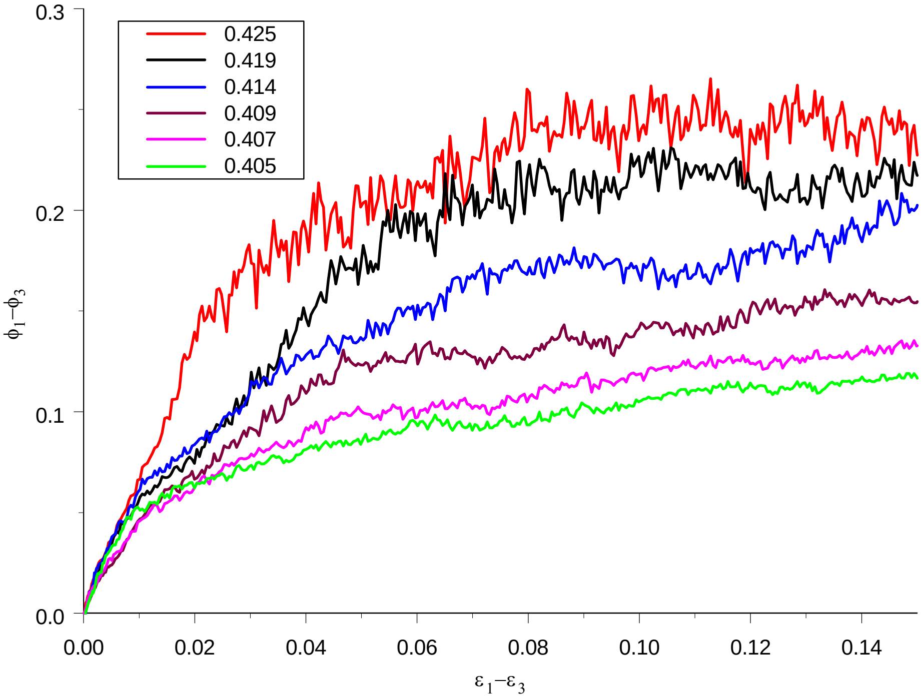

Fig. 6.9 Evolution of deviator fabric
[key refers to porosity]

6.3 Summary

In this chapter, results of undrained (or constant volume) plane strain simulations have been reported. In the literature, almost no results on undrained plane strain have been reported in detail. Undrained plane strain DEM simulations have never been reported before.

It has been demonstrated in this chapter that the strain condition is an important factor influencing the undrained behaviour especially in terms of the resistance to liquefaction. Only the very loose samples exhibit liquefaction, and the other loose samples remain in a solid-like state throughtout the tests.

This chapter has confirmed the existence of a unique mechanical coordination number associating with the initial peak q. This unique Z_m is found to have the same value (4.5) as found in chapter 5, which indicates its independence of porosities and strain conditions.

CHAPTER 7: COMPARISON

7.1 Introduction

Following the previous chapters, this chapter presents a more detailed comparison between drained axisymmetric compression (DAC) and drained plane strain (DPS) simulations, as well as undrained axisymmetric compression (UAC) and undrained plane strain (UPS) simulations. As the complete information about any parameter's evolution (like any stress parameter, and also any strain parameter) can already be completely derived from the plots in the previous chapters, the information presented in this chapter is, in a sense, only a reorganisation of the previous chapters, and therefore all the information presented in this chapter is not much different from that in the previous chapters. However, some direct straightforward comparisons will make the differences more clear. Not many researchers have published comparisons of DAC and DPS (nor those of UAC and UPS) behaviour of granular materials such as sand in the literature, although this topic is of interest to both researchers and practical engineers. In the literature, many shear strength criteria have been proposed and some of them will be discussed in detail and compared in section 7.3. Published experimental comparisons, such as Cornforth (1964) and Lee (1970), have been reviewed in Chapter 4. There has not been any published work on such comparisons by DEM simulations. Therefore, in this chapter, the discussion will follow a brief description of the parameters chosen for the plotting without a review section of literature work. Some additional literature will be mentioned in the discussions.

7.2 The parameters used for plotting

For a given sample, the stress conditions in plane strain ($\sigma_1 > \sigma_2 > \sigma_3$) and in axisymmetric compression ($\sigma_1 > \sigma_2 = \sigma_3$) are different. The strain conditions in plane strain ($\varepsilon_1 > \varepsilon_2 > \varepsilon_3$ with $\varepsilon_2 = 0$) and in axisymmetric compression ($\varepsilon_1 > \varepsilon_2 = \varepsilon_3$) are also different. A difficulty arises as to how to quantify the difference between axisymmetric compression and plane strain. A possible comparison of stress in axisymmetric compression and plane strain may be to compare σ_1, σ_2, and σ_3. However, such a treatment may not mean much as the principal stresses themselves are not directly related to shear strength parameters. For this consideration, most chosen stress parameters in this chapter are explicitly related to mobilised shear strength such as the mobilised Mohr-Coulomb shear strength parameter sinφ. Some stress and strain parameters used for this chapter (the definitions are consistent throughout this thesis) are defined as follows:

Deviator stress q (the difference between the major and minor principal stresses)

$$q = \sigma_1 - \sigma_3 \tag{7.1}$$

Deviatoric stress

$$q_{dev} = \sqrt{\frac{(\sigma_1 - \sigma_2)^2 + (\sigma_1 - \sigma_3)^2 + (\sigma_2 - \sigma_3)^2}{3}} \tag{7.2}$$

Deviator strain (the difference between the major and minor principal strains)

$$\varepsilon_{13} = \varepsilon_1 - \varepsilon_3 \tag{7.3}$$

Deviatoric strain

$$\varepsilon_{dev} = \sqrt{\frac{(\varepsilon_1 - \varepsilon_2)^2 + (\varepsilon_1 - \varepsilon_3)^2 + (\varepsilon_2 - \varepsilon_3)^2}{3}} \tag{7.4}$$

It should be mentioned that the above definition of deviatoric stress/strain does not degenerate to deviator stress/strain in axisymmetric compression condition, e.g. $q_{dev} = \sqrt{\frac{2}{3}}q$ and $\varepsilon_{dev} = \sqrt{\frac{2}{3}}(\varepsilon_1 - \varepsilon_3)$ in axisymmetric compression. In general (such as in plane strain), the relationships between deviatoric and deviator stress/strain do not have such a simple form. It should also be mentioned that the above definitions (especially deviatoric stress/strain) are different from those in some published literature, e.g. Georgiadis et al. (2004) who defined deviatoric stress as $\sqrt{\frac{(\sigma_1 - \sigma_2)^2 + (\sigma_1 - \sigma_3)^2 + (\sigma_2 - \sigma_3)^2}{6}}$. A similar difficulty arises for the fabric tensor. But, for the evolution of porosity and mechanical coordination number, the physical meaning of which are the same in both axisymmetric compression and plane strain, the difficulty does not arise.

7.3 Comparison of drained axisymmetric compression and drained plane strain simulations

The comparison includes both macroscopic and microscopic behaviour. The macroscopic behaviour includes the evolution of deviator stress ($\sigma_1 - \sigma_3$), q_{dev}, sin φ, and porosity; the microscopic behaviour includes the evolution of mechanical coordination number, deviator fabric and a new fabric parameter (see the definition in section 7.3.8). The sample with a porosity of 0.362 is denoted as porosity0.362 or sample0.362 in the discussion for convenience, similarly for other samples. In the following discussion, only the densest and loosest samples are superimposed on one graph for a given parameter's evolution. The complete seperate set of graphs for each of the eight samples are provided in Appendix B.

7.3.1 Evolution of deviator stress

Figure 7.1 shows the evolution of deviator stress (q) against deviatoric strain (ε_{dev}) under both DAC and DPS conditions for the densest and loosest samples. The separate sets of evolution of q for all the samples are provided in Appendix B (Fig. B.1a-h). These plots show that the evolution of q at very small strains is quite independent of the strain conditions for a given sample. It can seen that q_{peak} (q at peak) and q_{cs} (q at critical state) are higher in DPS than those in DAC for a given sample, but for the densest sample the differences are very small. The deviator stress can be considered to be a "mobilised" strength parameter. In terms of shear strength, the series of evolutions of q for the densest sample suggest that the extended Tresca failure criterion ($q/p = M$, M is a constant for a given sample) might be an appropriate strength criterion for both peak and critical state failure states. For the other samples, the shear strength in terms of deviator stress is higher in DPS than in DAC, for both peak and critical state failure states.

7.3.2 Evolution of deviatoric stress

Figure 7.2 shows the evolution of deviatoric stress (q_{dev}) against deviatoric strain (ε_{dev}) under both DAC and DPS conditions for the densest and loosest samples. The separate sets of evolution of q_{dev} for all the samples are provided in Appendix B (Fig. B.2a-h). It can seen that q_{dev} at peak and at critical state are respectively lower in DPS than those in DAC for a given sample. In terms of shear strength, the series of evolutions of q_{dev} suggest that the extended Mises failure criterion ($q_{dev}/p = M$, M is a constant for a given sample) is not appropriate, which is true for both peak and critical state failure states.

7.3.3 Evolution of sin φ

Figure 7.3 shows the evolution of sin φ against ε_{dev} under both DAC and DPS conditions for the densest and loosest samples. The separate sets of evolution of sin φ for all the samples are provided in Appendix B (Fig. B.3a-h). It can be seen that sin φ at peak and at critical state are respectively higher in DPS than those in DAC for a given sample. In terms of shear strength, the series of evolutions of sin φ suggest that the Mohr-Coulomb failure criterion is not an appropriate strength criterion, which is true for both peak and critical state failure states.

7.3.4 Evolution of Lade's parameter

Lade and Duncan (1975) proposed a new failure criterion (subsequently referred to as the Lade criterion):

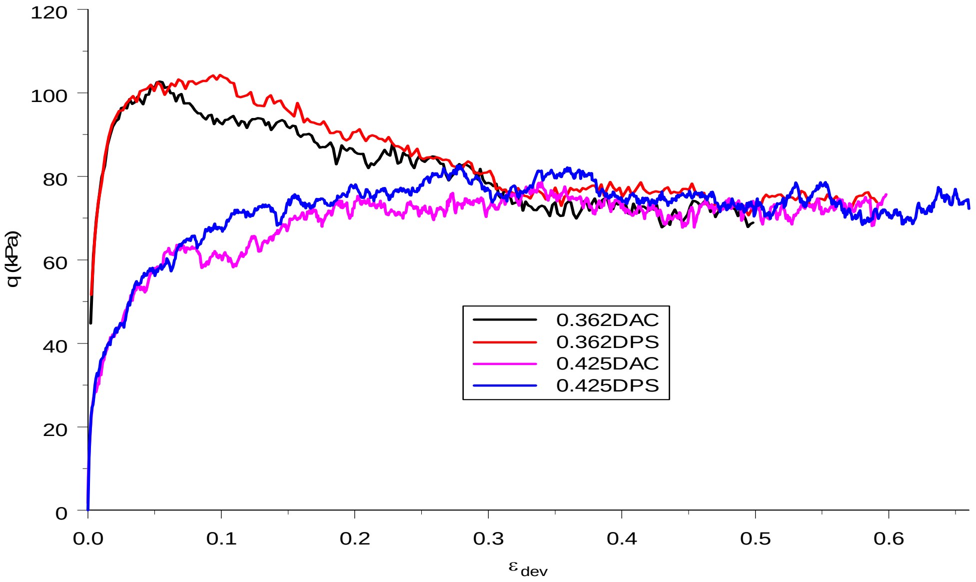

Fig. 7.1 Evolution of deviator stress
[key refers to porosity]

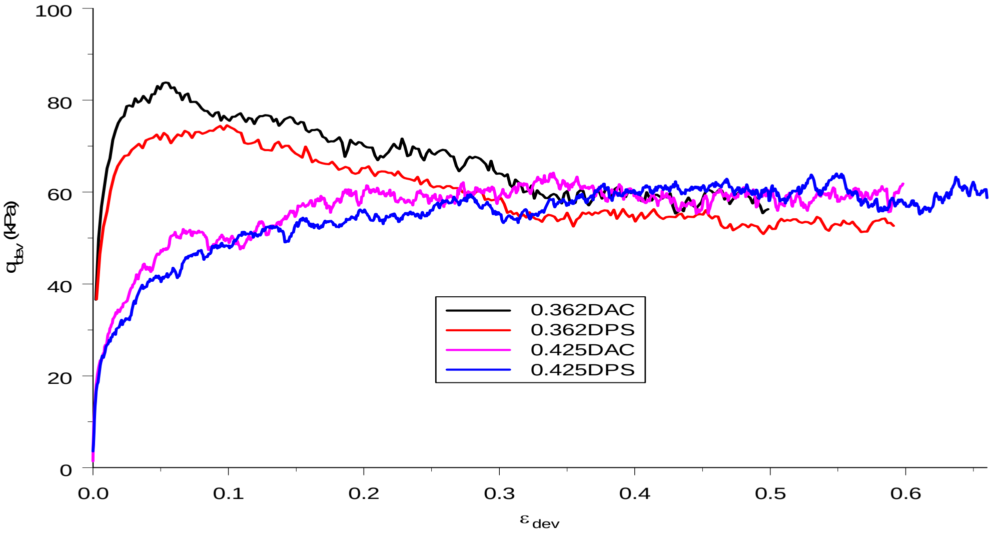

Fig. 7.2 Evolution of deviatoric stress
[key refers to porosity]

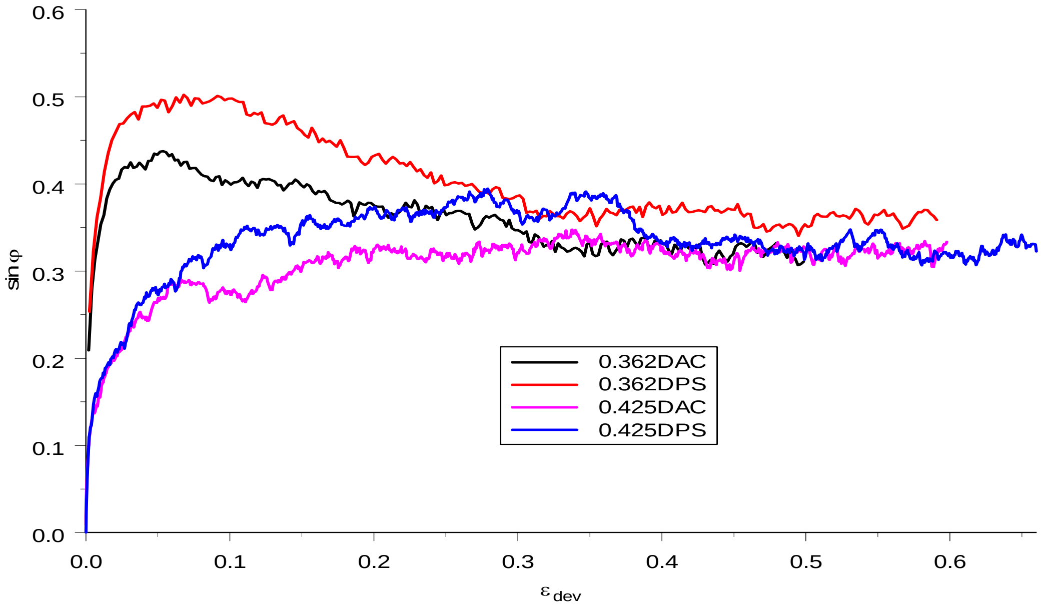

Fig. 7.3 Evolution of sin φ
[key refers to porosity]

$$\eta = \frac{I_1^3}{I_3} - 27 \tag{7.5}$$

where I_1 and I_3 are the first and the third stress invariants respectively.

Figure 7.4 shows the evolutions of the Lade parameter (η) against ε_{dev} under both DAC and DPS conditions for the densest and loosest samples. The separate sets of evolution of η for all the samples are provided in Appendix B (Fig. B.4a-h). It can seen from the figure that η at peak and at critical state are respectively independent of strain conditions (DPS and DAC) for a given sample. In terms of shear strength, the series of evolutions of

η suggest the Lade failure criterion is an appropriate strength criterion, which is true for both peak and critical state failure states. An extra interesting point about η is that, for a given initial porosity, its evolution against ε_{dev} is approximately independent of the strain conditions, which was first reported by Thornton (2000).

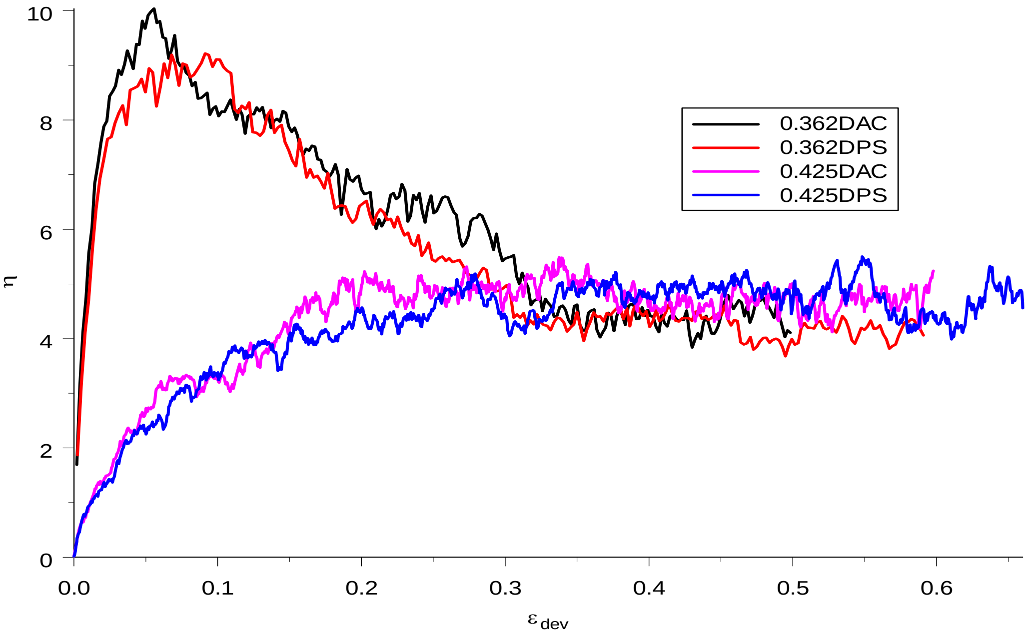

Fig. 7.4 Evolution of the Lade parameter
[key refers to porosity]

7.3.5 A summary of the different shear strength criteria

The extended Tresca, extended Mises, Mohr-Coulomb, and Lade failure criteria (all these criteria can be described by hyperplanes in stress space) can be viewed on a deviatoric plane (sometimes called the Π plane), see Fig. 7.5. The different failure hyperplanes form bounded surfaces in stress space, and when projected on the deviatoric stress plane, the different failure surfaces form a series of contours (also bounded). In Fig. 7.5, only one series of contours (all different failure surfaces have the same common point at the axisymmetric compression stress state) is plotted including the Matsuoka-Nakai surface and some experimental data from Lade and Duncan (1973, 1975). For the simulations performed in Chapter 3 and Chapter 4, there are only two points (e.g. peak states) in the deviatoric plane for a given sample. All the simulations were performed under constant mean stress conditions, and therefore the stress path is a curved (or straight) line on this deviatoric plane. The stress path for DAC is a line along the σ_x (in Fig. 7.5) axis, and the stress path for DPS is a curved line from the origin of the deviatoric plane. It should be mentioned that the Lade failure criterion was proposed mainly based on the experimental data for dense sand, and for loose sand there is some small deviation as pointed out by Lade and Duncan (1975). But for the DEM simulation data reported for DAC and DPS, the Lade failure criterion seems to give the best overall data-fit.

From Fig. 7.5, the extended Tresca and Lade failure surfaces are very close to each other for the sub-regions between axisymmetric compression and plane strain noting the value of b stress for plane strain at peak stress states is usually between 0.3 and 0.4. This is in agreement with the discussion in section 7.3.1 and therefore the extended Tresca failure criterion seems to give a good agreement for the reported data: both the physical experiment of Lade and Duncan (1973) and the DEM simulation data, for the dense sample, which also agrees with observations of Bishop (1966). For the loose samples, the extended Tresca criterion does not fit the reported data, as was implied by Bishop (1966) and was confirmed by the DEM simulation data reported in this thesis. Although the Matsuoka-Nakai failure criteria is also close to the Lade criterion for the sub-region between axisymmetric compression and plane strain, it does not fit the data for axisymmetric extension simulation data as reported by Thornton (2000), and therefore Matsuoka-Nakai criterion is not discussed further.

Also, from Fig. 7.5, the Mohr-Coulomb and the extended Mises surfaces deviate from the Lade surface for the sub-region between axisymmetric compression and plane strain. As can be seen in Fig. 7.5 for the discrete experimental data, sin φ will be expected to be smaller in axisymmetric compression than in plane strain, and q_{dev} will be expected to be larger in axisymmetric compression than in plane strain. These observations are again in agreement with the DEM simulation data reported here, which is another indication that the Lade criterion gives the best data-fit.

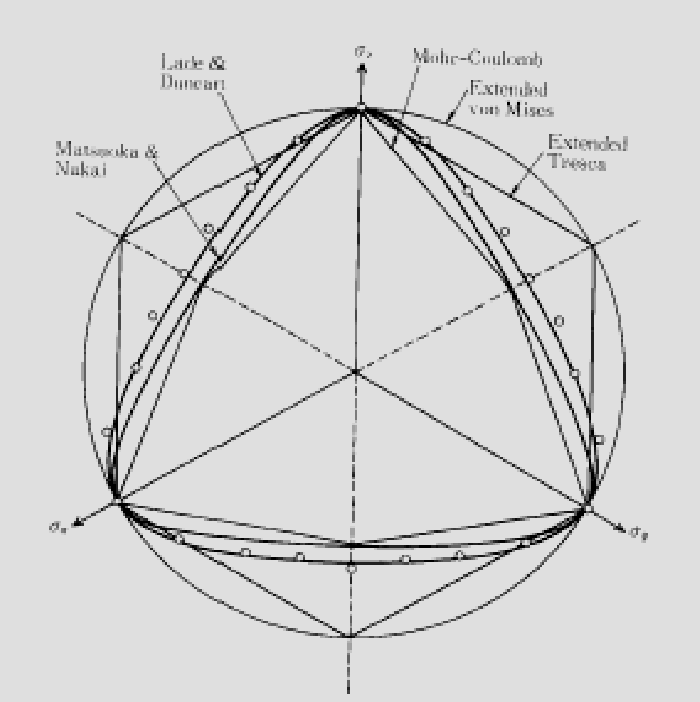

Fig. 7.5 Different failure criteria on the deviatoric plane [after Koseki (2005)]

7.3.6 Evolution of porosity

Figure 7.6 shows the evolution of porosity against ε_{dev} under both DAC and DPS conditions for the densest and loosest samples. The separate sets of evolution of porosity for all the samples are provided in Appendix B (Fig. B.5a-h). It can seen that porosity before critical state is nearly independent of strain conditions (DPS and DAC) for the densest sample. For all the loose samples, the plane strain condition seems to provide a higher resistance to volume contraction than axisymmetric compression during shear. The critical porosity is found to depend upon both the strain conditions and the initial porosities, but from a practical point of view the critical porosity can be considered to be independent of these conditions since the deviation is small.

7.3.7 Evolution of deviator fabric

Figure 7.7 shows the evolution of deviator fabric ($\phi_1-\phi_3$) against ε_{dev} under both DAC and DPS conditions for the densest and loosest samples. The separate sets of evolution of ($\phi_1-\phi_3$) for all the samples are provided in Appendix B (Fig. B. 6a-h). It can seen that ($\phi_1-\phi_3$) for DPS is correspondingly higher than that for DAC for a given sample during shear.

7.3.8 Evolution of the generalised fabric parameter

Following Thornton (2000), the failure fabric envelope in deviatoric fabric space has the shape of an “inverted Lade surface” for constant mean stress simulations. Therefore, a fabric parameter can be defined as

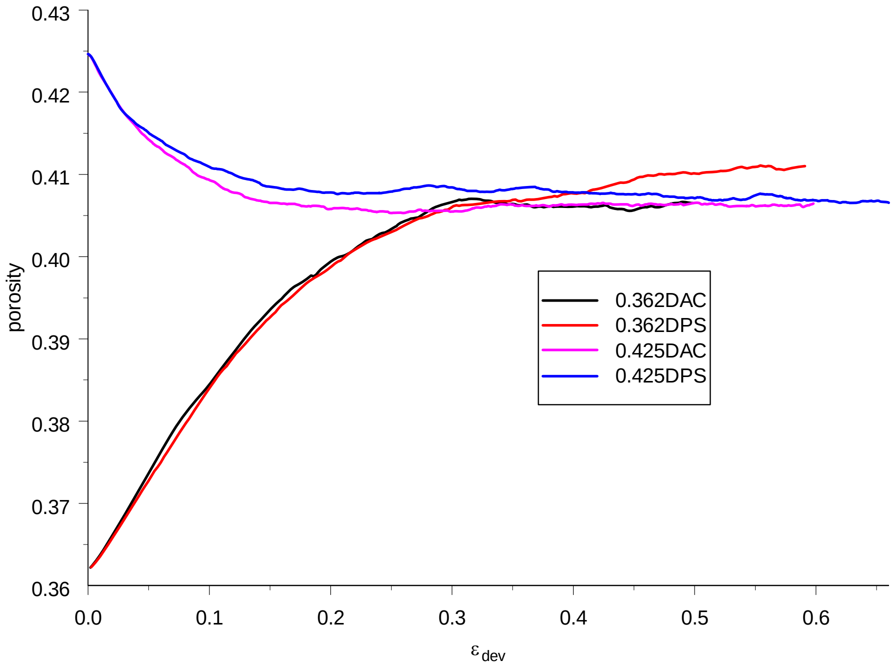

Fig. 7.6 Evolution of porosity
[key refers to porosity]

$$\eta^{\phi} = \frac{1}{2I_2^{\phi} - 3I_3^{\phi}} \tag{7.6}$$

where I_2^{ϕ} and I_3^{ϕ} are the second and third invariants of the fabric tensor respectively. For an isotropic structure, I_2^{ϕ} = 1/3 and I_3^{ϕ} = 1/27, therefore η^{ϕ} = 1.8.

Figure 7.8 shows the evolution of η^{ϕ} against ε_{dev} under both DAC and DPS conditions for the densest and loosest samples. The separate sets of evolution of η^{ϕ} for all the samples are provided in Appendix B (Fig. B. 7a-h). The figure shows that for a given initial sample, the evolution of the generalised fabric parameter (η^{ϕ}) is independent of the strain conditions. It can also be seen that ‘strain hardening and softening’ can be observed in terms of this parameter.

7.3.9 Evolution of mechanical coordination number

Figure 7.9 shows the evolution of Z_m against ε_{dev} under both DAC and DPS conditions for the densest and loosest samples. The separate sets of evolution of Z_m for all the samples are provided in Appendix B (Fig. B. 8a-h). It can be seen that the evolution of Z_m is essentially independent of strain conditions for a given sample in constant mean stress tests.

7.4 Comparison of undrained axisymmetric compression and undrained plane strain simulations

In this section, comparison of undrained axisymmetric compression (UAC) and undrained plane strain (UPS) simulations will be discussed. The comparison is focused on the undrained stress path, the evolution of sin φ and the evolution of the mechanical coordination number.

7.4.1 Undrained stress path

Figure 7.10 shows the undrained stress paths (deviator stress plotted against mean stress) for all the loose systems under UAC and UPS. It can be seen from the figure that the undrained stress paths are quite dependent on strain conditions. The system exhibits a higher resistance to liquefaction (or temporary liquefaction) in UPS than in UAC. For

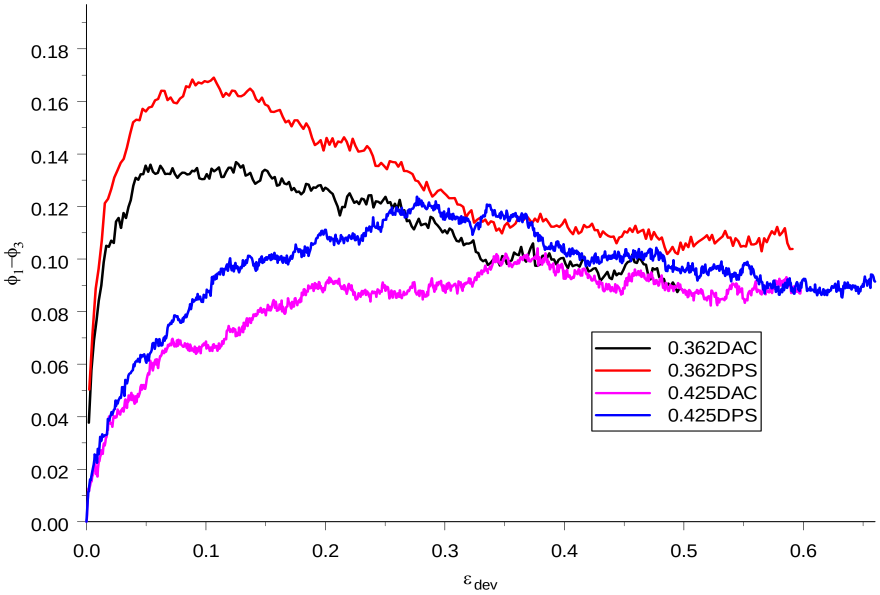

Fig. 7.7 Evolution of deviator fabric
[key refers to porosity]

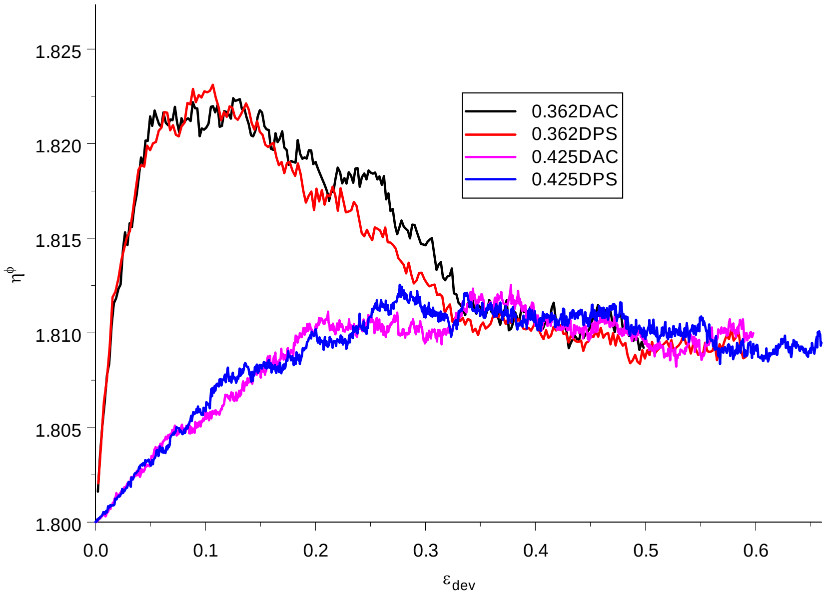

Fig. 7.8 Evolution of η^{ϕ}
[key refers to porosity]

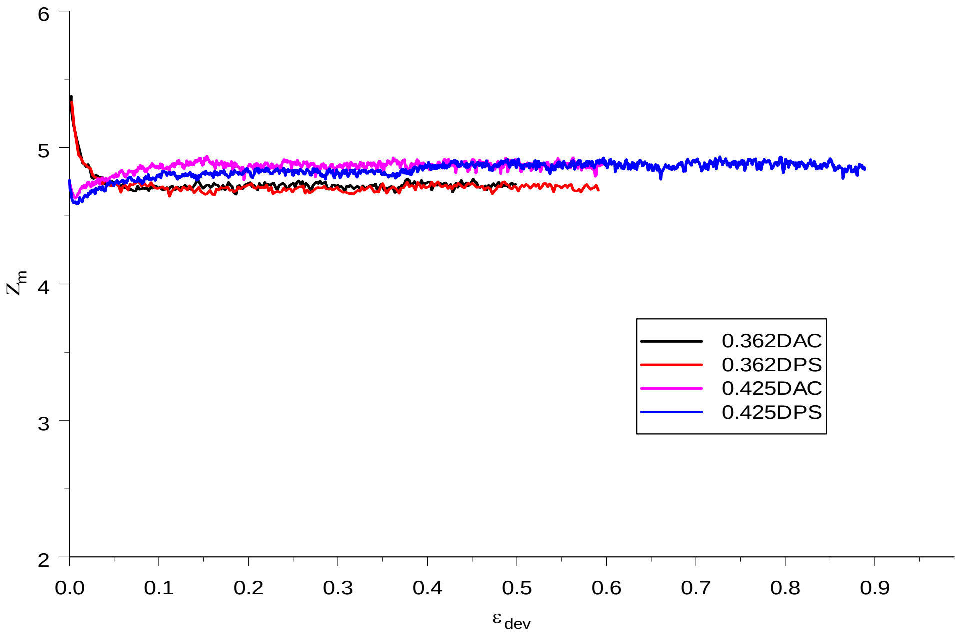

Fig. 7.9 Evolution of mechanical coordination number
[key refers to porosity]

each of the three medium loose systems, the values of the initial peak of q and p in UPS, are correspondingly higher than those in UAC, and the quasi-steady state values of q and p are also correspondingly higher in UPS.

7.4.2 Evolution of sin φ

Figure 7.11 shows the evolution of sin φ for all the systems (including the two dense systems) under UAC and UPS. The figure shows that, for all samples, the value of sin φ is always greater in UPS than in UAC. This is consistent with Lee (1970) who reported higher values of peak sin φ for UPS than for UAC.

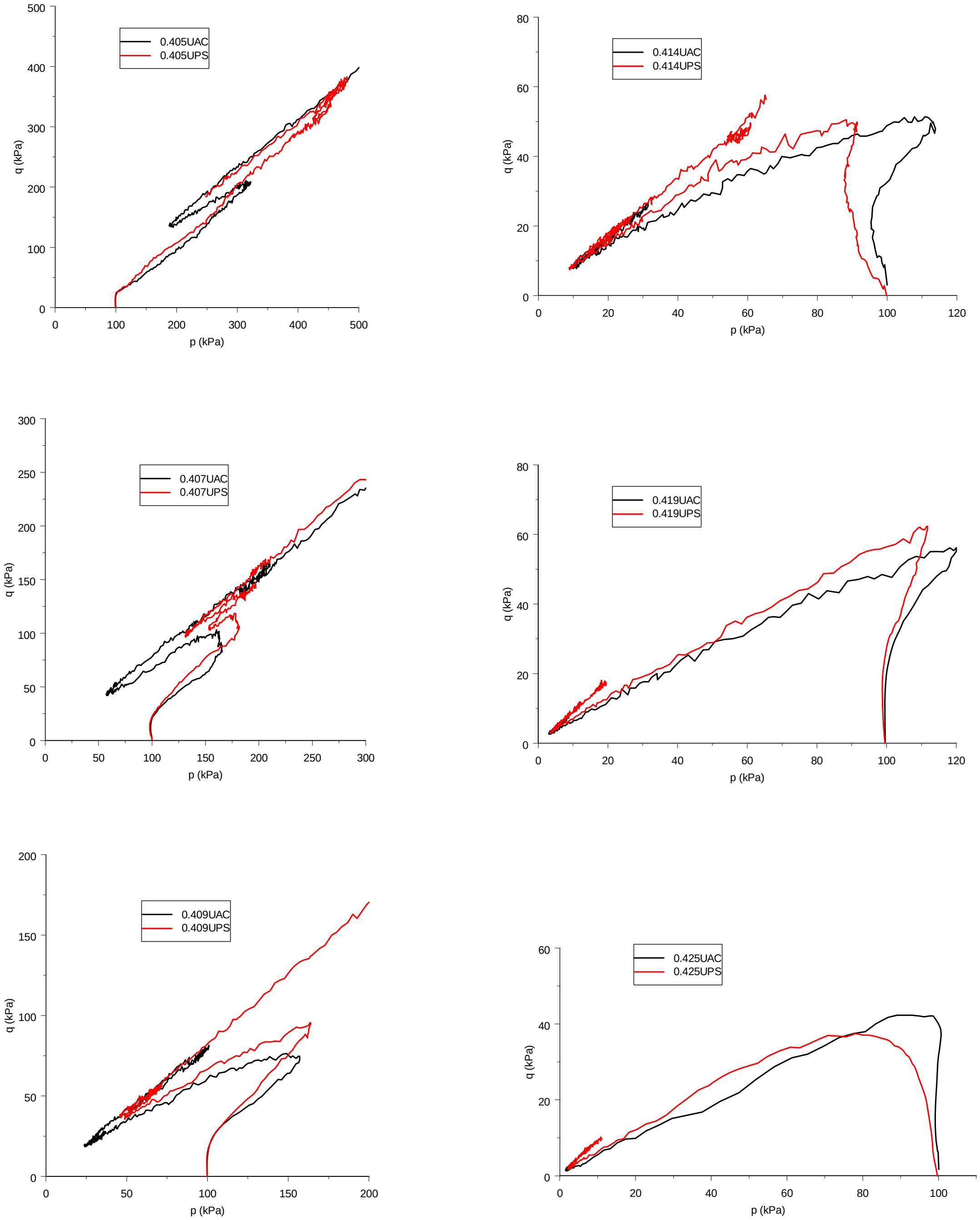

Fig. 7.10 Undrained stress paths for all loose systems
[key refers to porosity]

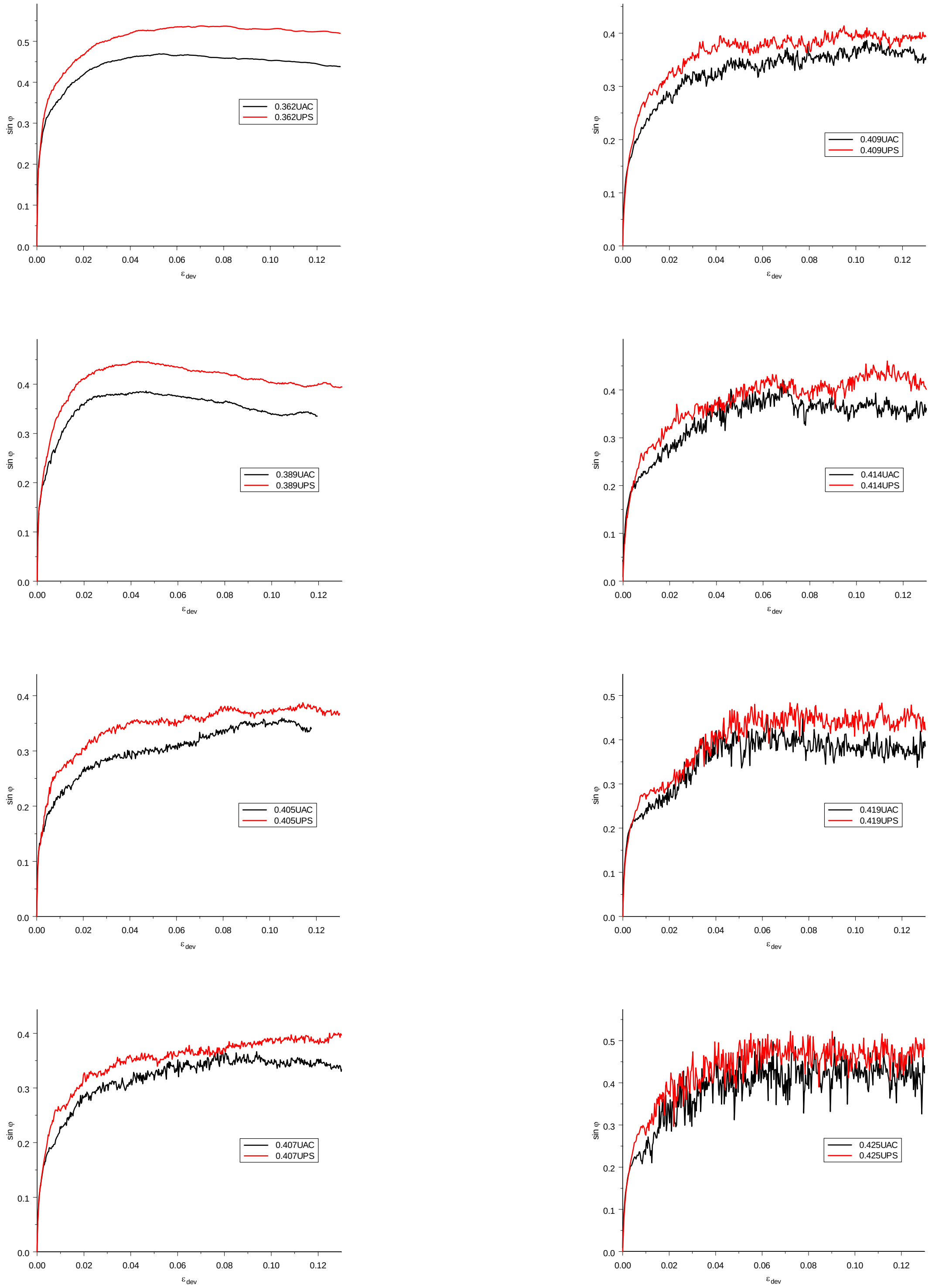

Fig. 7.11 Evolutions of sin φ for all systems
[key refers to porosity]

Table 7.1 shows the peak values of sin φ for all the systems for both drained and undrained conditions. It can be seen from the table that sinφ_{peak} generally depends on both drained conditions and strain conditions.

Table 7.1 Peak values of sin φ in drained and undrained simulations

samples	sinφ_{peak} in DAC	sinφ_{peak} in DPS	sinφ_{peak} in UAC	sinφ_{peak} in UPS
porosity0.362	0.44	0.50	0.47	0.54
porosity0.389	0.36	0.42	0.38	0.45
porosity0.405	0.35	0.40	0.36	0.38
porosity0.407	0.35	0.39	0.37	0.39
porosity0.409	0.35	0.39	0.36	0.40
porosity0.414	0.35	0.39	0.40	0.45
porosity0.419	0.34	0.38	0.42	0.46
porosity0.425	0.34	0.39	0.47	0.52

7.4.3 Evolution of mechanical coordination number

Figure 7.12 shows the evolution of mechanical coordination number (Z_m) for all loose systems under UAC and UPS. The figure shows that Z_m under UPS is a little higher than that under UAC. This means a loose sample under UAC conditions will be expected to reach the limiting value of $Z_m = 4$ at a smaller deviatoric strain than under UPS, and therefore a loose system under UPS exhibits higher resistance to instability.

7.5 Summary

This chapter presents a comparison of DAC and DPS as well as UAC and UPS behaviour. It is found that the Lade failure criterion gives the best overall data-fit for all the samples under drained conditions, and is independent of strain conditions. It is also found that a

Fig. 7.12 Evolutions of mechanical coordination number for all loose systems
[key refers to porosity]

generalised fabric parameter (η^{ϕ}) is independent of strain conditions under drained conditions. In undrained conditions, a loose system is found to exhibit higher resistance to instability in UPS than in UAC in terms of both stresses and mechanical coordination number.

CHAPTER 8: CONCLUSIONS AND SUGGESTIONS FOR FUTURE WORK

Drained and undrained simulation results have been reported, both under axisymmetric compression and plane strain conditions. A range of eight samples from very dense to very loose have been generated, and four simulations: drained axisymmetric compression (Chapter 3), drained plane strain (Chapter 4), undrained axisymmetric compression (Chapter 5) and undrained plane strain (Chapter 6) were performed for each sample but only results of the loose samples are presented for all undrained simulations in this thesis. The research work presented in this thesis shows that DEM can qualitatively capture fundamental behaviour under both drained and undrained conditions. Such a systematic investigation of the drained and undrained behaviour using DEM has never been reported in the literature before.

In this chapter, the conclusions related to the simulation results will be briefly summarised with further comments on the limitations of DEM and possible future work.

8.1 Conclusions

8.1.1 Summary of the conclusions for the main chapters

The results reported in Chapter 3 capture the general qualitative drained axisymmetric compression behaviour. Strain softening is only observed for dense samples, while strain hardening is observed for samples of all initial densities. A unique critical state in (q, p, e) space is observed independent of initial density, which means that there is a unique stress ratio and a unique porosity at the critical state. When critical state is reached, all microscopic state variables (parameters) remain almost constant.

The results reported in Chapter 4 capture the general qualitative drained plane strain behaviour. As in the axisymmetric compression simulations, strain softening is only observed for dense samples and strain hardening is observed for all samples. An approximately unique critical state is observed independent of initial density but dependent on the strain conditions. A unique porosity (or void ratio) at the critical state was found to be independent of strain conditions. When critical state is reached, all microscopic state variables (parameters) remain constant.

The results reported in Chapter 5 capture general qualitative undrained axisymmetric compression behaviour. The steady state (and quasi-steady state), liquefaction and instability concepts are redefined in terms of the mechanical coordination number. It was found that the limiting mechanical coordination number corresponds to the start of mechanical instability of the system. The preshear process was found to decrease the porosity, thus explaining the higher resistance to liquefaction. An ultimate state in q-p space was found to be curved but can be taken to be approximately linear (with a slope of M) for all the undrained simulations on loose samples and M is independent of porosity and preshear history. The undrained behaviour was found to be strain rate and stress history dependent.

The results of undrained plane strain simulations were presented in Chapter 6. The results extended the findings in Chapter 5 on the phase transition in terms of the limiting mechanical coordination number. It was demonstrated that the strain condition is an important factor influencing the undrained behaviour especially with regard to the resistance to liquefaction.

In Chapter 7 the results of the axisymmetric compression and plane strain simulations, both drained and undrained, were compared. It was found that the Lade failure criterion gave the best overall data-fit under drained conditions and is independent of strain conditions. It was also found that a generalised fabric parameter (η^{ϕ}) is independent of strain conditions under drained conditions. In the undrained simulations, loose systems were found to exhibit higher resistance to instability in plane strain than in axisymmetric compression in terms of both stresses and mechanical coordination number.

8.1.2 Summary of the main conclusions for the whole thesis

The summary of the conclusions for the whole thesis is as follows:

- Under drained axisymmetric compression conditions, dense samples dilate and loose samples contract. All the samples reach a unique critical state (with a critical porosity of 0.407) at large deviator strains of over 60%. (See section 3.4)

- Under drained conditions (by comparing axisymmetric compression and plane strain conditions), the Lade failure criterion is the most appropriate one for describing both peak and critical state failures. (See section 7.3)

- Under undrained conditions, liquefaction and temporary liquefaction can be observed for very loose and medium loose samples respectively. Liquefaction as well as temporary liquefaction can be explained by the loss of contacts and the appearance of structural mechanism. A criterion is proposed to justify when liquefaction or temporary liquefaction occurs in terms of mechanical coordination number Z_m, i.e. when $Z_m < 4$, liquefaction or temporary liquefaction occurs (See section 5.4). The preshearing process was found to decrease the porosity, thus providing the higher resistance to liquefaction compared the one without preshearing. In addition, the initial stress path for the presheared samples all lie on a unique curved line independent of the preshearing stress values (See section 5.5). Undrained behaviour was found to depend on the strain rates imposed, and the higher strain rates provide higher resistance to liquefaction (See section 5.6).

- Under undrained conditions, loose samples under plane strain condition give higher resistance to liquefaction (temporary liquefaction) than axisymmetric compression. (See section 7.4)

The above conclusions fulfil the objectives of this thesis (See section 1.2).

8.2 Limitations of DEM and future work

DEM has been widely used in particle technology and minerals engineering. In civil engineering it has been limited to examining the fundamental aspect of the mechanics of granular materials such as sand. In the context of geotechnical engineering problems, the big constraint is the number of particles required but parallel computing may make it possible to examine such problems in the future. However, this is complicated by the fact that density scaling, as used in the simulations in this thesis, cannot be used in a situation where gravity is included. Consequently, since geotechnical engineering is usually concerned with quasi-static problems, even with parallel codes any simulation will take a lot of computer time.

In the context of periodic cell simulations there are still problems that need to be addressed. An important issue is the effect of the particle size distribution. All DEM simulations that have been reported have used a rather narrow particle size distribution corresponding to what, in experimental terms, would be regarded as uniformly graded samples. With the potential offered by parallel computing, and therefore the total number of particles used in a simulation, it will be possible in the near future to examine the mechanical behaviour of well-graded systems and, in particular, gap-graded systems. It is not clear whether the information obtained from simulations of uniformly graded systems will also apply to such more realistic granular material.

The research work presented in this thesis is only a first attempt to investigate the drained and undrained behaviour of granular material in a systematic way. However, it should be noted the use of spherical particles has its limitations (see Chapter 2). The future work related to this thesis could include:

- To perform drained extension and other general 3D simulations for all the samples with a range of porosities in order to confirm whether the Lade's failure criterion is indeed the most appropriate one to be used to describe the results.

- To generate a series of samples with a range of porosities under different confining pressures (without considering particle crushing) and perform drained simulations for all the samples in order to study the validity of the state parameter as proposed by Been and Jefferies (1985).

- To implement bonded particle shapes in the TRUBAL code, in which simple particle crushing can be modelled, and study their drained and undrained behaviour.

- To generate other particle systems with more realistic size distributions.

- To compare the drained and undrained simulations using wall boundaries and using a periodic cell.

REFERENCES

Alarcon-Guzman, A., Leonards, G.A., and Chameau, J.L. (1988). Undrained monotonic and cyclic strength of sand. Journal of Geotechnical Engineering, ASCE, **114**(10), 1089-1109.

Alshibli, K. A., Bastiste, S. N., and Sture, S. (2003). Strain localization in sand: plane strain versus triaxial compression. Journal of Geotech. and Geoenvir. Engrg.,ASCE, **129**(6), 483-494.

Ashour, M. and Norris, G. (1999). Liquefaction and undrained response evaluation of sands from drained formulation. Journal of the geotechnical and geoenvironmental engineering division, ASCE, **125**(8), 649-658.

Atkinson, J. H. and Bransby, P. L. (1978). The Mechanics of Soils: An Introduction to Critical State Soil Mechanics. McGraw-Hill, New York.

Bagi, K. (1993). A quasi-static numerical model for micro-level analysis of granular assemblies. Mechanics of Materials, **16**, 101-110.

Bagi, K. (1996). Stress and strain in granular assemblies. Mechanics of Materials, **22**, 165-177.

Bagi, K. (2006). Analysis of microstructural strain tensors for granular assemblies. International Journal of Solids and Structures, **43,** 3166-3184.

Bardet, J. P. (1994). Observations on the effects of particle rotations on the failure of idealized granular materials. Mechanics of Materials, **18**, 159-182

Bardet, J. P. (1997). Experimental Soil Mechanics. Prentice Hall, Upper Saddle River, New Jersey 07458.

Barden, L. and Khayatt, A.J. (1966). Incremental strain ratios and strength of sand in the triaxial test. Geotechnique, **16**(4), 338-357.

Barden, L., Ismail, H. and Tong, P. (1969). Plane strain deformation of granular material at low and high pressures. Geotechnique, **19**(4), 441-452.

Bathurst, R. J. and Rothenburg, L. (1990). Observations on stress-force-fabric relationships in idealized granular materials. Mechanics of Materials, **9** , 65-80.

Been, K., Jefferies. (1985). A state parameter for sands. Geotechnique, **35**(2), 99-112.

Been, K., Jefferies, M. G. and Hachey, J. (1991). The critical state of sands. Geotechnique, **41**(3), 365-181.

Bishop, A. W. (1966). The strength of soils as engineering materials. Sixth Rankine Lecture, Geotechnique, **16**(2), 89-130.

Bishop, A. W. (1971). Shear strength parameters for undisturbed and remoulded soil specimens. Stress-strain behaviour of soils. Proc. Roscoe Memorial Symp., Cambridge, 3-58.

Bishop, A.W. and Eldin, A. K. G. (1950). Undrained triaxial tests on saturated sands and their significance in the general theory of shear strength. Geotechnique, **2**, 13-32.

Bishop, A.W. and Eldin, A. K. G. (1953). The effect of stress history on the relation between j and porosity of sand. Proc. 3rd international conference on soil mechanics and foundation engineering, Zurich, Switzerland, **1**, 100-105.

Bishop, A. W. and Henkel, D. J. (1957). The measurement of soil properties in the triaxial test. Edward Arnold , London.

Bolton, M. D. (1986). The strength and dilatancy of sands. Geotechnique, **36**(1), 65-78.

Bonilla, R.R.O. (2004). Numerical simulations of undrained granular media. PhD thesis, University of Waterloo.

Bray, J. W. (1987). Boundary element and linked methods for underground excavation design. Analytical and Computational Methods in Engineering Rock Mechanics, Brown (ed.), Allen & Unwin, London, 164-202

Cambou, B. (1993). From global to local variables in granular materials. Powers & Grains 93 , Thornton (ed.), Balkema, Rotterdam, 73-86.

Castro, G. (1969). Liquefaction of sands. Soil Mechanics Series No. 81, Harvard Univ., Cambridge, Mass.

Chang, C. S. (1988). Micromechanical modelling of constitutive equation for granular material. Micromechanics of granular materials, Satake and Jenkins (eds), Elsevier Science Publishers, Amsterdam, Netherlands, 271-278.

Cheng, Y. P., Nakata, Y. and Bolton, M. D. (2003). Discrete element simulation of crushable soil. Geotechnique, **53**(7), 633-641.

Cheng, Y. P., Bolton, M. D. and Nakata, Y. (2004). Crushing and plastic deformation of soils simulated using DEM. Geotechnique, **54**(2), 131-141.

Christoffersen, J., Mehrabadi, M. M. and Nemat-Nasser, S. (1981). A micromechanical description of granular material behavior. Journal of Applied Mechanics, **48**, 339-344.

Chu, J. (1992). Discussion “ The critical state of sands”. Geotechnique, **42**(4), 655.

Chu, J. and Leong, W. K. (2001). Pre-failure strain softening and pre-failure instability of sand : a comparative study. Geotechnique, **51**(4), 311-321.

Coop (1990). The mechanics of uncemented carbonate sands. Geotechnique, **40**(4), 607-626.

Coop and Atkinson (1993). The mechanics of cemented carbonate sands. Geotechnique, **43**(1), 53-67.

Cornforth, D.H. (1961). Plane strain failure characteristics of saturated sand. PhD thesis, University of London.

Cornforth, D. H. (1964). Some experiments on the influence of strain conditions on the strength of sand. Geotechnique, **14**(2), 143-167.

Cuccovillo and Coop (1999). On the mechanics of structured sands. Geotechnique, **49**(6), 741-760.

Cui, L. and O'Sullivian, C. (2006). Exploring the macro- and micro-scale response of an idealised granular material in the direct shear apparatus. Geotechnique, **56**(7), 455-468.

Cundall, P. A. (1971). A computer model for simulating progressive, large-scale movements in blocky rock systems. Proc. Symp. Int. Soc. Rock Mech., Nancy, **2**, 132-

150.

Cundall, P. A. (1974). A computer model for rock-mass behaviour using interactive graphics for the input and output of geometrical data. Report for the Missouri River Division, U.S. Army Corps of Engineers, University of Minnesota.

Cundall, P. A. (1978). BALL-A computer program to model granular media using the distinct element method. Technical note TN-LN-13, Advance Technology Group, Dames and Moore, London.

Cundall, P. A. (1988). Computer simulations of dense sphere assemblies. Micromechanics of granular materials, Satake and Jenkins (eds), Elsevier Science Publishers, Amsterdam, Netherlands, 113-123.

Cundall, P. A. (2001). A discontinuous future for numerical modelling in geomechanics?. Proc. of the Institution of Civil Engineers, Geotechnical Engineering, **149**(1), 41 – 47.

Cundall, P. A. and Hart, R. D. (1992). Numerical modeling of discontinua. Engineering Computations, **9**, 101-113.

Cundall, P. A. and Strack, O. D. L.(1979a). The development of constitutive laws for soil using the distinct element method. Third International Conference on Numerical Methods in Geomechanics, Wittke (Eds), Balkema, Aachen, 289-298.

Cundall, P. A. and Strack, O. D. L.(1979b). A discrete numerical model for granular assemblies. Geotechnique, **29**(1), 47-65.

Cundall, P. A. and Strack, O. D. L.(1979c). The discrete element method as a tool for research in granular media. Part II. Report to National Science Foundation, Dept. of Civil & Mineral Engrg., University of Minnesota, Minneapolis, Minnesota.

Cundall, P. A. and Strack, O. D. L.(1983). Modeling of microscopic mechanisms in granular material. Micromechanics of granular materials: New Models and Constitutive Relations, Jenkins and Satake (Eds), Elsevier Science Publishers, Amsterdam, Netherlands, 137-149.

Cundall, P. A., Drescher, A. and Strack, O. D. L.(1982). Numerical experiments on granular assemblies; Measurements and observations. IUTAM Conference on Deformation and Failure of Granular Materials, Balkema Publishers, Delft, 355-370.

Dantu, P. (1957). A contribution to the mechanical and geometrical study of non-cohesion masses. Proc. 4th Int. Conf. on Soil Mechanics & Foundation Engineering, London, UK, 144-148.

De Groot. M. B. and Stoutjesdijk, T. P. (1997). Undrained stress path of loose sand predicted from dry tests. Can. Geotech. J., **34**, 131-138.

De Josselin de Jong, G. and Verruijt, A. (1969). Etude photo-elastique d'un empilement de disques. Cahiers du Groupe Francais de Rheologie, **2**(1), 73-86.

Deresiewicz, H. (1958a). Mechanics of granular matter. Advances in Applied Mechanics, **5**, 233-306.

Deresiewicz, H. (1958b). Stress-strain relations for a simple model of a granular medium. Journal of Applied Mechanics, **25**, 402-406.

Digby, P. J. (1981). The effective elastic moduli of porous granular rocks. Journal of Applied Mechanics, **48**, 803-808.

Doanh, T. and Ibraim, E. (2000). Minimum undrained strength of Hostun RF sand. Geotechnique, **50**(4), 2000, 377-392.

Doanh, T. and Ibraim, E and Matiotti, R. (1997). Undrained instability of very loose Hostun sand in triaxial compression and extension. Part 1: experimental observations. Mechanics of Cohensive-Frictional Materials, Vol.2, 47-70.

Dobry, R. and Ng, T.-T. (1992). Discrete modelling of stress-strain behaviour of granular media at small and large strains. Engineering Computations, **9**, 129-143.

Drescher, A. (1976). An experimental investigation of flow rules for granular materials using optically sensitive glass particles. Geotechnique, **26**(4), 591-601

Drescher, A. and De Josselin de Jong, G. (1972). Photoelastic verification of a mechanical model for the flow of a granular material. J. Mech. Phys. Solids, **20**, 337-351.

Duffy, J. (1959). A differential stress-strain relation for the hexagonal close packed array of elastic spheres. Journal of Applied Mechanics, **26**, 88-94.

Duffy, J. and Mindlin, R. D. (1957). Stress-strain relations and vibrations of a granular medium. Journal of Applied Mechanics, **24**, 585-593.

Dyson, S. (1970). The strength and deformational behaviour of a cohensionless soil under generalized stress condition. PhD thesis, Aston University, Birmingham.

Feda, J. (1982). Mechanics of particulate materials. Development in geotechnical engineering 30. Elsevier publisher, Amsterdam.

Finge, Z, Boucq, S. and Doanh, T. (2003). The effects of stress path history on the undrained behaviour of saturated loose sands. Proc. 3rd international symposium on deformation characteristics of geomaterials, Swets & Zeitlinger, Lisse, Lyon, France, 729-736.

Finno, R. J., Harris, W. W., Mooney, M. A. and Viggiani, G. (1997). Shear bands in plane strain compression of loose sand. Geotechnique, **47**(1), 149-165.

Fu, Y. R. (2005). Experimental quantification and DEM simulation of micro-macro behaviors of granular materials using X-Ray tomography imaging. PhD thesis, Louisiana State University, USA.

Fung, Y. C. and Tong, P. (2001). Classical and computational solid mechanics. World Scientific, New Jersey.

Gajo, A. and Piffer, L. (1999). The effects of preloading history on the undrained behaviour of saturated loose sand. Soils and Foundations, **39**(6), 43-54.

Georgiadis, K., Potts, D. M. and Zdravkovic, L. (2004). Modelling the shear strength of soils in the general stress space. Computers and Geotechnics, **31**, 357-364.

Green, G. E (1969). Strength and compressibility of granular materials under generalised strain conditions. PhD thesis, University of London.

Hakuno, M. and Tarumi, Y. (1988). A granular assembly simulation for the seismic liquefaction of sand. Proc. Of JSCE, No. 398/I-10, 129-138.

Han, C. and Vardoulakis, I. (1991). Plane-strain compression experiments on water-saturated fin-grained sand. Geotechnique, **41**(1), 49-78.

Harder, J. and Schwedes, J. (1985). The development of a true biaxial shear tester. Part. Charact.,**2**, 149-153.

Head, K. H. (1986). Manual of soil laboratory testing, Volume 3: effective stress tests. Pentech Press, London.

Hill, R. (1950). The mathematical theory of plasticity. Oxford University Press, Oxford.

Ishihara, K. (1993). Liquefaction and flow failure during earthquakes. Geotechnique, 43(3),351-415.

Ishihara, K., Tatsuoka, F. and Yasuda, S. (1975). Undrained deformation and liquefaction of sand under cyclic stresses, Soils and Foundations, **15**(1), 29-44.

Iwashita, K. and Oda, M. (1998). Rolling resistance at contacts in simulation of shear band development by DEM. Journal of Engineering Mechanics, ASCE, **124**(3), 285-292.

Jensen, R. P., Bosscher, P. J., Plesha, M. E. and Edil, T. B. (1999). DEM simulation of granular media-structure interface: effects of surface roughness and particle shape. Int. J. Numer. Anal. Meth. Geomech., **23**, 531-547.

Jiang, M. J., Leroueil, S. and Konard, J. M. (2004). Insight into shear strength functions of unsaturated granulates by DEM analysis. Computers and Geotechnics, **31**, 473-489.

Khan, A. S. and Huang, S. (1995). Continuum theory of plasticity. John Wiley & Sons, New York.

Kishino, Y. (1988). Disc model analysis of granular media. Micromechanics of granular materials, Satake and Jenkins (eds), Elsevier Science Publishers, Amsterdam, Netherlands, 143-152.

Kishino, Y. (1989). Computer analysis of dissipation mechanism in granular media. Powders and Grains, Biarez & Gourves (eds), Balkema, Rotterdam, 323-330.

Kishino, Y. (1990). Quasi-static simulation of liquefaction phenomena in granular materials. Proc. of the second international symposium for science on form, (ed: S..Ishizaka), Tokyo: KTK scientific publishers, 157-174.

Komodromos, P. I. and Williams, J. R. (2004). Dynamic simulation of multiple deformable bodies using combined discrete and finite element methods. Engineering Computations, **21**, 431-448.

Koseki (2005). Principles of soil mechanics. http://soil.iis.u-tokyo.ac.jp/Lecture.htm

Kruyt, N. P. and Rothenburg, L. (1996). Micromechanical definition of the strain tensor of granular materials. Journal of Applied Mechanics, **118**, 706-711.

Lade, P. V. (1977). Elasto-plastic stress-strain theory for cohesionless soil with curved yield surfaces. International Journal of Solids and Structures, **13**, 1019-1035.

Lade, P. V. (1992). Static instability and liquefaction of loose fine sandy slopes. Journal of the geotechnical engineering division, ASCE, **118**(1), 51-71.

Lade, P. V. and Duncan, J. M. (1973). Cubical triaxial tests on cohesionless soil. Journal of the Soil Mechanics and Foundations Division, ASCE, Vol. 99, SM10, 793-812.

Lade, P. V. and Duncan, J. M. (1975). Elastoplastic stress-strain theory for cohensionless soil. Journal of Geotechnical Engineering Division, ASCE, Vol. 101, No. GT10, 1037-1053.

Lade, P. V. and Duncan, J. M. (1976). Stress-path dependent behaviour of cohensionless soil. Journal of Geotechnical Engineering Division, ASCE, Vol. 102, No. GT1, 51-68.

Lade, P. V. and Yamamuro, J. A. (1996). Undrained sand behaviour in axisymmetric tests at high pressures. Journal of the geotechnical engineering division, ASCE, **122**(2), 120-129.

Lade, P.V. and Bopp, P.A. (2005). Relative density effects on drained sand behaviour at high pressures. Soils and Foundations, **45**(1), 1-13.

Lambe, T. W. and Whitman, R. V. (1979). Soil Mechanics, SI Version. John Wiley & Sons, New York.

Lancelot, L., Shahrour, I. and Mahmoud, M. A. (2004). Instability and static liquefaction on proportional strain paths for sand at low stresses. Journal of Engineering Mechanics, ASCE, **130**(11), 1365-1372.

Lee, K. L. (1970). Comparison of plane strain and triaxial tests on sand. Journal of the Soil Mechanics and Foundations Division, ASCE, Vol. 96, SM3, 901-923.

Lee, K. L. and Seed, H. B. (1967). Drained strength characteristics of sands. Soil Mechanics and Foundations division, ASCE, SM6, 117-141.

Lin, X. and Ng, T.-T. (1997). A three-dimensional discrete element model using arrays of ellipsoids. Geotechnique, **47**(2), 319-329.

Malvern, L. (1969). Introduction to the mechanics of a continuous medium. Prentice-Hall, Inc., Englewood Cliffs, New Jersey.

Masson, S. and Martinez, J. (2001). Micromechanical analysis of the shear behaviour of a granular material. Journal of Engineering Mechanics, ASCE, **127**(10), 1007-1015.

Matsuoka, H. and Nakai, T. (1974). Stress-deformation relationship and strength characteristics of soil under three different principal stresses. Proc. Japan Soc. Civ. Engrs**,** **232**, 59-70.

Matsushima, T., Ishii, T. and Konagai, K. (2002). Observation of grain motion in the interior of a PSC test specimen by laser-aided tomography. Soils and Foundations. Vol. 42, No. 5, 27-36.

Meegoda, N. J. and Washington, D. W. (1994). Massively parallel computers for microscopic modeling of soils. Computer Methods and Advances in Geomechanics, Siriwardane and Zaman (eds.), Balkema, Rotterdam, 617-622.

Mehrabadi, M. M., Nemat-Nasser, S. and Oda, M. (1982). On statistical description of stress and fabric in granular materials. Int. J. Numer. Anal. Meth. Geomech., **6**, 95-108.

Mindlin, R. D. (1949). Compliance of elastic bodies in contact. Journal of Applied Mechanics, **16**, 259-268.

Mindlin, R. D. and Deresiewicz, H. (1953). Elastic spheres in contact under varying oblique forces. Journal of Applied Mechanics, **20**, 327-344.

Mirghasemi, A. A., Rothenburg, L. and Matyas, L. (2002). Influence of particle shape on engineering properties of assemblies of two-dimensional polygon-shaped particles. Geotechnique, **52**(3), 209-217.

Mooney, M. A., Finno, R. J. and Viggiani, M. G. (1998). A unique critical state for sand? Journal of Geotechnical and Geoenvironmental Engineering, ASCE, **124**(11), 1100-1108.

Muir Wood, D. (1990). Soil behaviour and critical state soil mechanics. Cambridge University Press, Cambridge.

Nakase ,H. (1999). A simulation study on liquefaction using DEM. An introduction Mechanics of Granular Materials , Oda and Iwashita (eds), 183-187.

Nemat-Nasser, S. and Mehrabadi, M. M. (1983). Stress and fabric in granular masses. Micromechanics of granular materials: New Models and Constitutive Relations, Jenkins and Satake (eds), Elsevier, 1-8.

Newland and Allely (1959). Volume change during undrained triaxial tests on saturated dilatant granular materials. Geotechnique, **9**(4), 174-182.

Ng, T.-T. (2001). Fabric evolution of ellipsoidal arrays with different particle shapes. Journal of Engineering Mechanics, ASCE, **127**(10), 994-999.

Ng, T.-T. (2002). Triaxial test simulations with discrete element method and hydrostatic boundaries. Journal of Engineering Mechanics, ASCE, **130**(10), 1188-1194.

Ng, T.-T. (2004a). Shear strength of assemblies of ellipsoidal particles. Geotechnique,

54(10), 659-669.

Ng, T.-T. (2004b). Macro- and micro-behaviors of granular materials under different sample preparation methods and stress paths. International Journal of Solids and Structures, **41**, 5871-5884.

Ng, T.-T. and Dobry, R. (1994). Numerical simulations of monotonic and cyclic loading of granular soil. Journal of Geotechnical Engineering, ASCE, **120**(2), 388-403.

Ng, T.-T. and Petrakis, E. (1996). Small-strain response of random arrays of spheres using discrete element method. Journal of Engineering Mechanics, ASCE, **122**(3), 239-244.

Norris, G., Siddharthan, R., Zafir, Z. and Madhu, R. (1997). Liquefaction and residual strength of sands from drained triaxial tests. Journal of Geotechnical Engineering, ASCE, **123**(3), 220-228.

Poulos, S. J. (1981). The steady state of deformation. Journal of the geotechnical engineering division, ASCE, **17**(5), 553-562.

O'Connor, R. M. (1996). A distributed distinct element modeling environment - algorithms, implementation and application. PhD thesis, Massachusetts Institute of Technology.

Oda, M. (1972). Initial fabrics and their relations to mechanical properties of granular material. Soils and Foundations, **12**(1), 17-36.

Oda, M. and Konishi, J. (1974). Microscopic deformation mechanism of granular material in simple shear. Soils and Foundations, **14**(4), 25-38.

Oda, M. (1978). Significance of fabric in granular mechanics. Proc. U.S. – Japan Seminar on Continuum-Mechanical and Statistical Approaches in the Mechanics of Granular Materials., Cowin and Satake (eds.), Tokyo, 7-26.

Oda, M. (1999). Fabric tensor and its geometrical meaning. An introduction: Mechanics of Granular Materials, Oda and Iwashita (eds.), Balkema, Rotterdam, 27-33.

Oda, M., Nemat-Nasser, S. and Mehrabadi, M. M. (1982). A statistical study of fabric in a random assembly of spherical granules. Int. J. Numer. Anal. Meth. Geomech., **6**, 77-94.

Oda, M., Tatsuoka, F. and Yoshida, T. (1997). Void ratio in shear band of dense granular soils (Does the critical void ratio exist in dense assemblies of granular soils?). Int. Symp. on Deformation and Progressive Failure in Geomechanics, (Asaoka et al., editors), Nagoya, 157-162.

Ogawa, S., Mitsui, S. and Takemure, O. (1974). Influence of the intermediate principal stress on mechanical properties of a sand. Proc. 29th Annual Meeting of JSCE, Part 3, 49-50

Onate, E. and Rojek, J. (2004). Combination of discrete element and finite element methods for dynamic analysis of geomechanics problems. Comput. Methods Appl. Mech. Engrg., **193**, 3087-3128.

Ouadfel, H. (1998). Numerical simulations of granular assemblies with three-dimensional ellipsoid-shaped particles. PhD thesis, University of Waterloo.

Powrie, W., Ni, Q, Harkness, R.M. and Zhang, X. (2005). Numerical modelling of plane strain tests on sands using a particulate approach. Geotechnique, **55**(4), 297-306.

Radjai, F., Jean, M., Moreau, J.-J. and Roux, S. (1996). Force distribution in dense two-dimensional granular systems. Physical Review Letters, **77**(2), 274-277.

Reades, D. W. (1972). Stress-strain characteristics of a sand under three-dimensional loading. PhD thesis, University of London.

Rothenburg, L. (1980). Micromechanics of idealized granular systems.PhD Dissertation, Carleton University, Ottawa, Ontario, Canada.

Rothenburg, L. and Selvadurai, A. P. S. (1981). A micromechanical definition of the Cauthy stress tensor for particulate media. Proc. Int. Symp. on the Mechanical Behaviour of Structured Media, Ottawa, Part B, 469-486.

Rothenburg, L., Bathurst, R. J. (1989). Analytical study of induced anisotropy in idealized granular materials. Geotechnique, **39**(4), 601-614.

Rothenburg, L. and Bathurst, R. J. (1992). Micromechanical features of granular assemblies with planar elliptical particles. Geotechnique, **42**(1), 79-95

Rothenburg, L. and Kruyt, N. P. (2004). Critical state and evolution of coordination number in simulated granular materials. International Journal of Solids and Structures, **41**, 5763-5774

Rothenburg, L., Bathurst, R. J. and Dusseault, M. B. (1989). Micromechanical ideas in constitutive modelling of granular materials. Powders and Grains, Biarez & Gourves (eds), 355-363.

Rowe, P. W. (1962). The stress-dilatancy relation for static equilibrium of an assembly of particles in contact. Proc. Roy. Soc. London A, **269**,500-527.

Rutledge, P. (1947). Cooperative triaxial shear research program. Progress report on soil mechanics fact finding survey, U.S. army Corps Of Engineers, Waterways Experiment Station, Vicksburg, Miss.

Sadd, M. H., Tai, Q. M. and Shukla, A. (1993). Contact law effects on wave propagation in particulate materials using distinct element modeling. Int. J. Non-Linear Mechanics, **28**(2), 251-265.

Sadd, M. H., Adhikari, G. and Cardoso, F. (2000). DEM simulation of wave propation in granular materials. Powder Technology, **109**, 222-233.

Satake, M. (1982). Fabric tensor in granular materials. IUTAM Conference on Deformation and Failure of Granular Materials, Balkema, Delft, 63-68.

Schofield, M. A., and Wroth, C. P. (1968). Critical State Soil Mechanics, McGraw-Hill, London.

Seed, H. B. and Lee, K. L. (1967). Undrained strength characteristic of cohensionless soils. Soil mechanics and foundations division, ASCE, 93, SM6, 333-361.

Serrano, A. A. and Rodriguez-Ortiz, J. M. (1973). A contribution to the mechanics of heterogeneous granular media. Proc. Symp. Plasticity and Soil Mech., Cambridge, 215-227.

Sitharam, T. G. (1999). Micromechanical modelling of granular materials: effect of confining pressure on mechanical behavior. Mechanics of Materials, **31**, 653-665.

Sitharam, T. G., Dinesh, S. V. and Shimizu, N. (2002). Micromechanical modelling of monotonic drained and undrained shear behaviour of granular media using three-dimensional DEM. Int. J. Numer. Anal. Meth. Geomech., **26**, 1167-1189.

Sladen, J. A. and Oswell, J. M. (1989). The behaviour of very loose sand in the triaxial compression test. Can. Geotech. J., **26**, 103-113.

Strack, O. D. L. and Cundall, P. A. (1978). The discrete element method as a tool for research in granular media. Part I. Report to National Science Foundation, NSF Grant ENG76-20711.

Strack, O. D. L. and Cundall, P. A. (1984). Fundamental studies of fabric in granular materials. Interim Report to NSFCEE–8310729, Dept. of Civil and Mineral Engineering, Univ. of Minnesota.

Tatsuoka, F., Pradhan, T.B.S. and Horii, N. (1988). Discussion on direct shear tests on reinforced sand. Geotechnique , **38** (1), 148-153.

Terzaghi, K. and Peck, R. B. (1967). Soil Mechanics in Engineering Practice. Wiley International Edition, John Wiley & Sons, Second Edition, New York.

Thornton, C. (1974). Deformation of sand in plane strain and axisymmetric compression. PhD thesis, Aston University, Birmingham.

Thornton, C. (1979). The conditions for failure of a face-centered cubic array of uniform rigid spheres. Geotechnique, **29**(4), 441-459.

Thornton, C. (1994). Micromechanics of elastic sphere assemblies during 3D shear. Proc. Workshop on Mechancis and Statistical Physics of Particulate Materials, Institute for Mechanics and Materials Report No. 94-9: 64-67. Univ. of California San Diego.

Thornton, C. (1997). Force transmission in granular media. KONA, **15**, 81-90.

Thornton (1999). Future developments in discrete element approaches. An introduction: Mechanics of Granular Materials, Oda and Iwashita (eds.), Balkema, Rotterdam, 217-219.

Thornton, C. (2000). Numerical simulations of deviatoric shear deformation of granular media. Geotechnique, **50**(1), 43-53.

Thornton, C. and Barnes, D. J. (1982). On the mechanics of granular material. IUTAM Conference on Deformation and Failure of Granular Materials, Delft, 69-77

Thornton, C. and Barnes, D. J. (1986a). Evolution of stress and structure in particulate material. Applied Solid Mechanics-1, Tooth and Spence (eds), Elsevier Applied Science Publishers, London and New York, 191-205

Thornton, C. and Barnes, D. J. (1986b). Computer simulated deformation of compact granular assemblies. Acta Mechanica, **64**, 45-61

Thornton, C. and Randall, C. W. (1988). Applications of theoretical contact mechanics to solid particle system simulation. Micromechanics of granular materials, Satake and Jenkins (eds), Elsevier Science Publishers, Amsterdam, Netherlands, 133-142

Thornton, C. and Sun, G. (1993). Axisymmetric compression of 3D polydisperse systems of spheres. Powers and Grains 93, Thornton (ed.), 129-134

Thornton, C. and Sun, G. (1994). Numerical simulation of general 3D quasi-static shear deformation of granular media. Numerical Methods in Geotechnical Engineering, Smith (ed.), Balkema, Rotterdam, 143-148.

Thornton, C. and Antony, S. J. (1998). Quasi-static deformation of particulate media. Proc. Roy. Soc. London A, **356**, 2763-2782.

Thornton, C. and Antony, S. J. (2000). Quasi-static shear deformation of a soft particle system. Powder Technology, **109**, 179-191.

Thornton, C. and Zhang, L. (2001). A DEM comparison of different shear testing devices. Powers and Grains 2001, Kishino (ed.), BALKEMA Publishers, Lisse, 183-190.

Thornton, C. and Zhang, L. (2003). Numerical simulations of direct shear test. Chem. Eng. Technol., **26**(2), 153-156.

Thornton, C. and Zhang, L. (2006a). Probing of the mechanical response of granular material in general 3D stress space. Geomechanics and Geotechnics of Particulate Media, Hyodo, Murata and Nakate (eds.), Yamaguchi, 199-204.

Thornton, C. and Zhang, L. (2006b). A numerical examination of shear banding and simple shear non-coaxial flow rules. Philosophical Magazine, **86**, 3425-3452.

Thornton, C. and Zhang, L. (2007). A numerical examination of the direct shear test. Geotechnique, in press.

Ting, J. M., Corkum, B. T., Kauffman, C. R., and Greco, C. (1989). Discrete numerical model for soil mechanics. Journal of Geotechnical Engineering, ASCE, **115**(3), 379-398.

Ting, J. M., Meachum, L. and Rowell, J.D. (1995). Effect of particle shape on the strength and deformation mechanism of ellipse-shaped granular assemblages. Engineering Computations, **12**, 99-108.

Tzaferopoulos, M. Ap. (1996). On a quasi-static discrete element model of granular materials. Computers and Geotechnics, **18**(2), 145-165.

Vaid, Y. P., Chung, E. K. F., Kuerbis, R. H. (1990). Stress path and steady state. Can. Geotech. J., **27**, 1-7.

Wade, N. H. (1963). Plane strain failure characteristics of saturated clay. PhD thesis, University of London.

Wakabayashi, T. (1957). Photoelastic method for determination of stress in powered mass. Proc. 7th Jap. Nat. Congr. Appl. Mech. 153-192.

Walton, K. (1987). The effective elastic moduli of a random packing of spheres. J. Mech. Phys. Solids, **35**, 213-226.

Wightman, A. (1967). The stess-dilatancy of sands during plane strain compression. PhD thesis, University of Manchester.

Wood, C. C. (1958). Shear strength and volume change characteristics of compacted soil under conditions of plane strain. PhD thesis, University of London.

Yamamuro, J. A. and Lade, P. V. (1996). Drained sand behaviour in axisymmetric tests at high pressures. Journal of the geotechnical engineering division, ASCE, **122**(2), 109-119.

Yamamuro, J. A. and Lade, P. V. (1997). Static liquefaction of very loose sands. Can.

Geotech. J., **34**, 905-917.

Yang, J. (2002). Non-uniqueness of flow liquefaction line for loose sand. Geotechnique, **52**(10), 757-760.

Zhang, H. M. and Garga, V. K. (1997). Quasi-steady state: a real behaviour? Can. Geotech. J., **34**(5), 749-761.

Zhang, L. (2003). The behaviour of granular material in pure shear, direct shear and simple shear. PhD thesis, Aston University, Birmingham, UK.

Zhang, L. and Thornton, C. (2007). Numerical probing of the mechanical response of granular material in general 3D stress/strain space. In-house report, Civil Engineering Department, University of Birmingham, UK.

APPENDIX A: SERVO-CONTROL MODE USED IN THE TRUBAL CODE

The TRUBAL code used for this thesis provides a servo-control option. The function of a servo-control mode is to permit any desired stress path to be followed approximately in incremental steps. With the servo-control mode, the applied strain field is continuously adjusted according to the difference between the desired stress state and the measured stress state. Depending on which servo-control mode is selected, the strain rates are adjusted differently. There are two servo-control modes used for this thesis, i.e. mode 1 and mode 2 in the code. Mode 1 is used for the isotropic compression in preparing the samples. Mode 2 is used for shear tests (drained simulations).

In both modes, the specified strain rate tensor is updated according to the following equation

$$\dot{\varepsilon}_{ij}^{t+\Delta t} = \dot{\varepsilon}_{ij}^{t} + \Delta\dot{\varepsilon}_{ij} \tag{A.1}$$

where $\dot{\varepsilon}_{ij}^{t}$ is the (old) specified strain rate tensor, whose initial values are set by the user; $\Delta\dot{\varepsilon}_{ij}$ is the change of the specified strain rate tensor, which is calculated according to

(A.2) or (A.3) depending on the modes used; $\dot{\varepsilon}_{ij}^{t+\Delta t}$ is the (new) updated specified strain rate tensor.

In mode 1, the change of the specified strain rate tensor $\Delta\dot{\varepsilon}_{ij}$ is updated according to the following equation

$$\Delta\dot{\varepsilon}_{ij} = \Delta\dot{\varepsilon}_{ij} + \frac{1}{3} g(\sigma_{ij}^{d} - \sigma_{ij}^{m}) \tag{A.2}$$

In mode 2, the change of the specified strain rate tensor $\Delta\dot{\varepsilon}_{ij}$ is updated according to the following equation

$$\Delta\dot{\varepsilon}_{ij} = \Delta\dot{\varepsilon}_{ij} + g(\sigma_{ij}^{d} - \sigma_{ij}^{m}) \left| \frac{\dot{\varepsilon}_{ij}}{|\dot{\varepsilon}_{11}| + |\dot{\varepsilon}_{22}| + |\dot{\varepsilon}_{33}|} \right| \tag{A.3}$$

In the equations (A.2) and (A.3), g is a gain parameter set by the user, σ_{ij}^{d} is the desired stress tensor and σ_{ij}^{m} is the measured stress tensor.

In the application of the servo-control, a limit is set for the maximum strain rate allowed for the simulation. This is necessary when high velocities are developed should the measured stress differ greatly from the desired stress. The limit of the maximum allowed strain rate is given in the servo-control command together with the gain parameter by the user.

APPENDIX B: GRAPHS FOR THE COMPARISON OF DAC AND DPS IN CHAPTER 7

Figure B.1a-h: Evolution of q

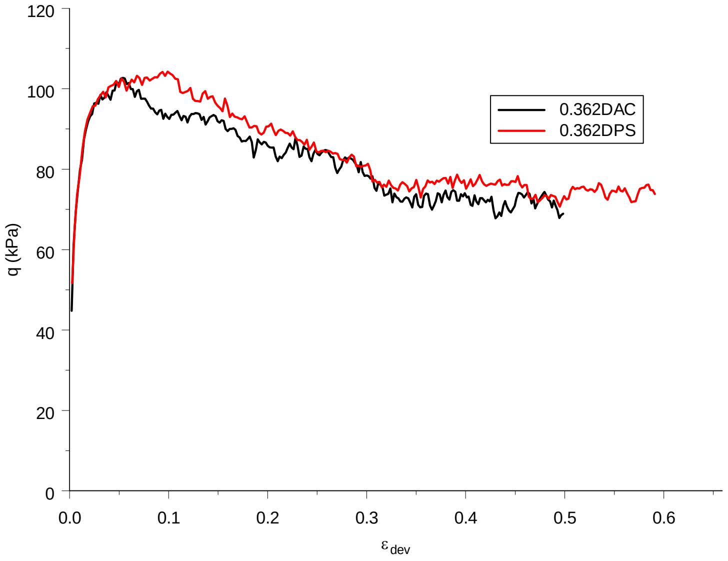

Fig. B.1a Evolution of q for porosity0.362

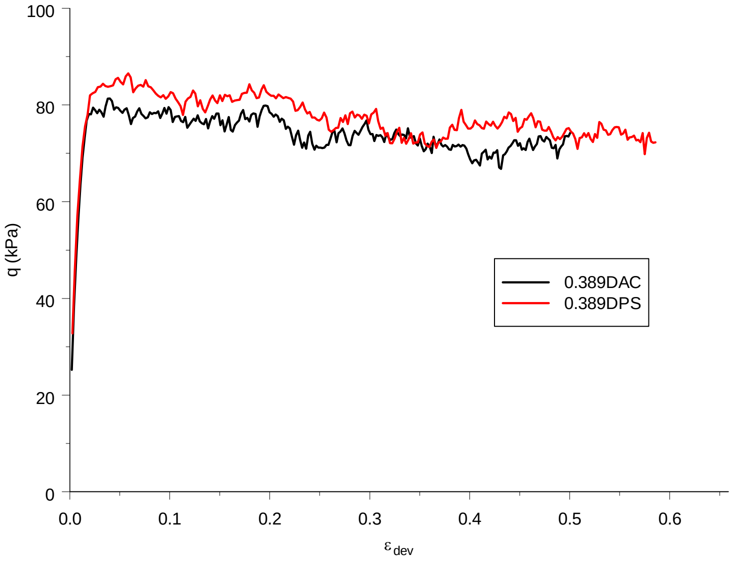

Fig. B.1b Evolution of q for porosity0.389

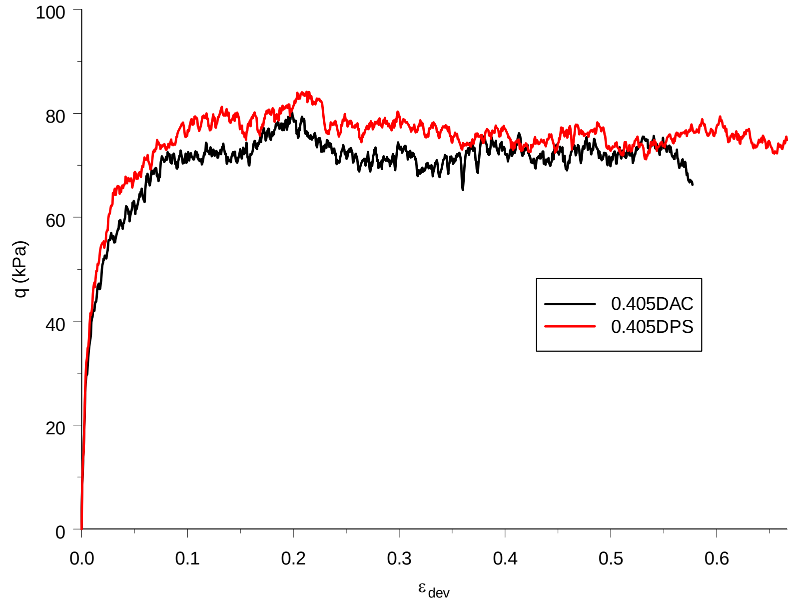

Fig. B.1c Evolution of q for porosity0.405

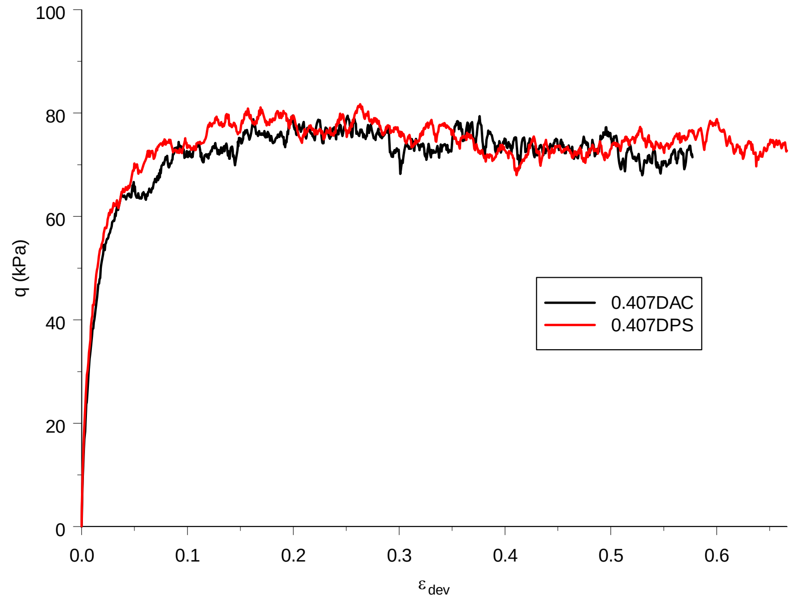

Fig. B.1d Evolution of q for porosity0.407

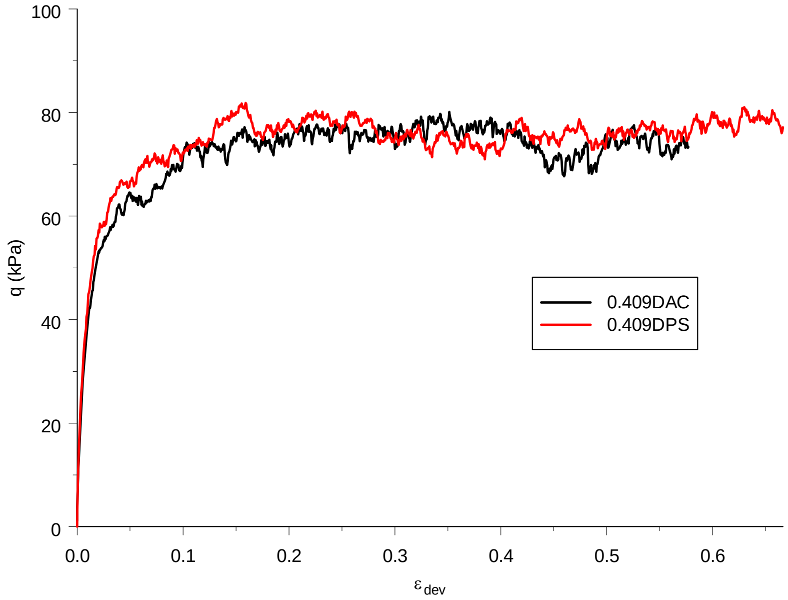

Fig. B.1e Evolution of q for porosity0.409

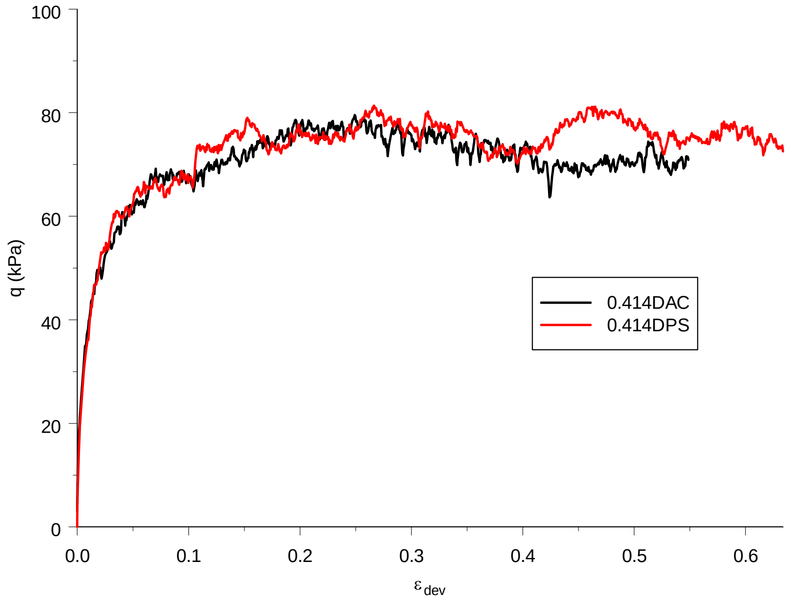

Fig. B.1f Evolution of q for porosity0.414

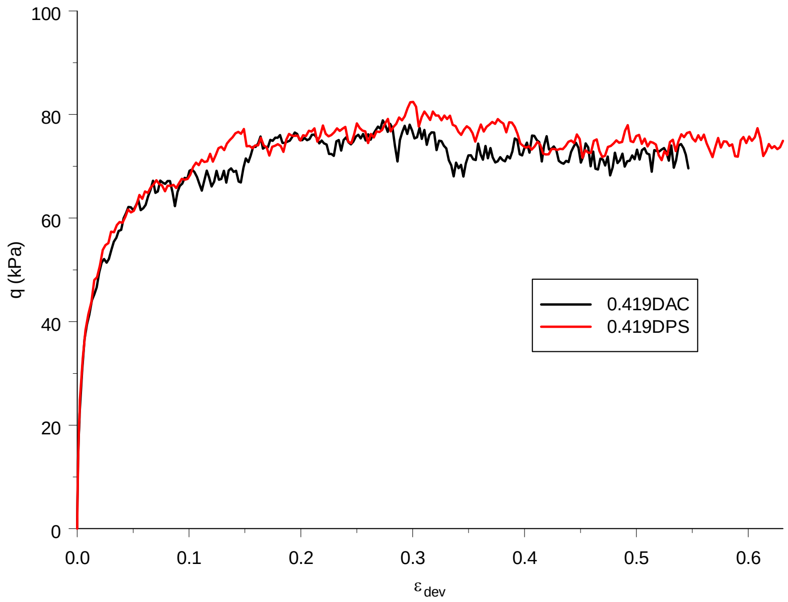

Fig. B.1g Evolution of q for porosity0.419

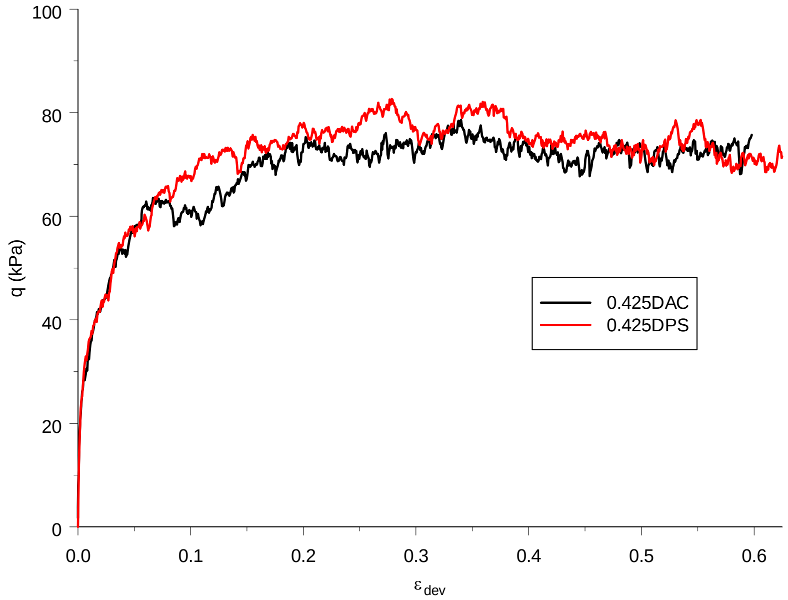

Fig. B.1h Evolution of q for porosity0.425

Figure B.2a-h: Evolution of q_{dev}

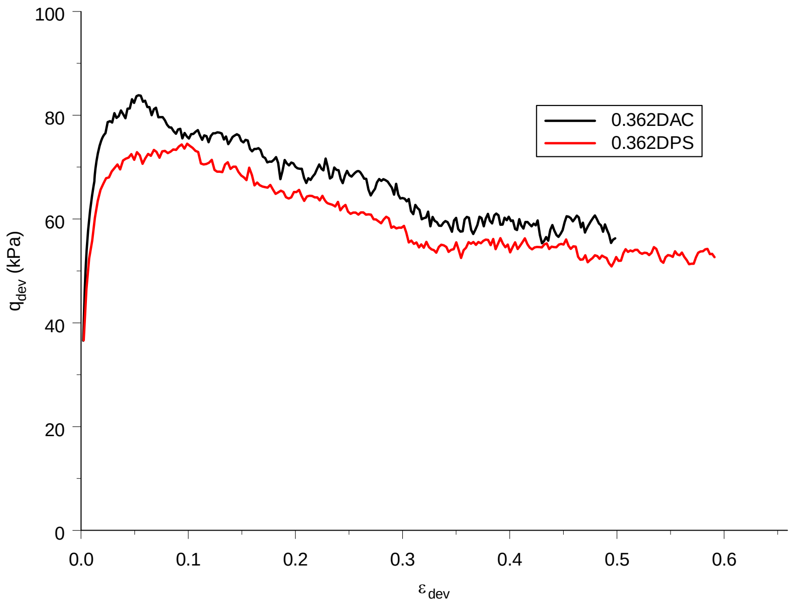

Fig. B.2a Evolution of q_{dev} for porosity0.362

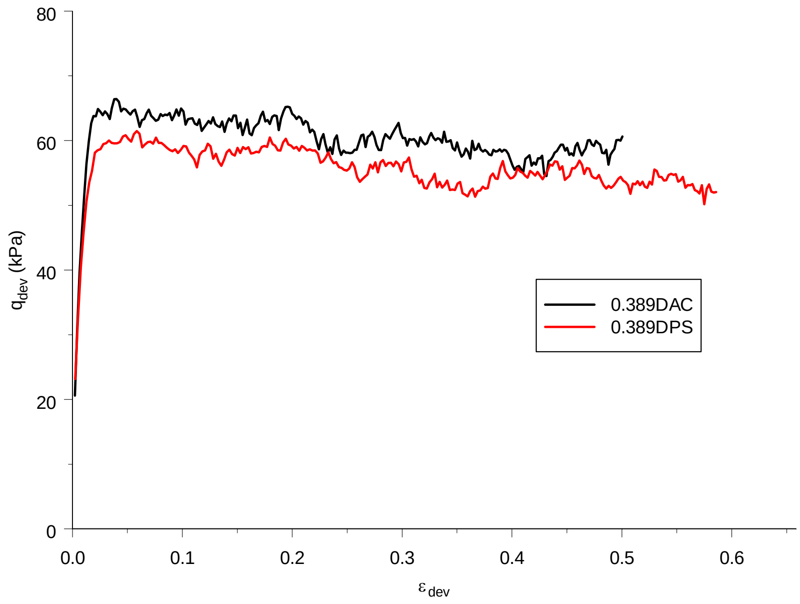

Fig. B.2b Evolution of q_{dev} for porosity0.389

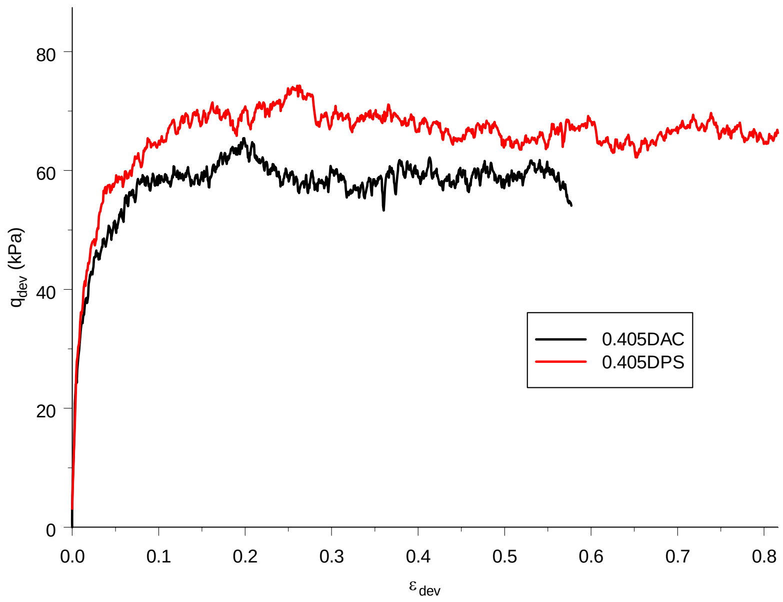

Fig. B.2c Evolution of q_{dev} for porosity0.405

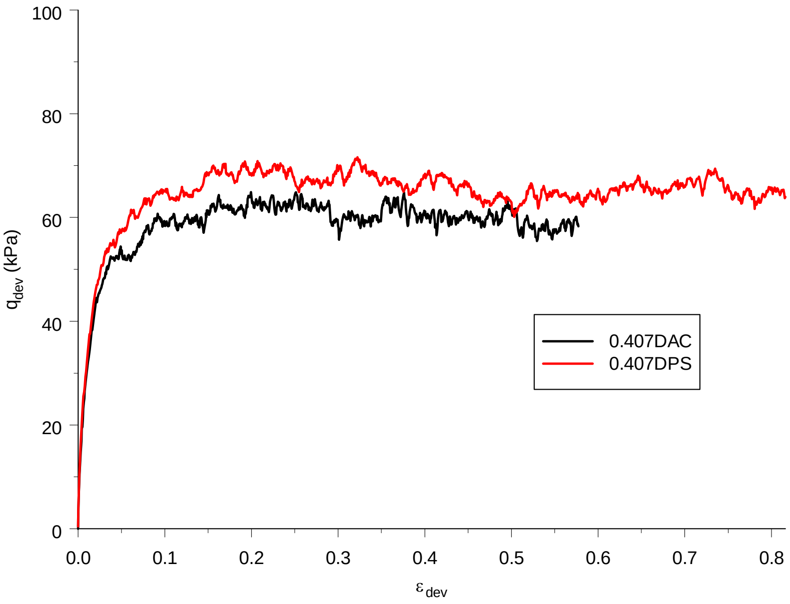

Fig. B.2d Evolution of q_{dev} for porosity0.407

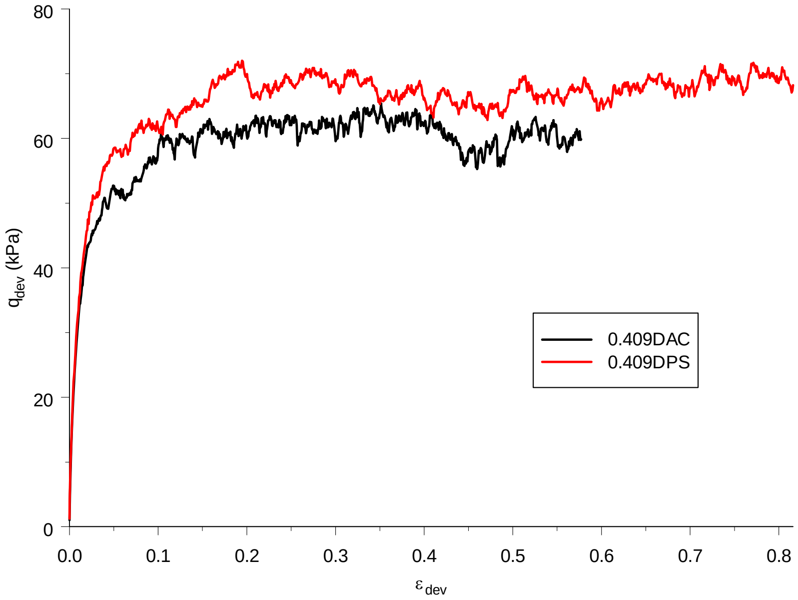

Fig. B.2e Evolution of q_{dev} for porosity0.409

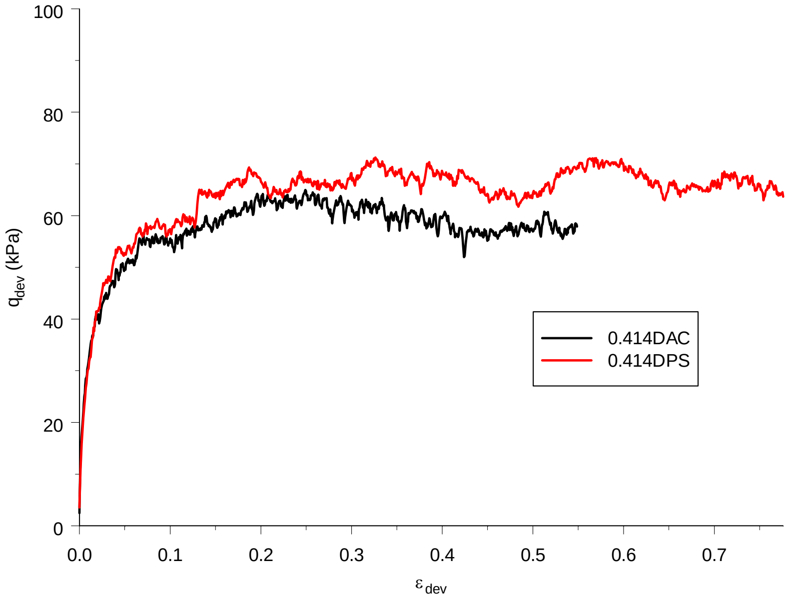

Fig. B.2f Evolution of q_{dev} for porosity0.414

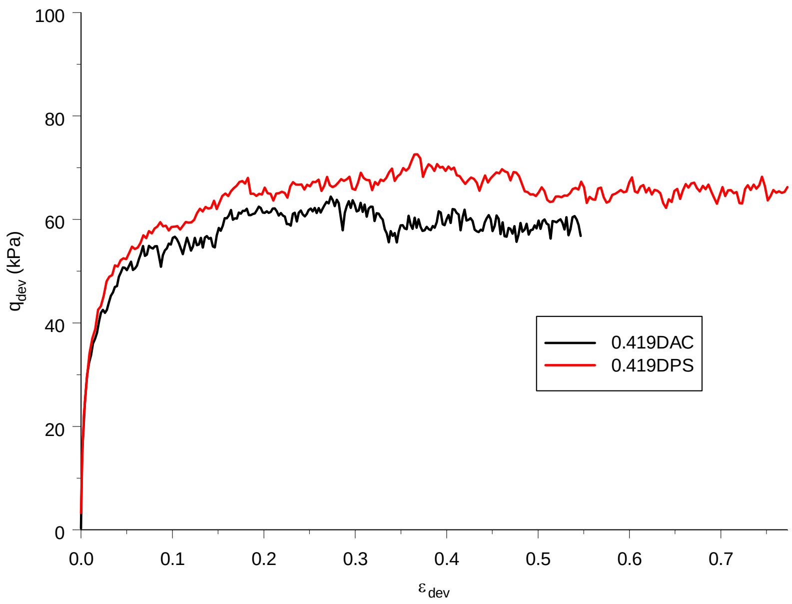

Fig. B.2g Evolution of q_{dev} for porosity0.419

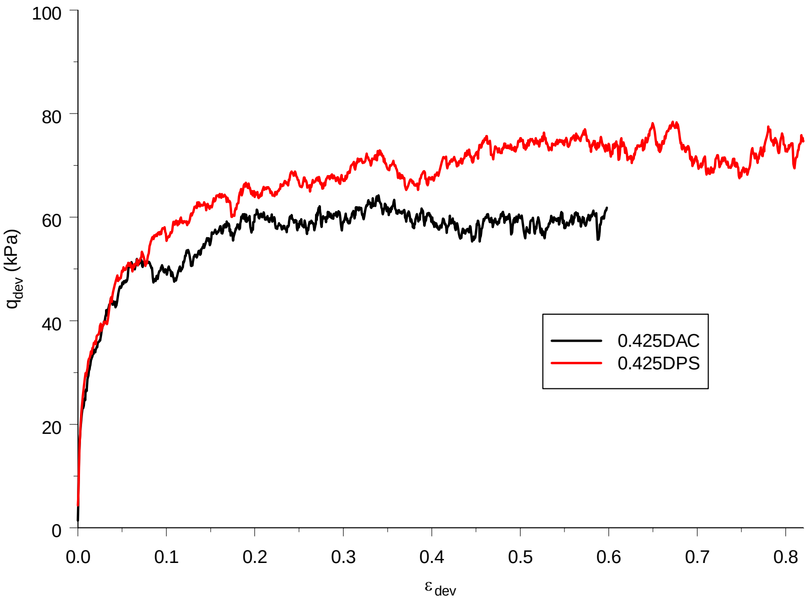

Fig. B.2h Evolution of q_{dev} for porosity0.425

Figure B.3a-h: Evolution of sin φ

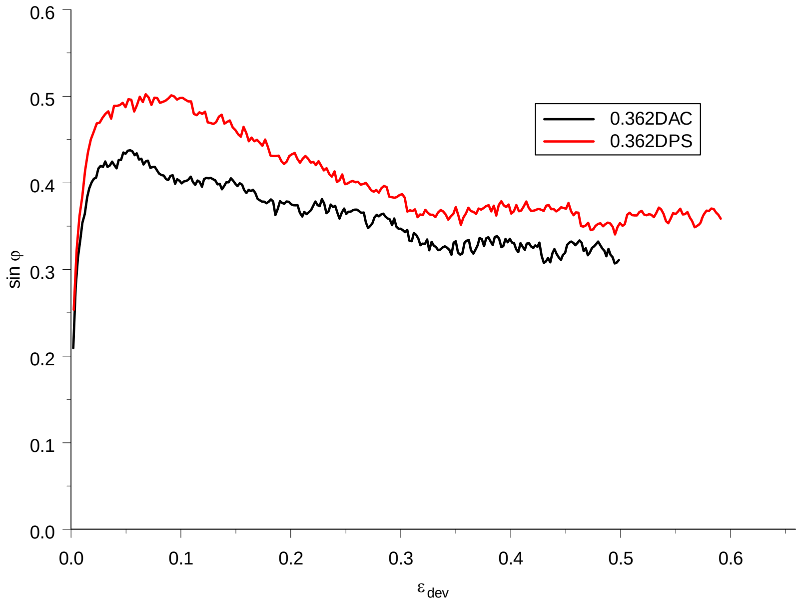

Fig. B.3.a Evolution of sin φ for porosity0.362

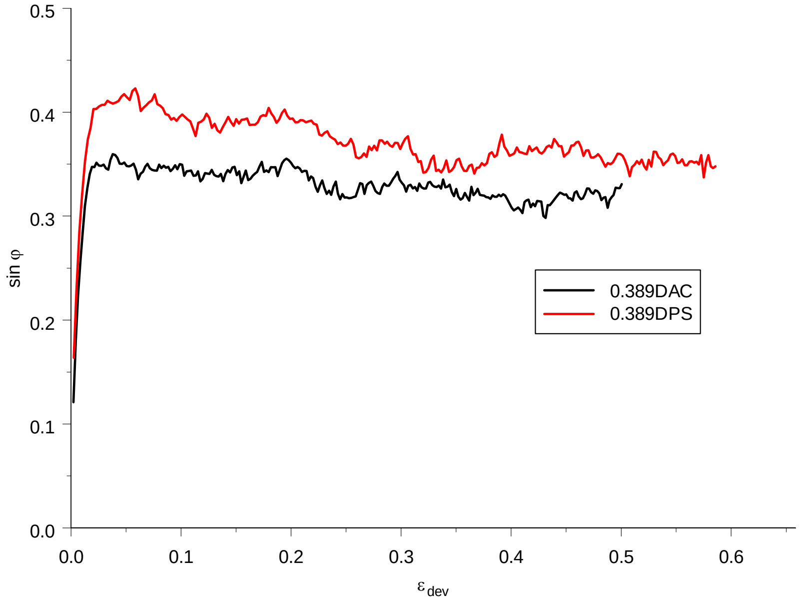

Fig. B.3.b Evolution of sin φ for porosity0.389

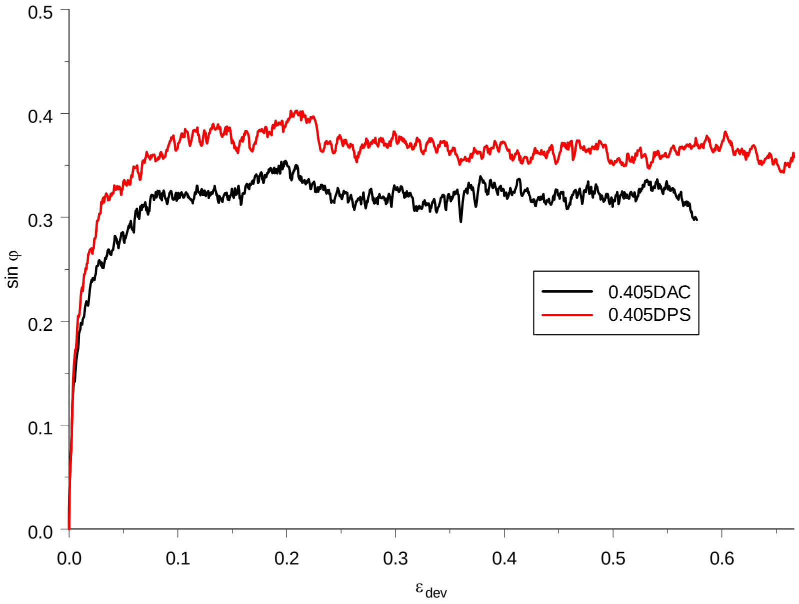

Fig. B.3.c Evolution of sin φ for porosity0.405

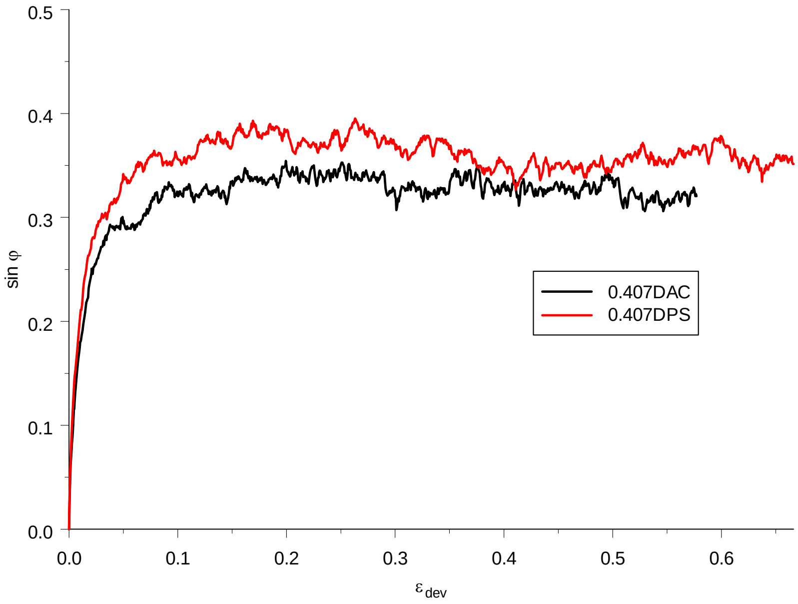

Fig. B.3.d Evolution of sin φ for porosity0.407

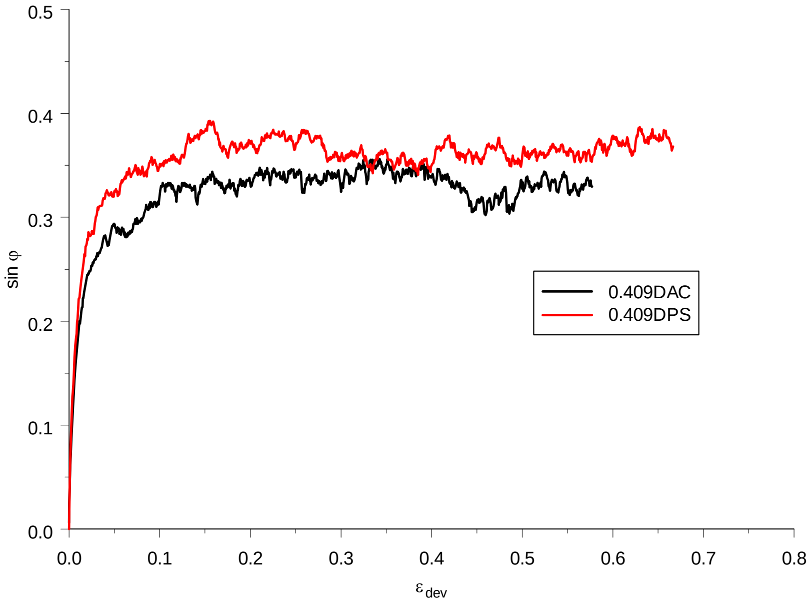

Fig. B.3.e Evolution of sin φ for porosity0.409

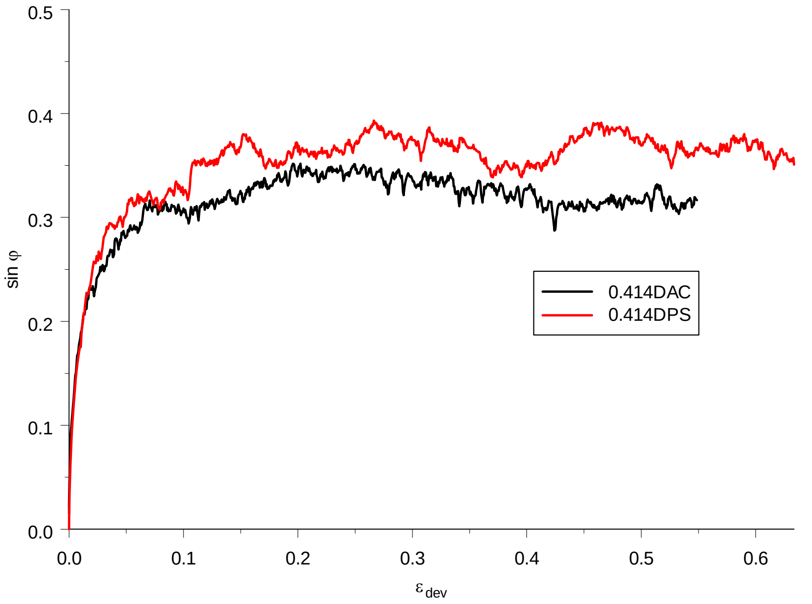

Fig. B.3.f Evolution of sin φ for porosity0.414

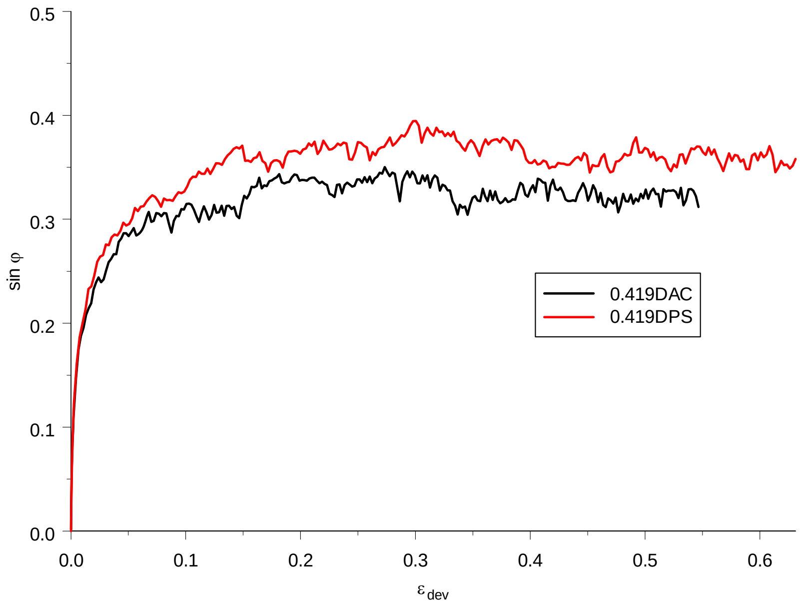

Fig. B.3.g Evolution of sin φ for porosity0.419

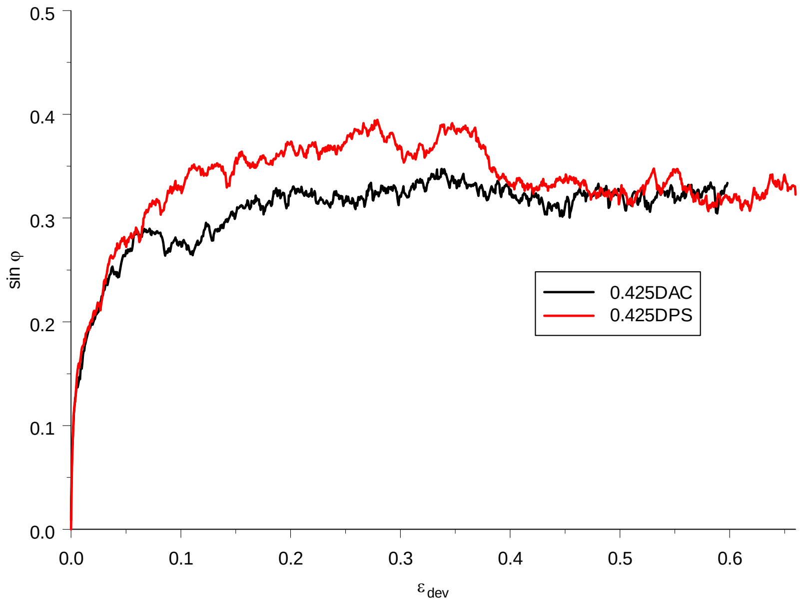

Fig. B.3.h Evolution of sin φ for porosity0.425

Figure B.4a-h: Evolution of η

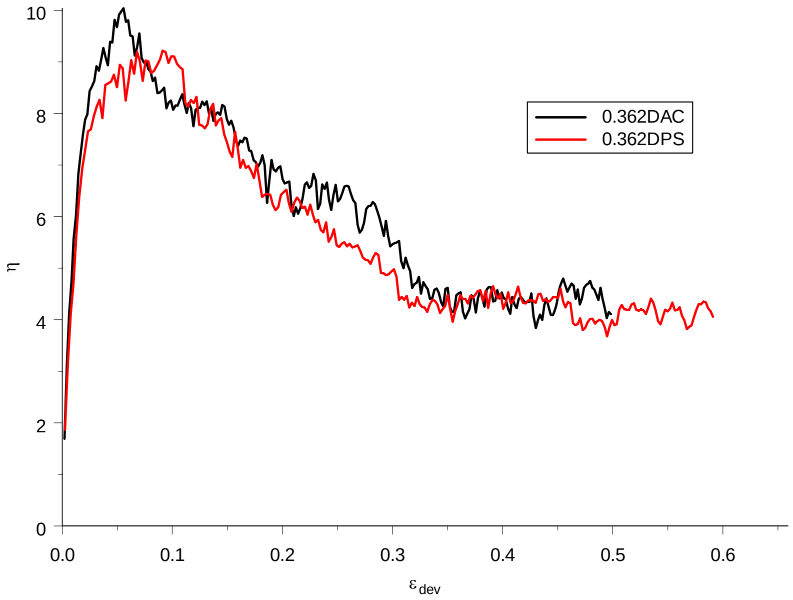

Fig. B.4a Evolution of η for porosity0.362

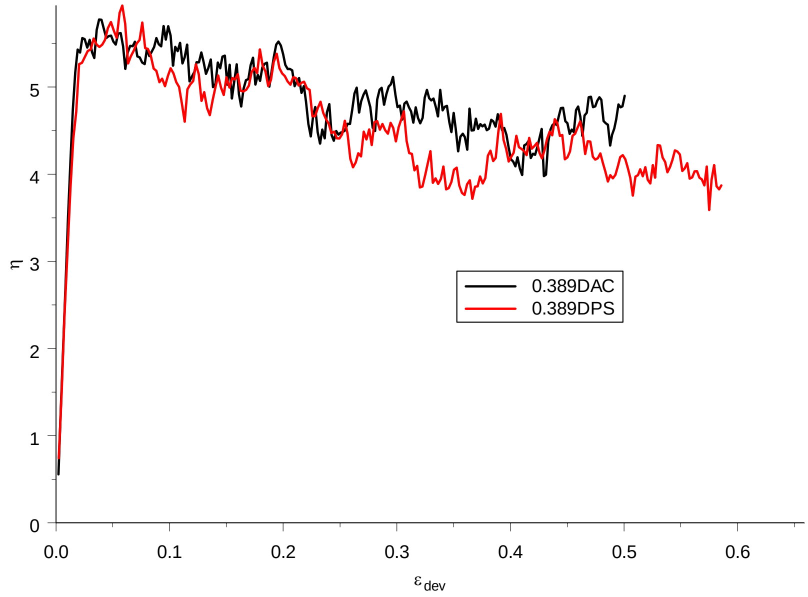

Fig. B.4b Evolution of η for porosity0.389

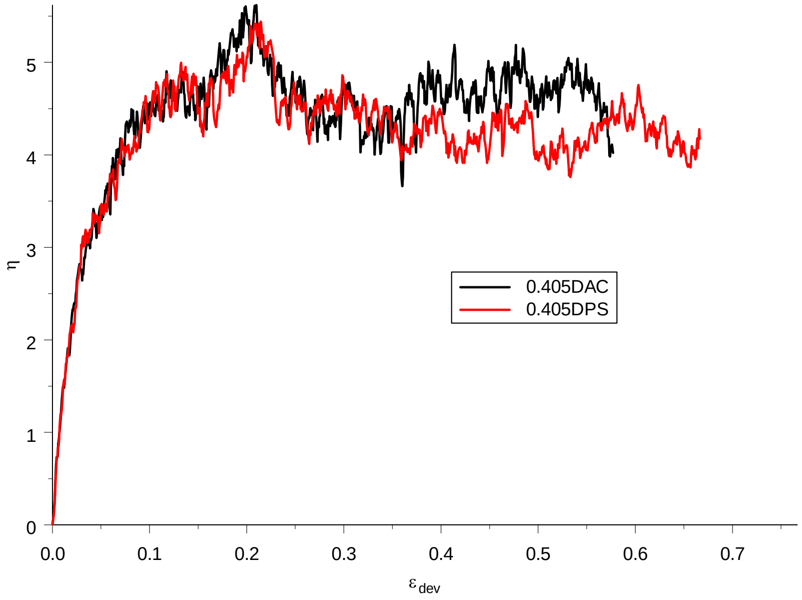

Fig. B.4c Evolution of η for porosity0.405

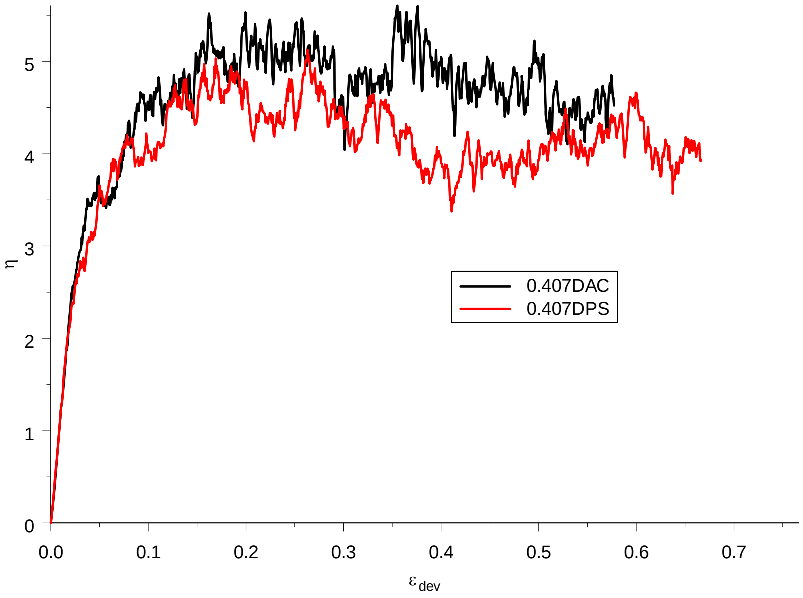

Fig. B.4d Evolution of η for porosity0.407

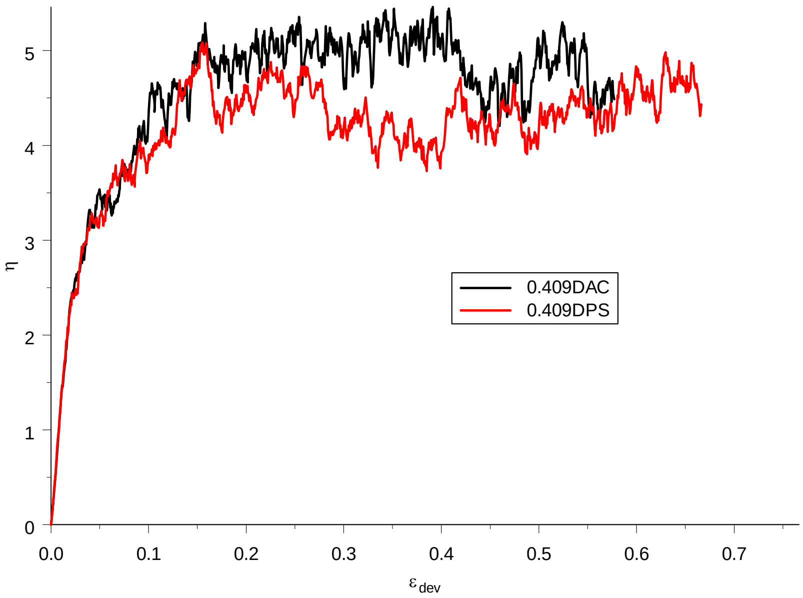

Fig. B.4e Evolution of η for porosity0.409

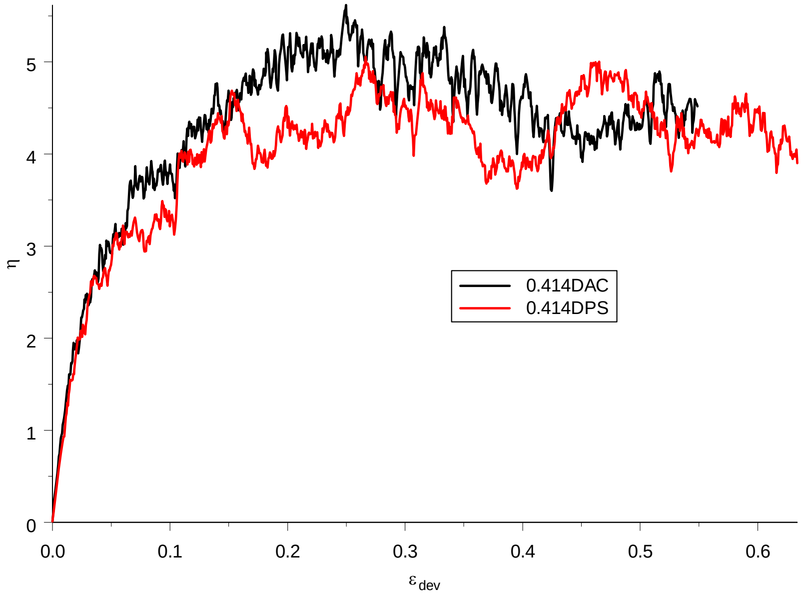

Fig. B.4f Evolution of η for porosity0.414

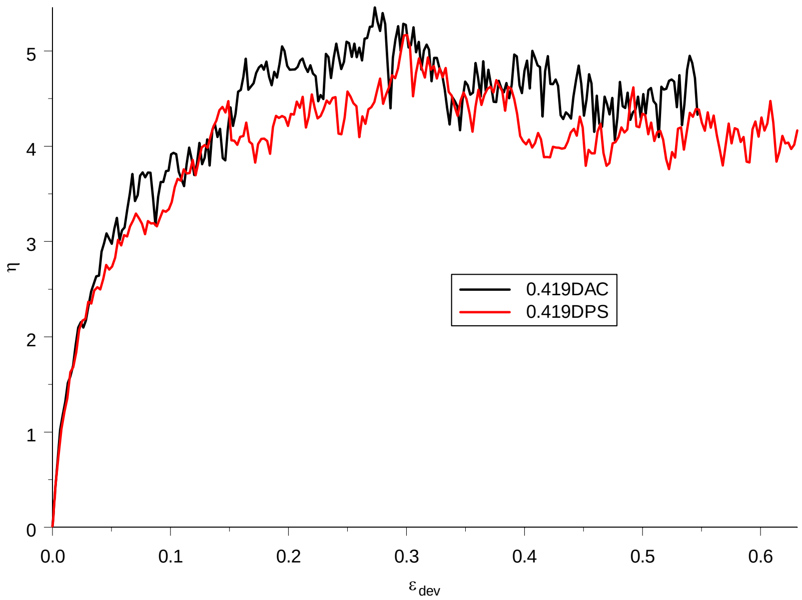

Fig. B.4g Evolution of η for porosity0.419

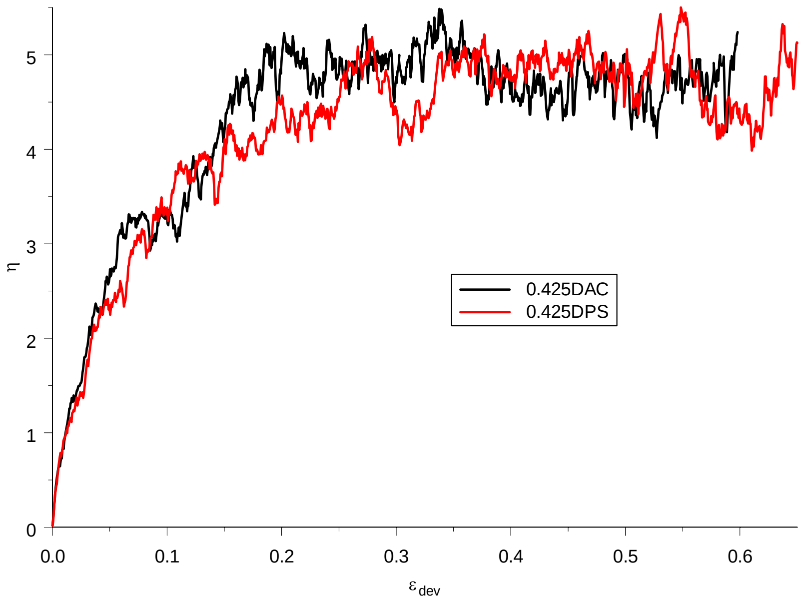

Fig. B.4h Evolution of η for porosity0.425

Figure B.5a-h: Evolution of porosity

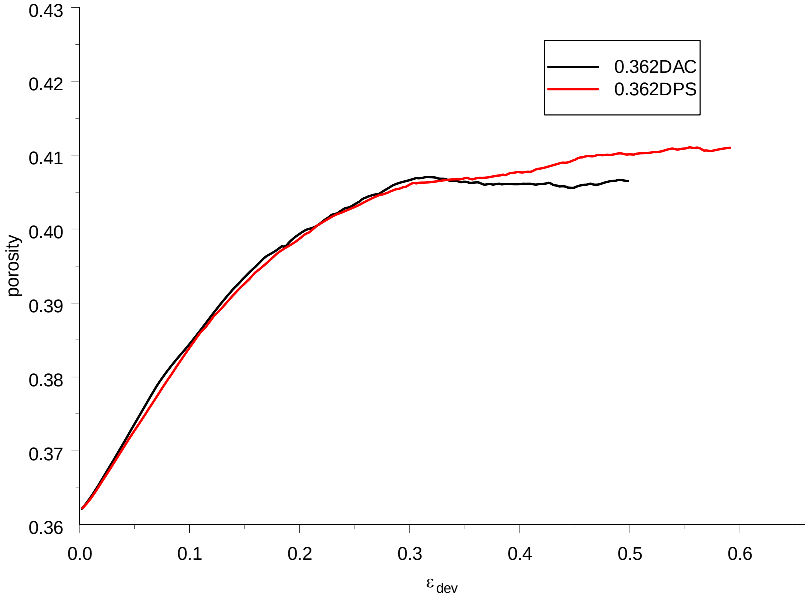

Fig. B.5a Evolution of porosity0.362

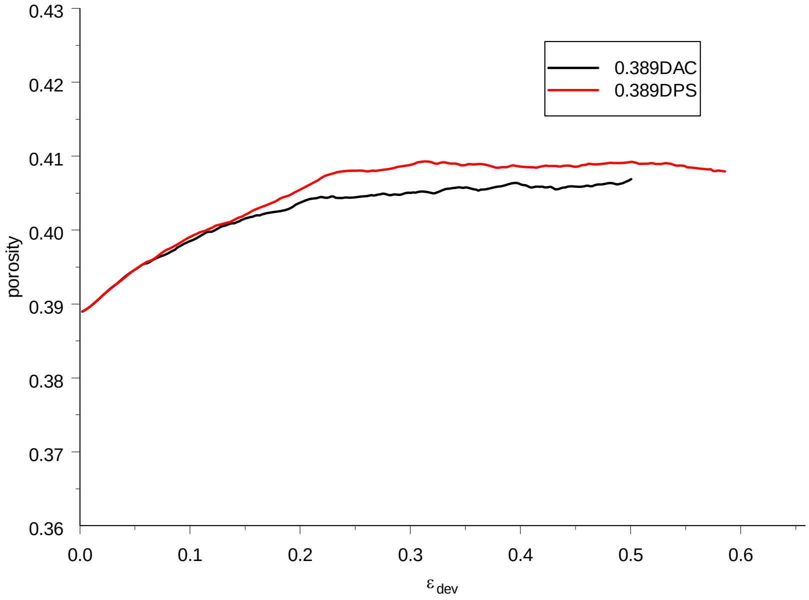

Fig. B.5b Evolution of porosity0.389

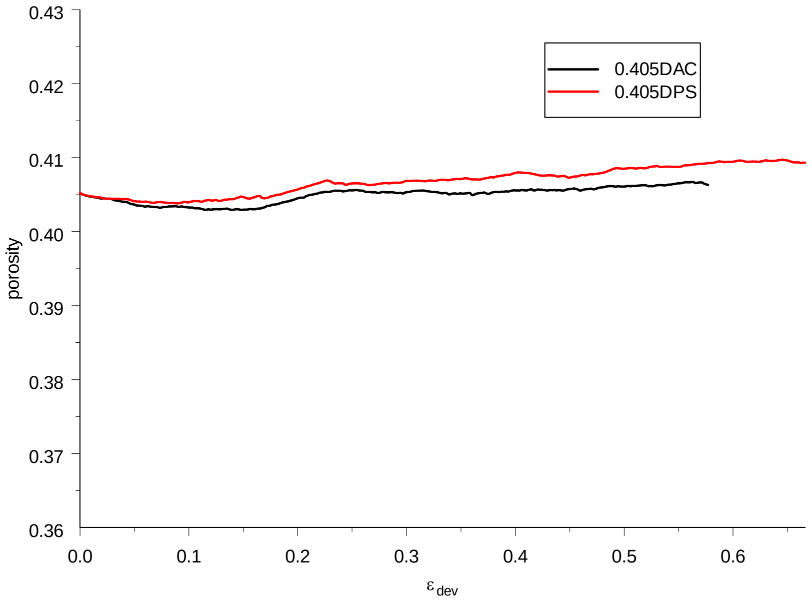

Fig. B.5c Evolution of porosity0.405

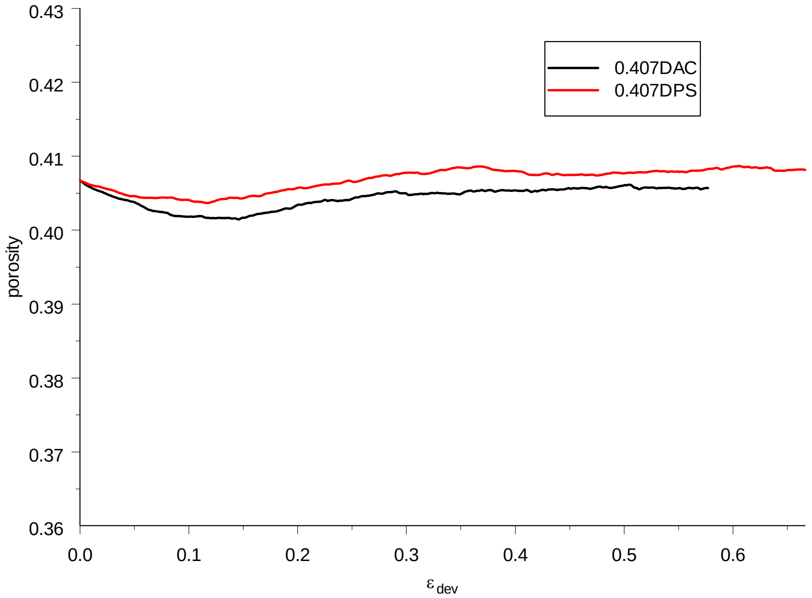

Fig. B.5d Evolution of porosity0.407

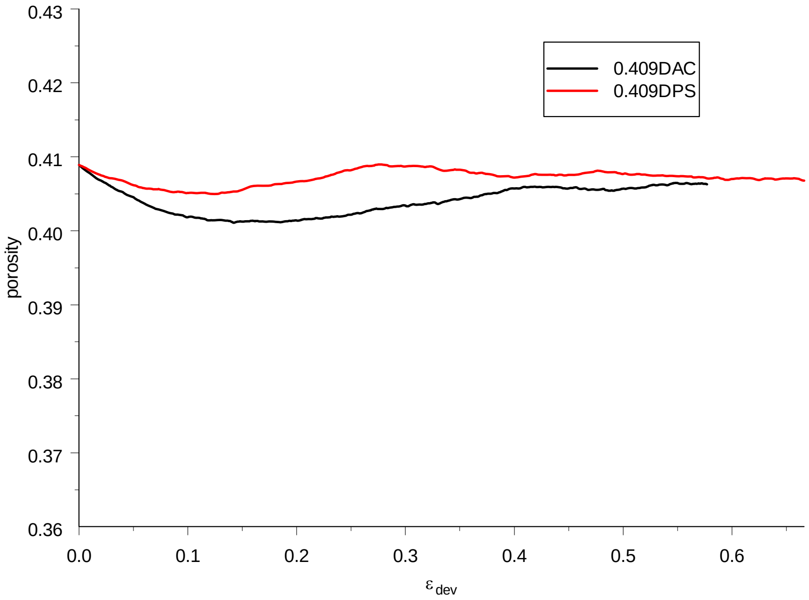

Fig. B.5e Evolution of porosity0.409

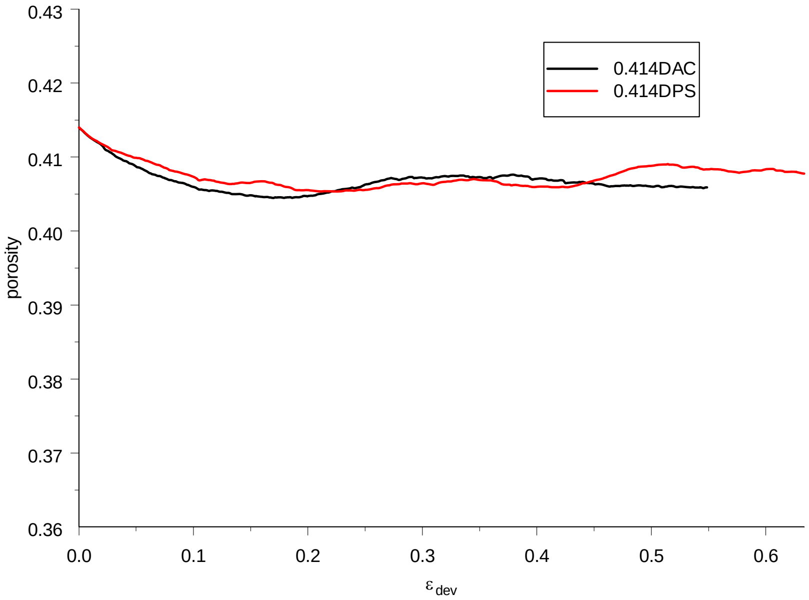

Fig. B.5f Evolution of porosity0.414

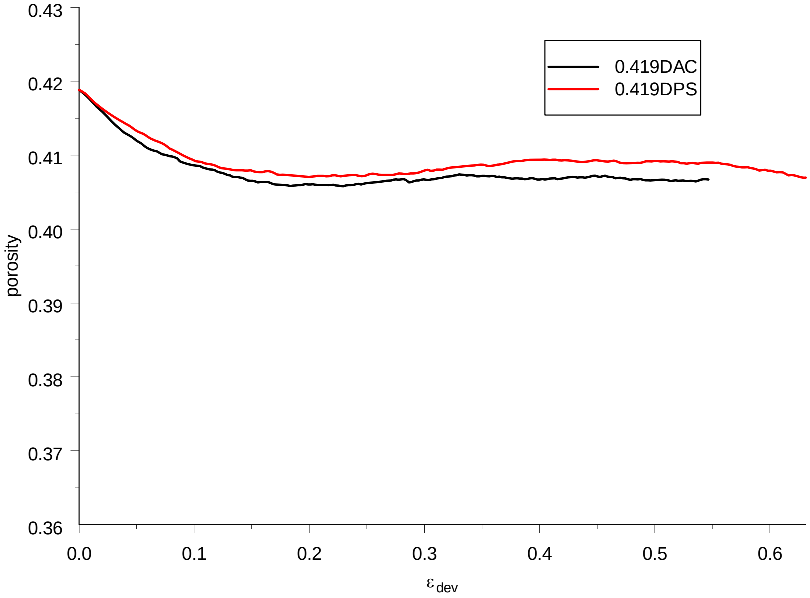

Fig. B.5g Evolution of porosity0.419

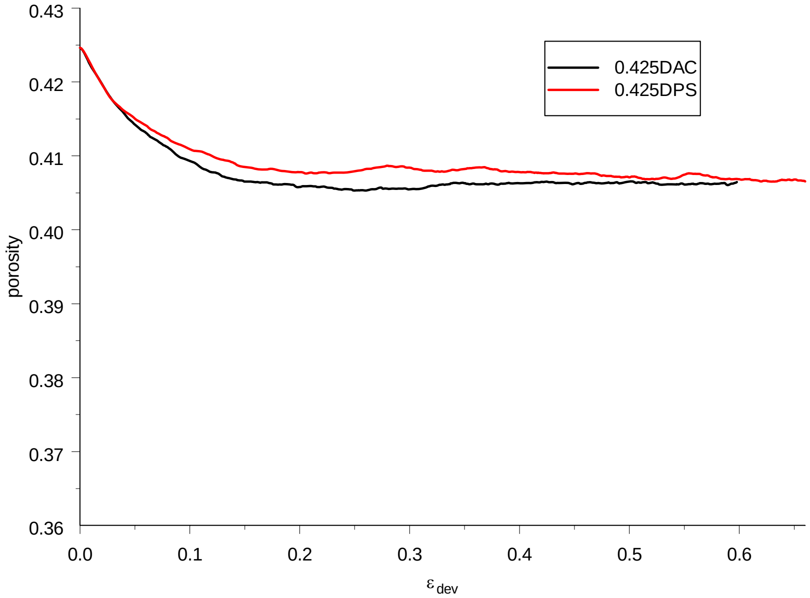

Fig. B.5h Evolution of porosity0.425

Figure B.6a-h: Evolution of deviator fabric

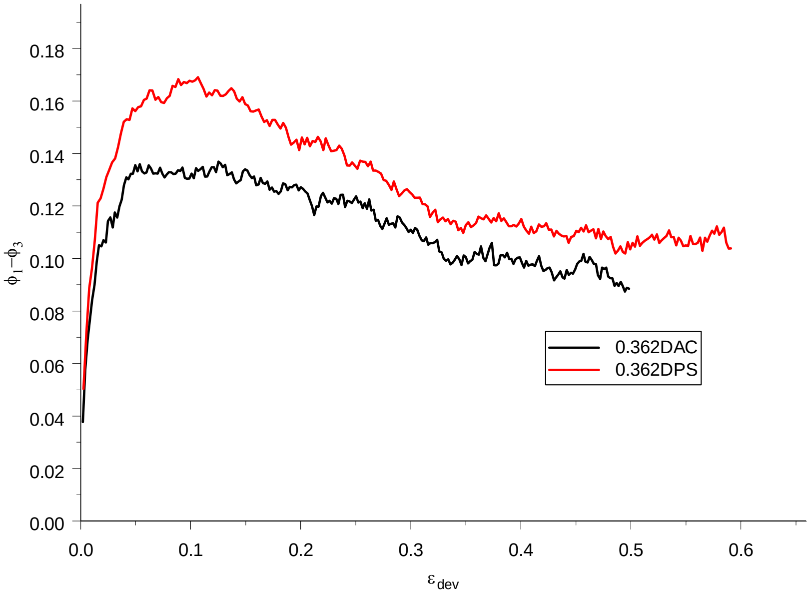

Fig. B.6a Evolution of deviator fabric for porosity0.362

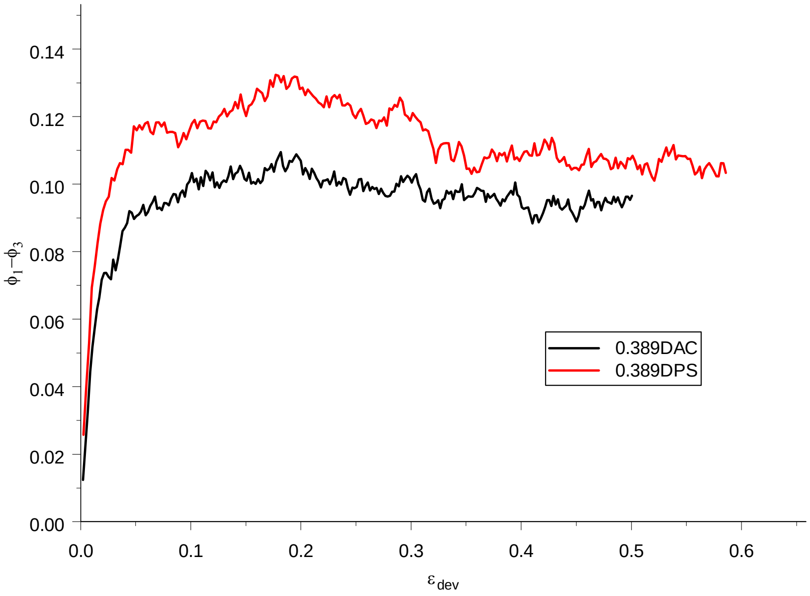

Fig. B.6b Evolution of deviator fabric for porosity0.389

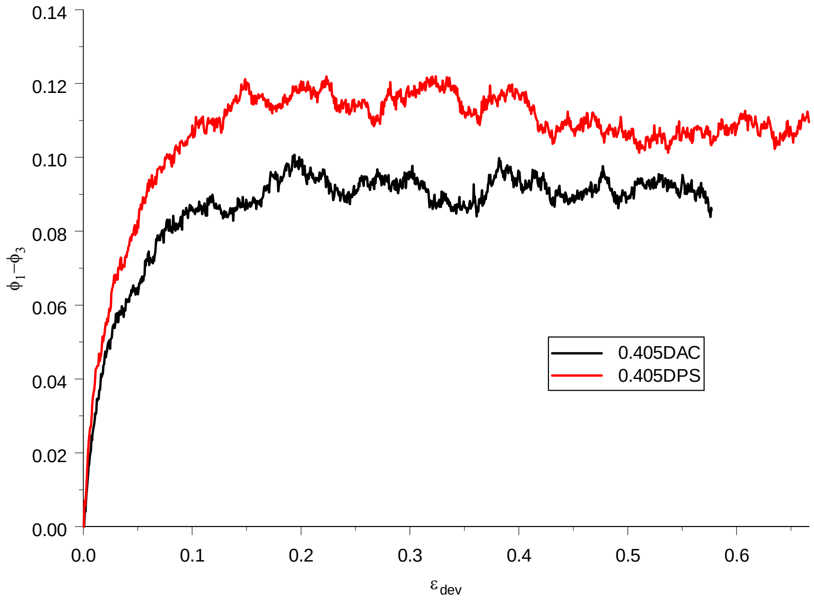

Fig. B.6c Evolution of deviator fabric for porosity0.405

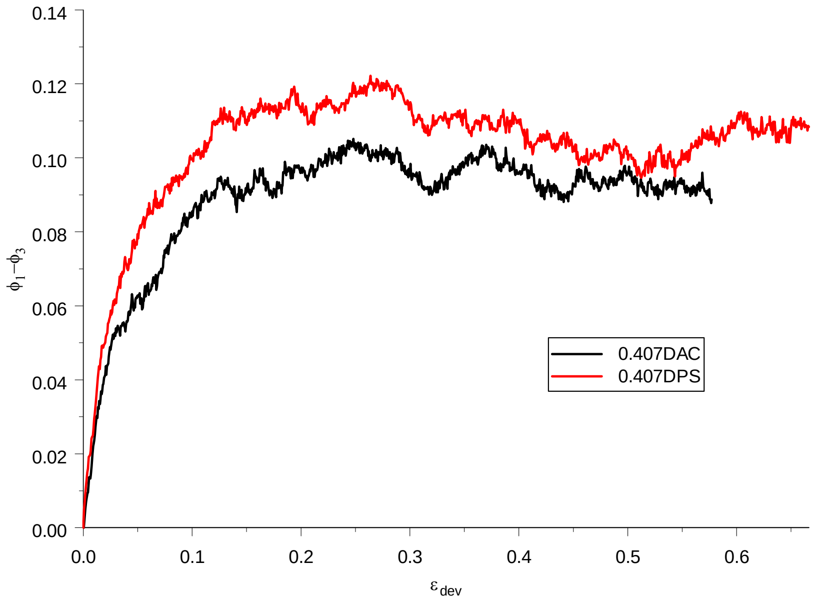

Fig. B.6d Evolution of deviator fabric for porosity0.407

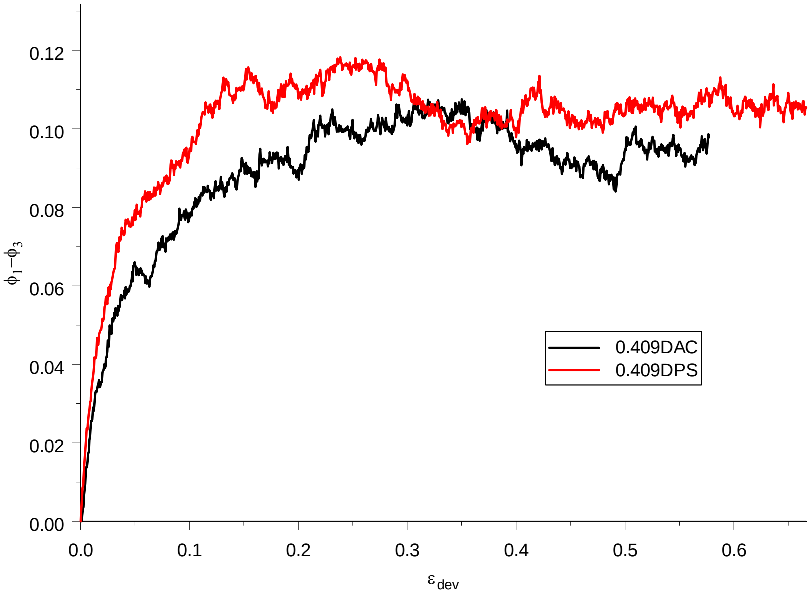

Fig. B.6e Evolution of deviator fabric for porosity0.409

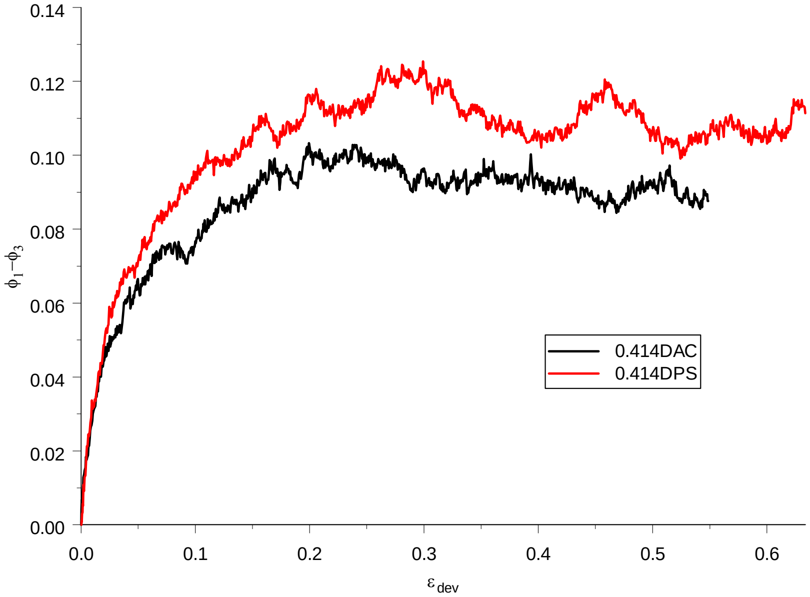

Fig. B.6f Evolution of deviator fabric for porosity0.414

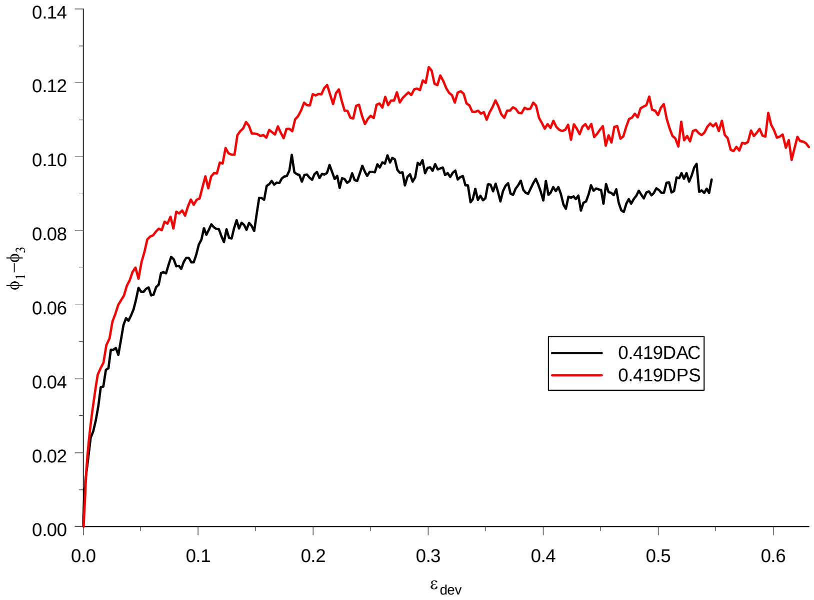

Fig. B.6g Evolution of deviator fabric for porosity0.419

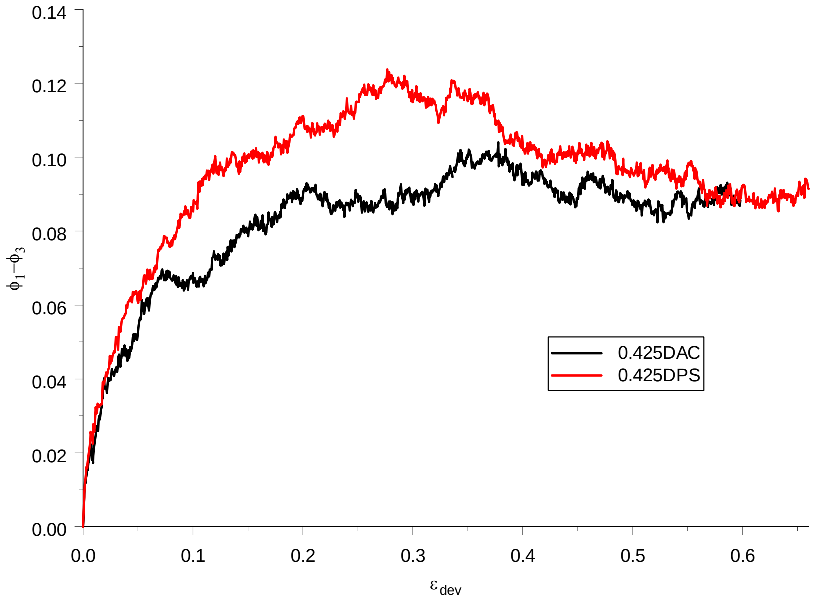

Fig. B.6h Evolution of deviator fabric for porosity0.425

Figure B.7a-h: Evolution of η^{ϕ}

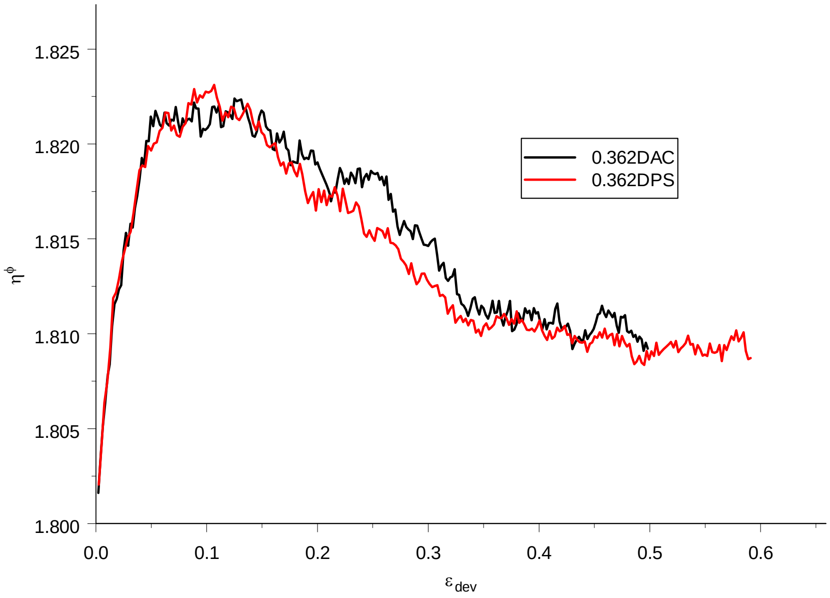

Fig. B.7a Evolution of η^{ϕ} for porosity0.362

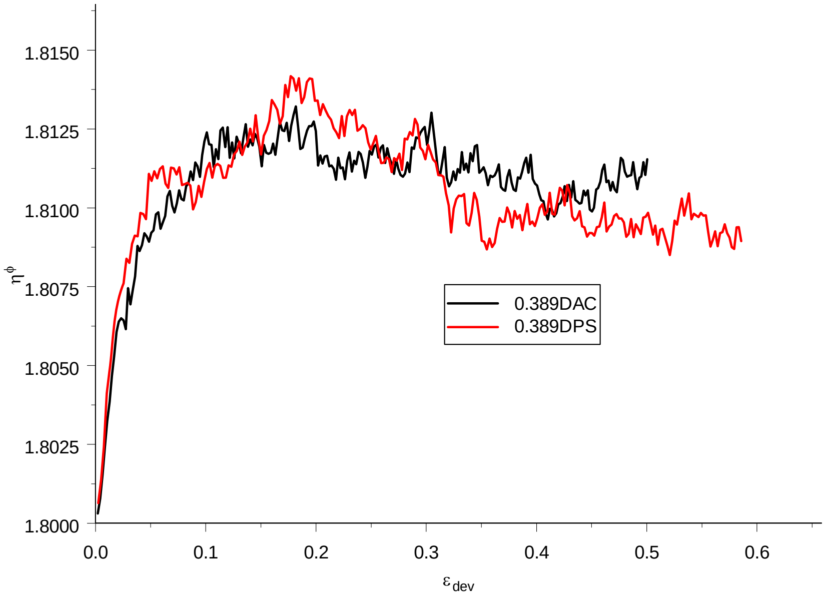

Fig. B.7b Evolution of η^{ϕ} for porosity0.389

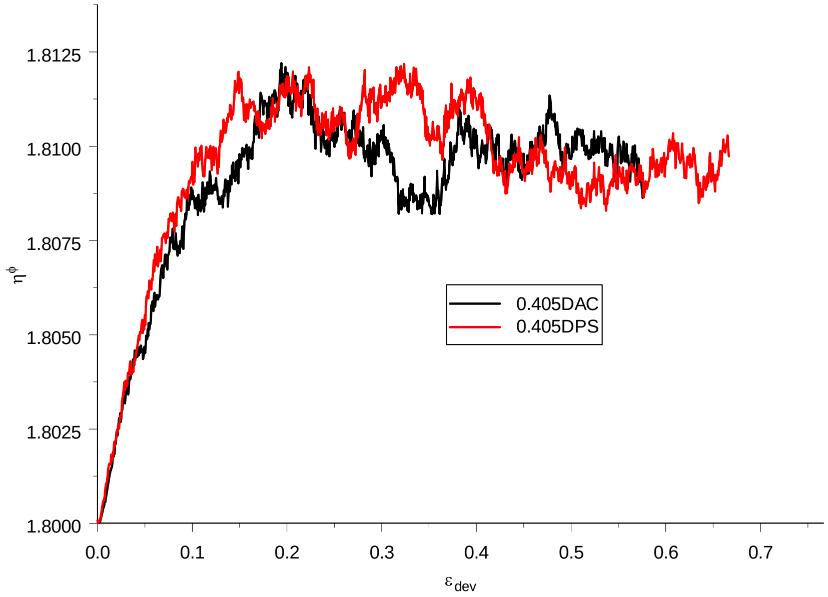

Fig. B.7c Evolution of η^{ϕ} for porosity0.405

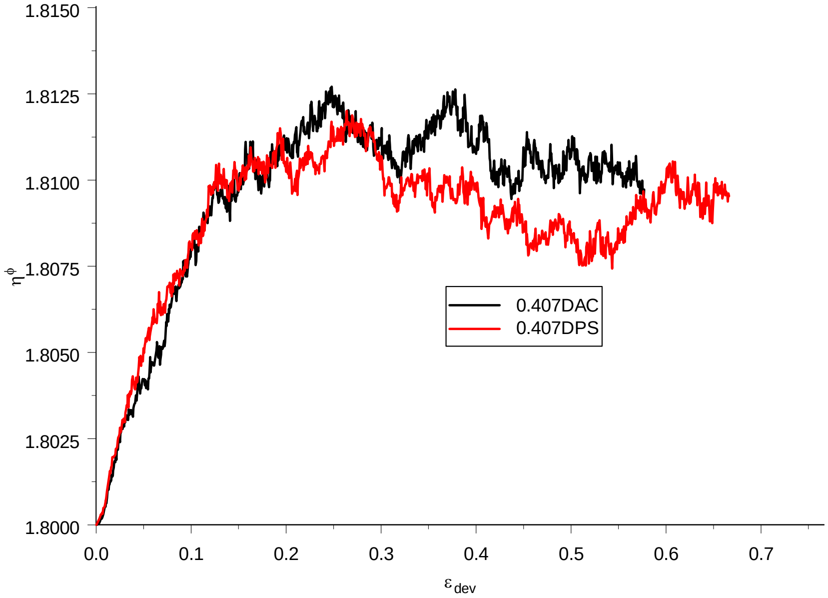

Fig. B.7d Evolution of η^{ϕ} for porosity0.407

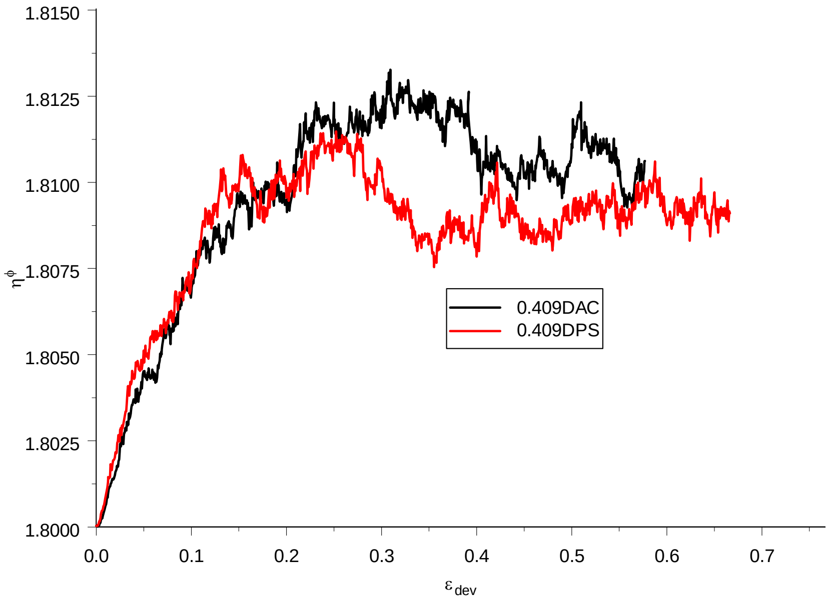

Fig. B.7e Evolution of η^{ϕ} for porosity0.409

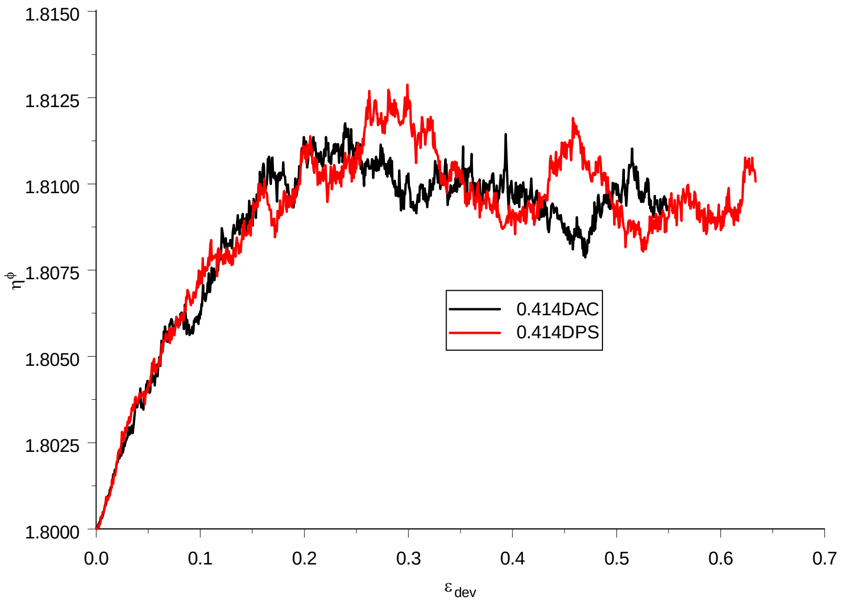

Fig. B.7f Evolution of η^{ϕ} for porosity0.414

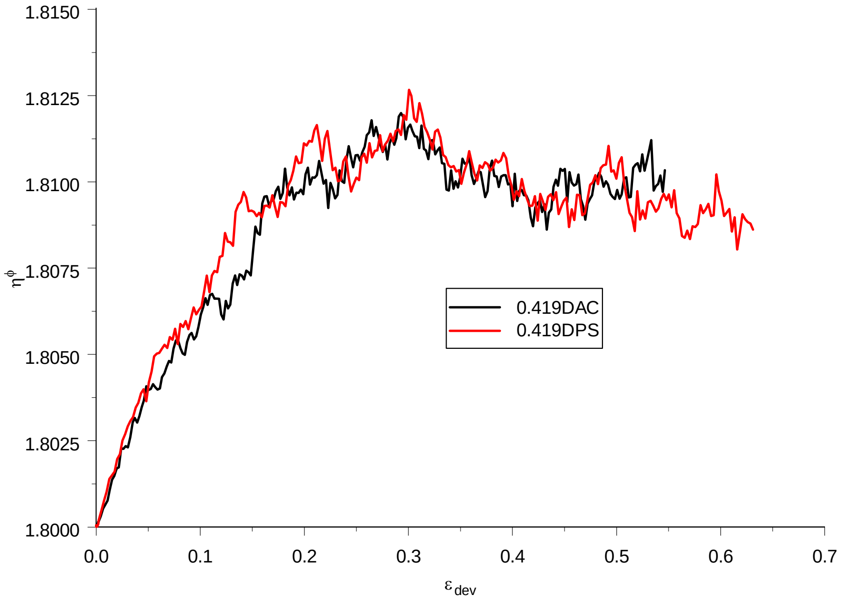

Fig. B.7g Evolution of η^{ϕ} for porosity0.419

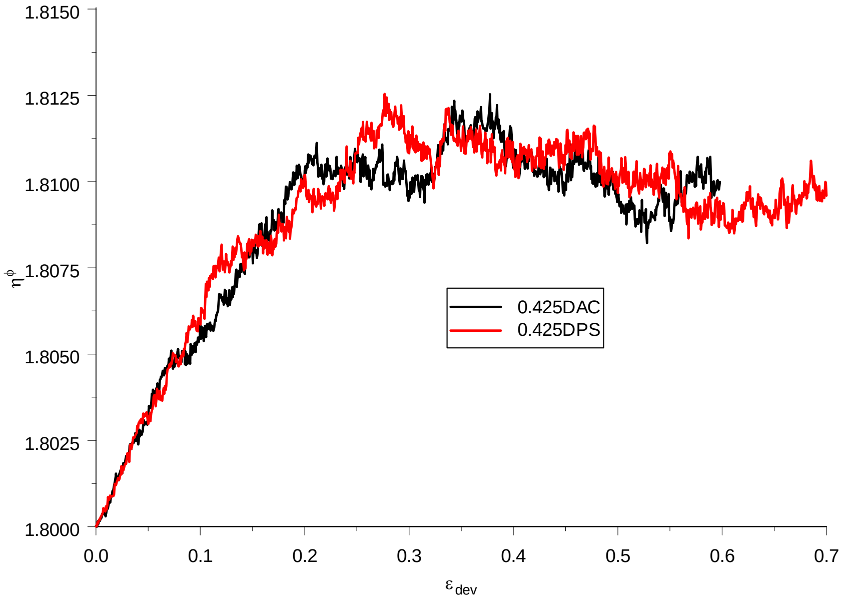

Fig. B.7h Evolution of η^{ϕ} for porosity0.425

Figure B.8a-h: Evolution of Z_m

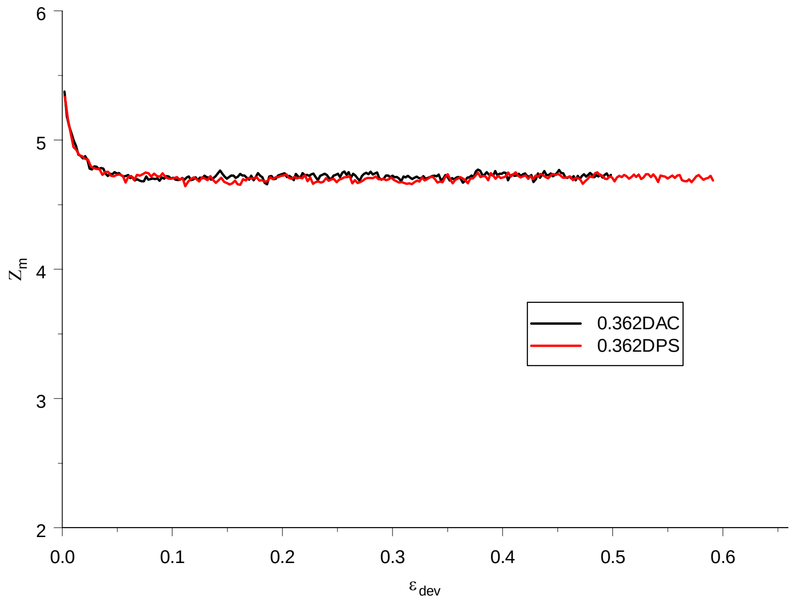

Fig. B.8a Evolution of Z_m for porosity0.362

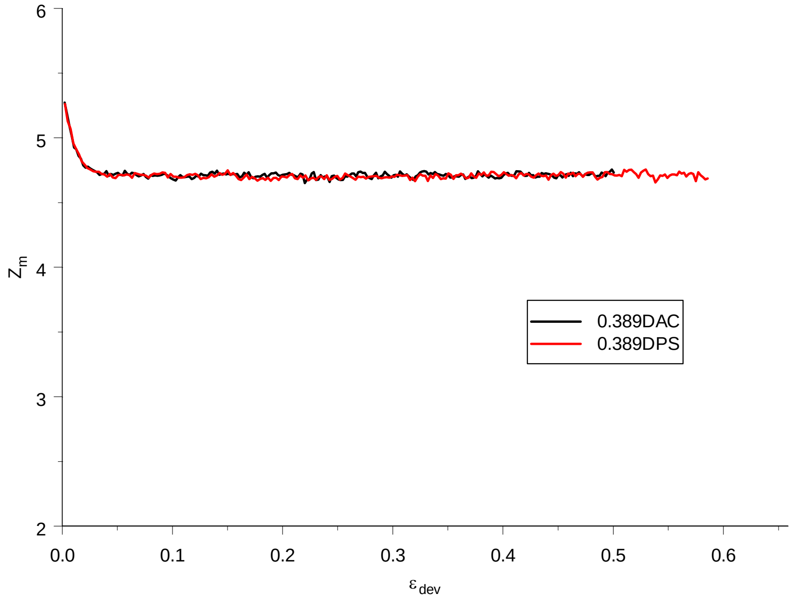

Fig. B.8b Evolution of Z_m for porosity0.389

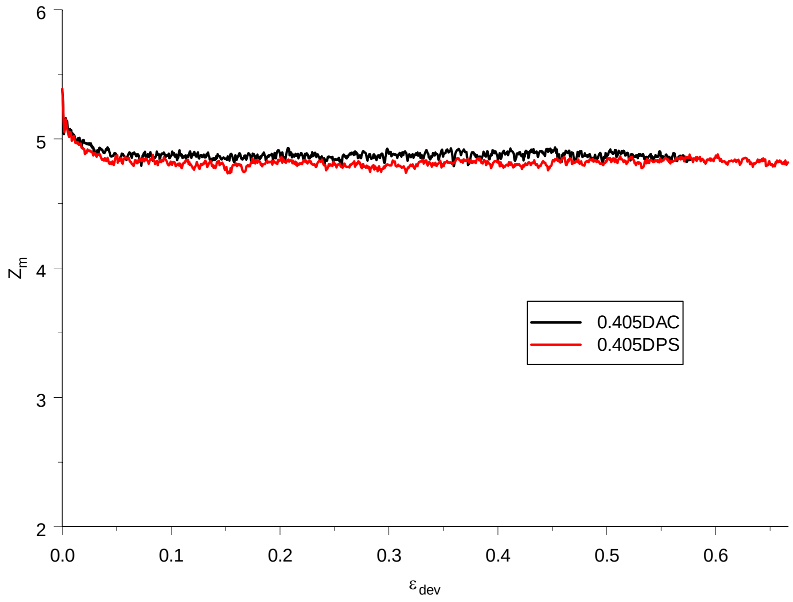

Fig. B.8c Evolution of Z_m for porosity0.405

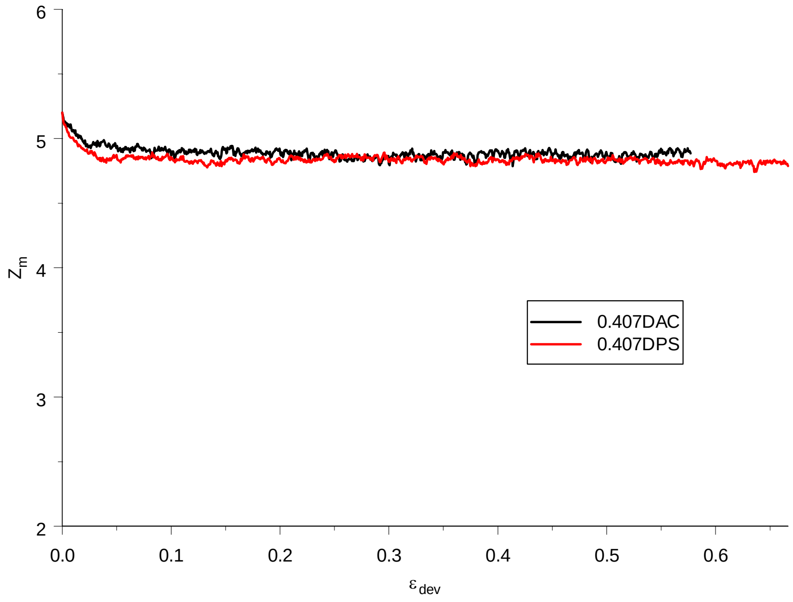

Fig. B.8d Evolution of Z_m for porosity0.407

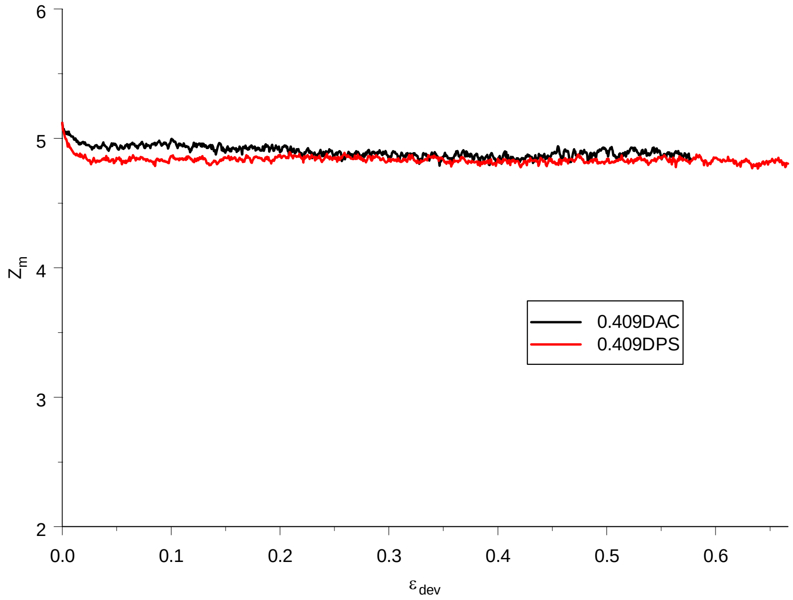

Fig. B.8e Evolution of Z_m for porosity0.409

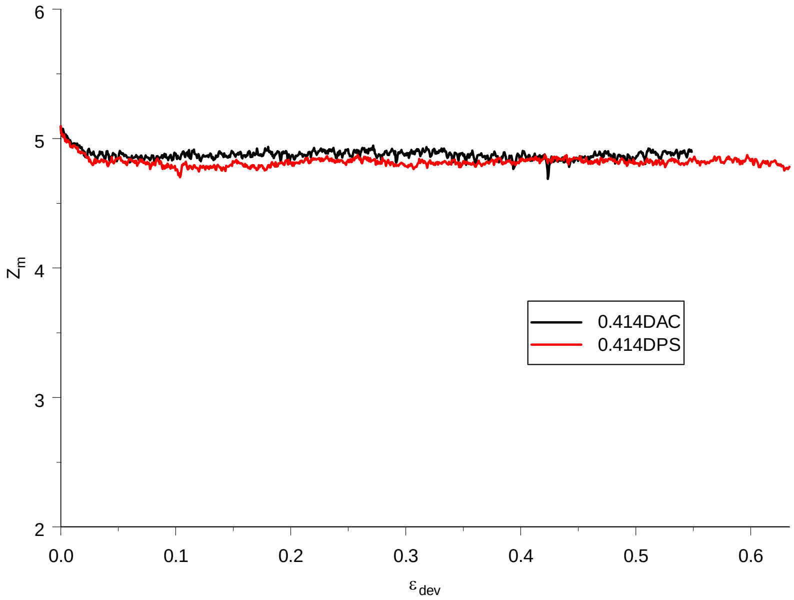

Fig. B.8f Evolution of Z_m for porosity0.414

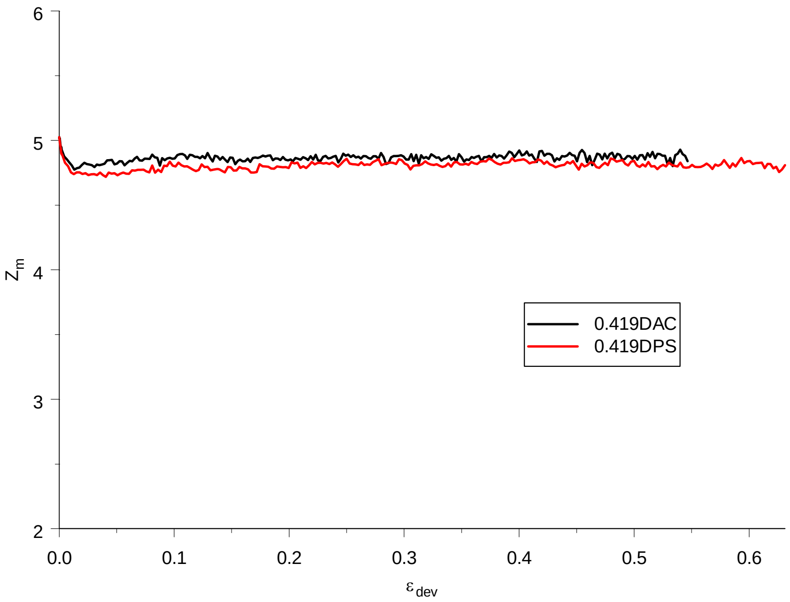

Fig. B.8g Evolution of Z_m for porosity0.419

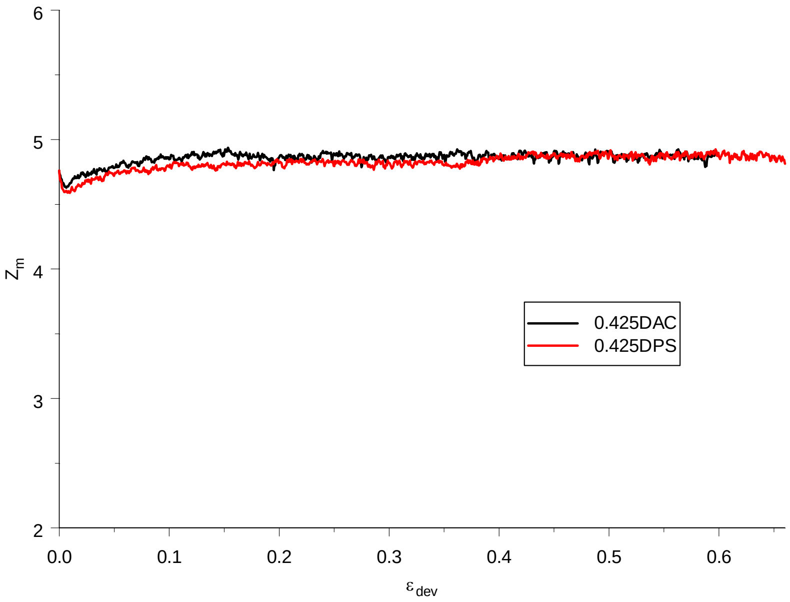

Fig. B.8h Evolution of Z_m for porosity0.425